Remote Sensing Laboratories – RSL

Department of Geography, University of Zurich, Switzerland

Wide-area wet snow mapping of the Alps based on Sentinel-1 multi-track radar backscatter composites

GEO 511 – Master's Thesis

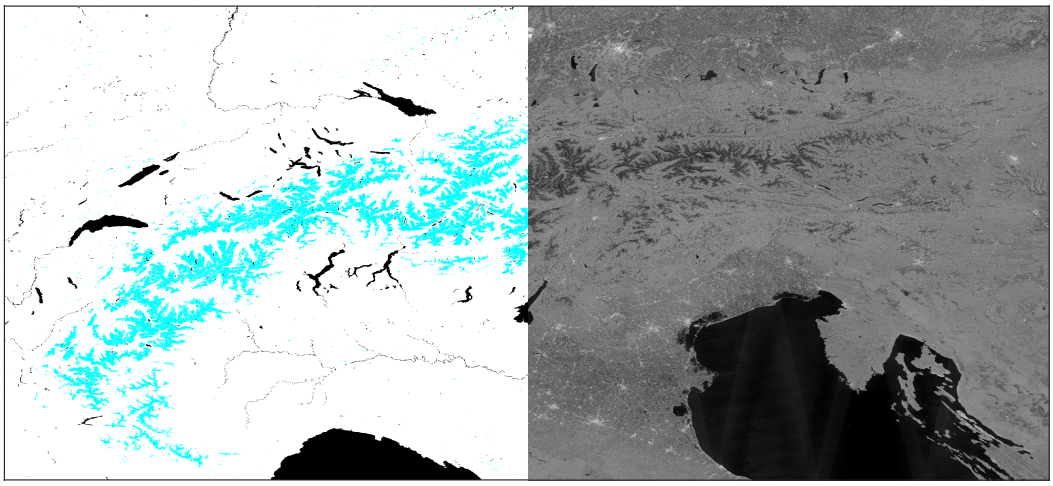

12. August 2016

Submitted by

David Jäger

07-919-715

Supervised by

Dr. David Small

Faculty member

Prof. Dr. Michael E. Schaepman

Abstract

Knowledge of the extent and duration of snow cover is important for a number of applications, including climate change research, hydroelectric planning and prediction of avalanches and flooding. Optical remote sensing is widely used for operational snow monitoring; however, its applicability is limited by cloud cover and illumination conditions. Synthetic Aperture Radar (SAR) sensors offer weather- and time-independent observation capabilities for wet snow cover. Numerous studies have demonstrated the applicability of C-band SAR imagery for wet snow mapping, but they usually only examined small-scale investigation areas. In the present thesis, a local resolution weighting (LRW) approach was used to produce composite images from Sentinel-1A C-band SAR data, covering the entirety of the European Alps with a single image. Subtracting a dry snow or snow-free reference image from these composites and applying a suitable threshold allowed the production of wet snow maps. Several algorithm improvements were introduced and assessed in order to address issues arising from the inclusion of a wide variety of land cover classes and climate regimes within a single, wide-area investigation scene. The final wet snow mapping algorithm presented here incorporates external data on land cover, elevation, temperature and snow cover and is able to produce unsupervised wet snow classifications from LRW composite time series spanning an entire melting season. Algorithm application to 16-day LRW composites from the melting seasons of 2015 and 2016 revealed good performances, reaching mean user's accuracies over the entire snowmelt period of 76% for 2015 and 79% for 2016 when compared to MODIS snow cover products. Some limitations were identified due to the relatively long temporal baseline of 16 days of the LRW composites. Availability of Sentinel-1B and RADARSAT constellation data in the near future will greatly reduce the composite period length. With those additional data sources, the method presented here will allow weather-independent wet snow mapping with high temporal and spatial resolution over wide areas.

Table of Contents

Figures

Tables

1 Introduction

The extent and duration of snow cover has far-reaching influence on climate, hydrology, ecology and economy on both global and local scale. On a global level, it plays an important role in controlling the planetary albedo and is therefore an important factor in Earth's energy balance (Rees, 2005). Snow cover further influences soil moisture and temperature, vegetation growth conditions and permafrost. It shows high sensitivity to changes in temperature and precipitation and is therefore a good indicator of climate variability and change. Consequently, snow cover was included as an important climate variable into the Global Climate Observing System GCOS (WMO and GCOS, 2011). On a local level, snow plays an important role as water storage for drinking, irrigation and hydroelectricity. Knowledge of the extent and state of snow cover in mountainous areas is crucial for predicting avalanches and flooding. It can also have direct economic influences, both beneficial (e.g. through skiing and other winter recreations) and adverse (e.g. through disruption of roads and railways) (Rees, 2005).

For these reasons, continuous observation of snow cover is an important objective. Monitoring by means of traditional field surveying methods can yield very detailed and accurate measurements, but is generally time-consuming and costly. Additionally, those methods usually only acquire point measurements, which may not be representative for a larger area (Snehmani et al., 2015). Remote sensing has proven to be a suitable tool for operational snow monitoring. The first snow map derived from satellite imagery dates back to 1960 and routine space-borne snow monitoring has been done since 1966 (Rees, 2005). Most snow monitoring systems that are operational today use passive sensors that measure the visible and infrared part of the electromagnetic spectrum. These systems are well suited for snow detection, as they can exploit the high reflectance of snow in the visible part of the electromagnetic spectrum. Multispectral sensors can additionally utilise the characteristic drop of snow reflectance in the short-wave infrared, which is particularly helpful to discriminate between snow cover and clouds (Rees, 2005; Dietz et al., 2012). The large number of available optical satellite systems allows snow mapping in a variety of spatial and temporal resolutions. However, the applicability of optical snow mapping is impaired by the presence of clouds, limited daylight, mountain shadow and bad illumination conditions induced by topography and weather (Rees, 2005; Dietz et al., 2012; Snehmani et al., 2015). These limitations can be overcome by using microwave sensors, as radiation from the microwave spectrum is independent of daylight and able to penetrate clouds. Passive microwave sensors have been used since 1978 to map snow cover through clouds and at night, but they are severely limited in terms of spatial resolution and maximal depth of the mapped snow pack (Rees, 2005; Dietz et al., 2012). Active microwave sensors, such as Synthetic Aperture Radar (SAR) sensors, achieve much higher spatial resolutions and offer weather- and time-independent observation capabilities. For this reason, increasing effort has been invested over the last decades to develop a reliable snow mapping method based on SAR satellite data.

1.1 Current state of research

The potential of SAR imagery for snow monitoring applications has been discussed since the early 1980s. Investigation of backscatter signatures based on scatterometer measurements revealed a general decreasing trend of backscatter coefficient with increasing snow wetness (Stiles & Ulaby, 1980). Experiments with airborne X-band SAR confirmed those findings and demonstrated the capabilities of SAR to detect wet snow cover (Mätzler & Schanda, 1984). These early studies also revealed the limitations of SAR imagery for detecting dry snow. Subsequent studies therefore focussed mostly on the occurrence of wet snow during snowmelt season.

With the launch of the European Remote Sensing satellite ERS-1 in 1991 and ERS-2 in 1995, continuous monitoring of the earth's surface with C-band SAR became possible. While SAR-systems operating in X-band generally offer better separability of wet snow from snow-free areas, C-band SAR was found to be adequate for wet snow mapping (Shi & Dozier, 1993). Rott and Nagler (1995) introduced a method to extract wet snow from ERS-1 images by calculating the ratio between an image containing wet snow and a reference image featuring only dry snow or snow-free areas and applying a suitable threshold to the ratio image. Similar approaches were subsequently successfully applied in multiple studies based on ERS data (e.g. Baghdadi et al., 1997; Nagler & Rott, 2000; Piesbergen, 2001), on ENVISAT ASAR data (e.g. Storvold & Malnes, 2004; Nagler & Rott, 2005; Longpépé et al., 2009), on RADARSAT data (Pivot, 2012) as well as on COSMO SkyMed images (Schellenberger et al., 2012; Notarnicola et al., 2013). Recently, Nagler et al. (2016) demonstrated the suitability of this approach for the newly launched Sentinel-1A platform. Alternative approaches to SAR-based wet snow mapping were also proposed, using SAR interferometry (Strozzi et al., 1999) and polarimetry (Park et al., 2014). However, the rationing approach with subsequent application of a suitable threshold remains the most widely used method to date for deriving wet snow cover from radar imagery.

1.2 Aim

While the capabilities of SAR imagery for wet snow mapping have clearly been demonstrated, most studies to date were confined to using data acquired within a single satellite track. This did not only limit the size of the study areas to the local scale, but also led to data gaps in complex terrain due to radar shadow and layover effects. Small (2012) introduced a Local Resolution Weighting (LRW) method that allowed to combine SAR images from multiple ascending and descending orbits into one composite image, thereby overcoming both of those limitations (see chapter 2.2.2). Schaub (2011) and Rohner (2014) demonstrated the general suitability of such LRW composites based on ENVISAT ASAR and RADARSAT-2 data for wet snow mapping. However, they applied the largely unaltered method introduced by Rott and Nagler (1995) with one single wet snow threshold to LRW composites covering the extent of Switzerland. This approach could be problematic, as the expansion of the study area from local to national scale increased the di-

versity of land cover classes and climate regimes contained within a single composite image. This might necessitate the application of adjusted algorithm settings for different regions within the study area. Furthermore, the inclusion of different land cover types and temperature regimes within a single image might necessitate a more careful selection of data to be used as dry snow reference than suggested by the standard method, in order to avoid wet snow contamination of the reference image. These implications caused by an expansion of the study area have not yet been investigated. The present study aimed to close this gap by implementing and testing several adjustments to the standard wet snow thresholding method and incorporating additional data sources such as optically derived snow maps, temperature data, terrain model and land cover information. Usage of the dense SAR image time series available from the new Sentinel-1A satellite allowed a further expansion of the study area beyond the national scale, covering the entirety of the European Alps. The following research questions were formulated:

1. *What is the performance in terms of classification accuracy of a wet snow mapping algorithm based on backscatter thresholding of Sentinel-1 Local Resolution Weighting (LRW) composite images in the Alps?*
2. *How can the wet snow detection algorithm be improved by*
   a) *adding further input datasets?*
   b) *improving the quality of the dry reference backscatter image?*
   c) *adjusting backscatter difference thresholds?*
   d) *combining VH and VV polarisations?*
   e) *shortening the composite time period?*
   f) *using 250 vs. 500 meter resolution MODIS snow products?*

1.3 Thesis structure

The study area and all used datasets are described in chapter 2. In chapter 3 the applied methods to produce the necessary input datasets as well as the actual snow mapping algorithm are explained. Results are presented in chapter 4 and synthesised and discussed in chapter 5. Finally, the most important conclusions are summarised in chapter 6 and an outlook to possible further research is given.

2 Data

2.1 Study area

The study area covered the European Alps and adjacent regions. It was defined by a rectangle spanning from 43.5° N / 5.5° E (south-west corner) to 49° N / 17.5° E (north-east corner). It covered the entirety of Switzerland, Liechtenstein, Austria, Slovenia and San Marino as well as parts of France, Italy, Germany, the Czech Republic, Slovakia, Hungary, Croatia and Bosnia-Herzegovina (see Figure 1). The total land area was 563'000 km^2, with elevations ranging from 0 – 4810 m.a.s.l.

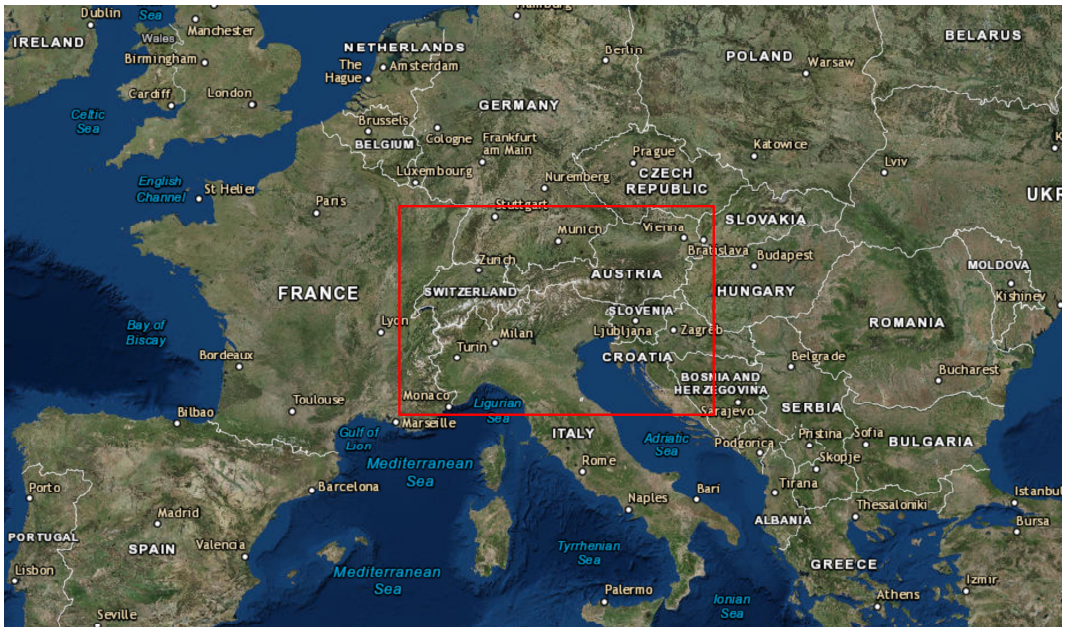

Figure 1. Study area (red box) in the larger European context (Source: ESRI, 2015).

2.2 Sentinel-1 SAR data

2.2.1 Sensor overview

The Sentinel-1 mission consists of two identical Satellites, carrying C-band Synthetic Aperture Radar (SAR) sensors. They are part of the European Earth observation program Copernicus and are operated by the European Space Agency (ESA). Sentinel-1A was launched on the 3rd of April 2014, Sentinel-1B followed on the 25th of April 2016 (ESA, n.d.). They fly on the same sun-synchronous, near polar orbit at 693 km altitude, with a 180-degree orbital phasing difference. The repeat cycle for each satellite is 12 days, a combination of both satellites will achieve 6-day repeat pass observations (Torres et al., 2012).

The Sentinel-1 SAR sensor operates in the C-band at a centre frequency of 5.405 GHz. It can be operated in four different imaging modes, providing different coverage and spatial resolutions: Interferometric Wide-swath mode (IW), Wave mode (WV), Strip Map mode (SM) and Extra Wide-swath mode (EW). The IW mode is the nominal operation mode over land areas and achieves a geometric ground resolution of 5 m x 20 m within a swath width of 250 km. Data is usually acquired in dual-polarisation mode over Europe (Torres et al., 2012). At the time of writing, Sentinel-1B is still in its in-orbit commissioning phase. Therefore only Sentinel-1A data was used in this thesis.

2.2.2 Local Resolution Weighting (LRW) composites

In complex terrain like the Alps, single SAR acquisitions typically suffer from severe distortions in geometry due to foreshortening and layover-effects. These distortions are

traditionally corrected by resampling the data into a map geometry, using a Digital Elevation Model (DEM). This results in a Geocoded Terrain-Corrected (GTC) product (Meier et al., 1993). Aside from geometric distortions, complex topography also influences the radiometry of a SAR scene, which is not accounted for by the GTC approach. To normalize those radiometric distortions, Small (2011) introduced an approach to produce Radiometrically Terrain-Corrected (RTC) images. This method uses the highly accurate state vectors of modern SAR satellites and a high-resolution DEM to produce a simulated radar geometry image that models the effects of terrain on the backscatter. This simulated image is then applied to a SAR acquisition to compensate the terrain-induced backscatter differences. Land-cover induced backscatter differences are more easily retrieved from the resulting flattened RTC image, enabling the comparison of land-cover signatures over larger areas and even between multi-track acquisitions (Small, 2011).

While the RTC approach has been proven to effectively compensate for geometric and radiometric distortions caused by topography, it cannot compensate for the terrain-induced variations of local resolution and data gaps due to radar shadow. RTC images do however allow an easy joining of images from multiple acquisitions, both from different satellite tracks as well as from ascending and descending orbits. Since regions seen as foreslopes in ascending orbits are typically viewed as backslopes in descending acquisitions, a combination of the two orbits presents great potential to compensate for locally varying resolution and data gaps. Small (2012) developed a method to combine RTC-flattened radar images from multiple ascending and descending tracks into one composite image, thereby trading off temporal resolution for increased local spatial resolution and larger scene extents. This Local Resolution Weighting (LRW) approach computes the weighted sum of all contributing flattened backscatter observations, whereby images with higher local resolution are given a proportionally higher local weight. The weighting is done in such a way that all available acquisitions contribute to the final composite, thereby reducing noise and increasing the Equivalent Number of Looks (ENL). The applicability of this approach has been demonstrated using ENVISAT ASAR wide swath and Radarsat-2 imagery acquired over Switzerland (Small, 2012).

In the present thesis, pre-processed Sentinel-1A LRW composites covering the entire study area were used. A time series starting on the 30th of September 2014 and running through June 2016 was available, with data acquired in cross-polarisation (VH) as well as in like-polarisation (VV). The data was reprojected into geographic latitude/longitude coordinates, with a spatial resolution of 3x3 arc-seconds (roughly 90 Meters). Two temporal aggregation levels were used: 1) composites of images acquired over an 8-day period with a four-day overlap with the previous and subsequent acquisition period, and 2) composites over a 16-day period and eight days of temporal overlap. The periods were chosen to match the dates of the MODIS snow product MOD10A2 (Riggs et al., 2006; see chapter 2.3). The 16-day LRW composite represented a good compromise between maximum data coverage of the study area and short time span. While most images still contained data gaps in the first half of the time series, the composite scenes were gap-free

from the 9th of November 2015 onwards. The total scene coverage of the 16-day composites varied between 82.3% and 100%. The 8-day composites offered a better temporal resolution, but at the cost of some very large data gaps, with coverage ranging from 50.1% to 100% (see Figure 2). In addition to the large data gaps, the 8-day composites were expected to feature a generally higher noise level compared to the 16-day images due to the smaller amount of spatial overlap of the single SAR acquisitions.

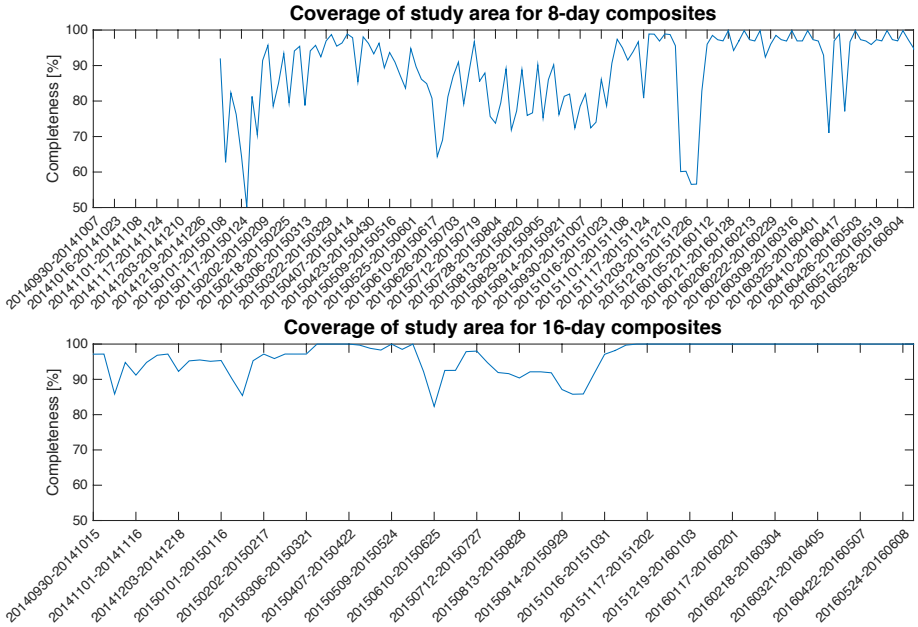

Figure 2. Coverage of the study area by the Sentinel-1A SAR composite images.

2.3 MODIS snow product

Snow products derived from optical imagery were used as part of the wet snow mapping algorithm as well as for comparison with the SAR-derived snow maps. All optically derived maps used here were based on Moderate Resolution Imaging Spectroradiometer (MODIS) imagery.

MODIS is a space-borne, multispectral optical instrument operated by the National Aeronautics and Space Administration (NASA). It observes the entire Earth every one to two days in 36 spectral bands. Spatial resolution ranges from 250 m (bands 1-2) over 500 m (bands 3-7) to 1000 m (bands 8-36) (NASA, n.d.). The first MODIS instrument was launched aboard the Terra satellite on the 18th of December 1999 and has been continually collecting data to the present (NASA, 2016b). A second MODIS instrument was launched aboard Terra's sister satellite, Aqua, on the 4th of May 2002, and has also remained operational to date (NASA, 2016a).

2.3.1 NASA MODIS snow product

NASA offers a variety of snow products derived from MODIS imagery acquired by the Terra and Aqua platforms. The snow detection is based on the Normalized Difference Snow Index (NDSI), which is defined for MODIS imagery as

$$NDSI = \frac{band\ 4 - band\ 6}{band\ 4 + band\ 6}.$$

Since band 6 on Aqua is only partly functional, the NDSI for Aqua acquisitions are calculated by using band 7 instead of band 6 (Hall & Riggs, 2007). Snow is detected by applying suitable thresholds to the NDSI. Additional, individual thresholding of band 2 and band 4 prevent erroneous snow classification of surfaces with low reflectance (e.g. water surfaces) that might have a high NDSI value. For detection of snow in dense vegetation, additional criteria are implemented. Forested pixels are classified as snow if the scatterplot values of the NDSI and the Normalized Difference Vegetation Index (NDVI) lie within a defined polygon, and where band 1 and band 2 reflectance are above a fixed threshold. Finally, any wrong classifications of bright warm surfaces as snow are corrected by applying a surface temperature screen. The final snow product is available with temporal resolutions of one day, eight days and one month, and with spatial resolutions of 500 m in the sinusoidal grid or 0.05° in the climate modelling grid (Hall et al., 2001; Riggs et al., 2006). The 500 m daily product achieves an overall absolute accuracy of about 93%. Lower accuracies are found in forested areas and complex terrain, while higher accuracies of up to 99% have been observed in cropland and agricultural areas (Hall & Riggs, 2007).

In the present study, the MODIS 8-day snow product MOD10A2 from collection five was used (Riggs et al., 2006). This product is based on daily 500 m resolution snow cover maps (sinusoidal grid), classified by the algorithm described above, that were then combined into an 8-day composite image. If snow cover was detected in a pixel on any day during the 8-day period, then the cell is labelled as *snow* in the composite, regardless of whether it was classified as snow on any other day of the period. The composite therefore represented the maximum snow extent during the 8-day period. Cells that were cloud covered during all eight days were marked as *cloud*. In addition to the maximum snow extent, the data files also featured a second band containing an 8-bit "chronobyte" image, where each bit represented one day during the 8-day composite period. If the pixel was classified as *snow* on a particular day, the corresponding bit was set to one. This allowed the extraction of the total number of days during the 8-day period where a pixel was detected as snow covered (Riggs et al., 2006). Based on this "chronobyte" image, an additional set of data spanning 16 days was produced, matching the date ranges of the 16-day SAR composites. Since this was twice the time span of the MOD10A2 product, the required minimal number of days of snow detection per pixel was also doubled. This meant that a pixel had to be detected as snow covered on at least two days during the 16-day period in order to be labelled as *snow*. Accordingly, a pixel had to be cloud-free for at least two days during the 16-day period, otherwise it was marked as *cloud*.

Only data from Terra was used in this study, as Aqua data suffered from the non-functional band 6 and therefore showed more noise (Hall & Riggs, 2007). The study area was completely covered by MODIS tiles h18v04 and h19v04. They were downloaded for the entire available MOD10A2 time series from the 26th of February 2000 to the 8th of June 2016. The tiles were then mosaicked and reprojected into geographic coordinates using the open source Geospatial Data Abstraction Library (GDAL). The original 500 m resolution was resampled to 3x3 arc-second resolution using nearest neighbour resampling method and cropped to the investigation scene extent, so that it matched the Sentinel SAR data both in extent and in spatial resolution.

2.3.2 EURAC MODIS snow product

The Institute for Applied Remote Sensing at the European Academy (EURAC) in Bozen, Italy, produced a snow product that was based on the same MODIS data as the NASA products, but used a different approach to identify snow. Instead of using the NDSI, snow detection was done using only MODIS bands 1 (red) and 2 (infrared). This allowed exploitation of their higher spatial resolution of 250 m compared to the 500 m resolution of bands 4 and 6 used for the NDSI, resulting in a snow map with higher spatial resolution (Notaricola et al., 2013b). Bands 1 and 2 were combined to calculate the NDVI:

$$NDVI = \frac{band\ 2 - band\ 1}{band\ 2 + band\ 1}.$$

To detect snow, thresholds were applied to the NDVI. In non-forested areas, a single global threshold was applied. In forested areas, individual NDVI-thresholds were used for coniferous, deciduous and mixed forests. Additionally, a multi-temporal approach was applied, where the ratio of the image to be classified was compared to a snow-free reference image. Cloud detection was done using the NDSI based on bands 4 and 6 as well as the 1000 m resolution emissive bands 20, 21, 26, 31, 32. Finally, the snow maps produced for MODIS Aqua and Terra data were combined to utilize the half-day acquisition time difference between the two sensors, reducing cloud coverage as well as the number of non-classified pixels (Notarnicola et al., 2013a). The resulting 250 m resolution snow maps achieved a mean overall accuracy of around 88.1% when compared to Landsat 7 ETM+ images and around 93.7% when compared to ground measurements. Higher accuracies were achieved in open areas, while very rugged terrain with northern exposition and densely forested areas yielded lower accuracies (Notaricola et al., 2013b).

For this study, daily EURAC snow cover maps for the entire year 2015 were available. Only 63% of the Sentinel-1 study area was covered by the EURAC data (see Figure 3). The daily maps were combined to the same 8-day periods as the NASA snow product, using the same combination rule as for the NASA data (i.e. if a pixel was marked as *snow* on one day, it was marked *snow* for the entire 8-day period). A second set of data spanning 16 days was produced in the same manner as for the NASA-data (i.e. if a pixel was marked as *snow* for at least two days during the 16-day period, it was marked as *snow* in the composite image). The composites were then reprojected, resampled and cropped

analogue to the NASA data, so that resolution and extent matched the Sentinel SAR data (missing areas were filled with NoData-values).

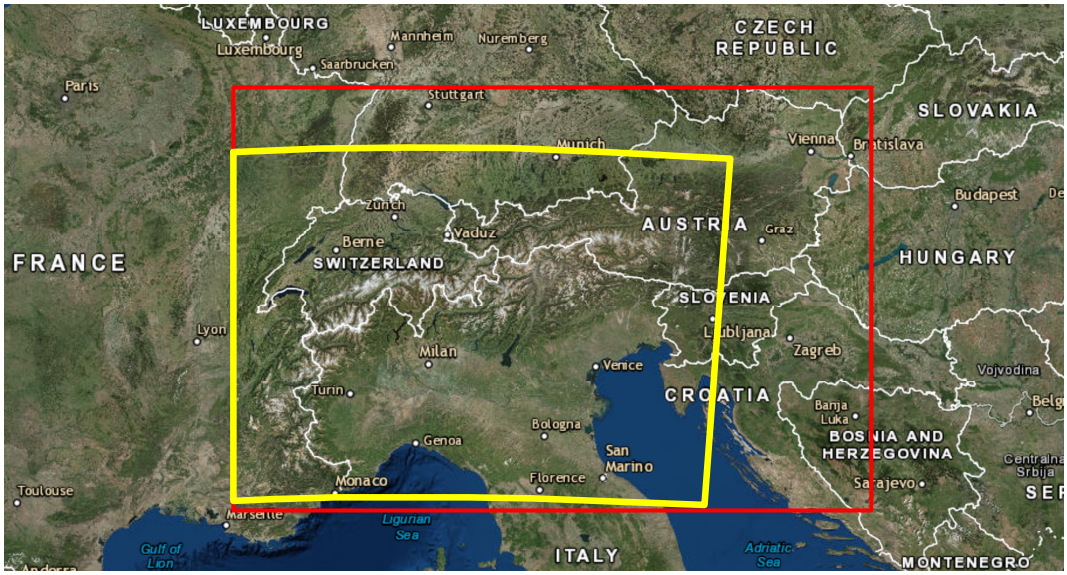

Figure 3. Comparison of EURAC snow cover data extent (yellow box) with the study area (red box) (Source: ESRI, 2015).

2.4 Digital Elevation Model (DEM)

A Digital Elevation Model (DEM) derived from the Shuttle Radar Topography Mission (SRTM) was used. This mission, a joint endeavour of NASA, National Geospatial-Intelligence Agency, and the German and Italian Space Agencies, flew in early 2000. It used interferometric radar to derive a global, high-resolution DEM at a maximum spatial resolution of one arc-second (Farr et al., 2007). The data used in this study had a spatial resolution of three arc-seconds and was cropped to the investigation scene extent.

2.5 CORINE land cover map

Information on land cover used in this thesis was extracted from the Europe-wide CORINE land cover (CLC) map, produced for the Copernicus land monitoring services. The latest available map was produced with data from 2011 and 2012. It classified land and water surfaces into 48 land cover classes, based on satellite data from IRS, SPOT and RapidEye, as well as from orthophotos and topographic maps. The map was available in 100 m spatial resolution and achieved a reported thematic accuracy of at least 85% (Büttner et al., 2014).

The land cover map was reprojected, resampled and cropped with GDAL in order to match the spatial resolution and extent of the Sentinel SAR composites. Resampling was done using the nearest neighbour approach. The land cover classes were then aggregated into seven classes:

- urban areas: CLC classes 1 – 11
- agricultural land: CLC classes 12 – 22
- forests: CLC classes 23 – 25
- scrubland: CLC classes 26 – 29
- natural non-vegetated areas: CLC classes 30 – 33
- glaciers & perpetual snow: CLC class 34
- water surfaces: CLC classes 40 – 44

Wetlands (CLC classes 35 – 39), unclassified pixels and missing data (CLC classes 45 – 48) only occurred in insignificant extents within the study area and were therefore neglected.

2.6 ERA-Interim temperature data

Temperature data used in this study was derived from the global atmospheric reanalysis ERA-Interim, produced and distributed by the European Centre for Medium-Range Weather Forecasts (ECMWF). This reanalysis featured a multitude of surface and upper-air parameters describing weather, ocean-wave and land-surface conditions. It was produced by assimilating various satellite and *in situ* data with forecast model outputs. The data was available globally in various spatial resolutions and a temporal resolution of three or six hours, depending on the parameter. The time series started in 1979 and has been continually updated to the present (Berrisford et al., 2011; Dee et al., 2011).

6-hourly maps of temperature two meters above ground were available from ERA-Interim at a maximum spatial resolution of 0.125x0.125° in geographic coordinates. While this dataset gave a good overview of the regional temperature conditions, the spatial resolution was too coarse to adequately represent the actual surface temperature in complex terrain like the Alps. A resampling method considering terrain variation was therefore required to downscale the temperature data to match the 3x3 arc-second spatial resolution of the SAR data. The applied method is described in chapter 3.1.1.

To validate the resampled temperature maps, a total of 80’630 surface temperature measurements from 111 automated weather stations scattered over Switzerland were retrieved from the CLIMAP-portal provided by MeteoSchweiz (MeteoSchweiz, 2014). The measurements were recorded over one year (1st October 2014 to 30th September 2015), with daily acquisitions at 06:00 UTC and 18:00 UTC.

3 Methods

Microwave radiation interacts with snow cover in a complex manner. The backscatter measured by a SAR antenna can be described as the sum of surface scattering at the snow surface, volume scattering within the snowpack and scattering at the snow-soil interface. Those contributors are in turn influenced by radar wavelength, snow grain size and liquid water content of the snow pack (Hall 1996). In C-band, the dominating factor is the snow

wetness, i.e. the amount of liquid water within the snow pack. Microwaves in the C-band spectrum can penetrate dry snow to a depth of about 20 meters, whereas the penetration depth in wet snow with liquid water content of 5 volume-% is reduced to a few centimetres (Mätzler, 1986). This means that for remote sensing applications, dry snow is largely transparent and therefore not detectable for C-band radar. Wet snow on the other hand typically reduces the backscatter intensity significantly due to high dielectric losses caused by the liquid water content within the snow pack (Mätzler & Schanda, 1984). This allows the mapping of wet snow cover by means of multitemporal change detection. A reference image taken during snow-free or dry-snow conditions is hereby subtracted from an investigation image acquired during snowmelt. This removes backscatter variations caused by topography and land cover; ideally only backscatter differences caused by dielectric losses in wet snow remain. A wet snow cover map can then be extracted from this difference image by applying a suitable threshold.

This approach was introduced by Rott & Nagler (1995) and applied to ERS-1 C-band data acquired over the Austrian Alps. Baghdadi et al. (1997) used a similar approach for ERS-1 data taken over a study area in southeastern Québec, Canada. Similar approaches have later been successfully adapted to ENVISAT ASAR data (e.g. Storvold & Malnes, 2004; Nagler & Rott, 2005; Longpépé et al., 2009), to RADARSAT data (e.g. Pivot, 2012), to COSMO SkyMed images (Schellenberger et al., 2012; Notarnicola et al., 2013) and recently to Sentinel-1A data (Nagler et al., 2016). While those studies demonstrated the general applicability of this method for C-band SAR, they mostly featured a limited spatial extent and typically only analysed acquisitions from a few points in time. The multitemporal approach required repeat-pass acquisitions in a single geometry, which limited the number of useable acquisitions and complicated an analysis beyond single-track collection. In the present thesis, LRW-composites (see chapter 2.2.2) were used as input data instead of single-track SAR acquisitions. This allowed the mapping of wet snow over a wide area while removing the need for exact repeat-pass acquisitions, therefore enabling the utilisation of all available images taken over the study area. The method was further refined by incorporating auxiliary data products from other sensors, allowing an efficient wide-area mapping of wet snow for an entire time series.

Figure 4 gives an overview of the input datasets and processing steps used in the present study. Aside from any necessary pre-processing, the processing can be split into five main parts: 1) a backscatter difference image time series was produced by pixel-wise subtraction of the flattened γ^0 reference backscatter from γ^0 of the investigation scene; 2) a DEM and the CORINE land cover classification was used to mask out certain areas and section the remaining area of every difference image into regions; 3) temperature data and the MODIS snow cover product were used to mask out snow-free areas and thus amplify the backscatter differences between wet snow and dry/no snow in order to extract thresholds for each region from the time series; 4) the thresholds were applied to every difference image of the time series; 5) a post-classification correction of misclassified pixels based on the mean length of snow season for each pixel, extracted from the 15-year MODIS

time series, was applied. The result was a time series of wet snow cover maps that allowed the investigation of retreating snow cover during the melting season. In the following sub-chapters, the individual steps of the workflow are described in detail.

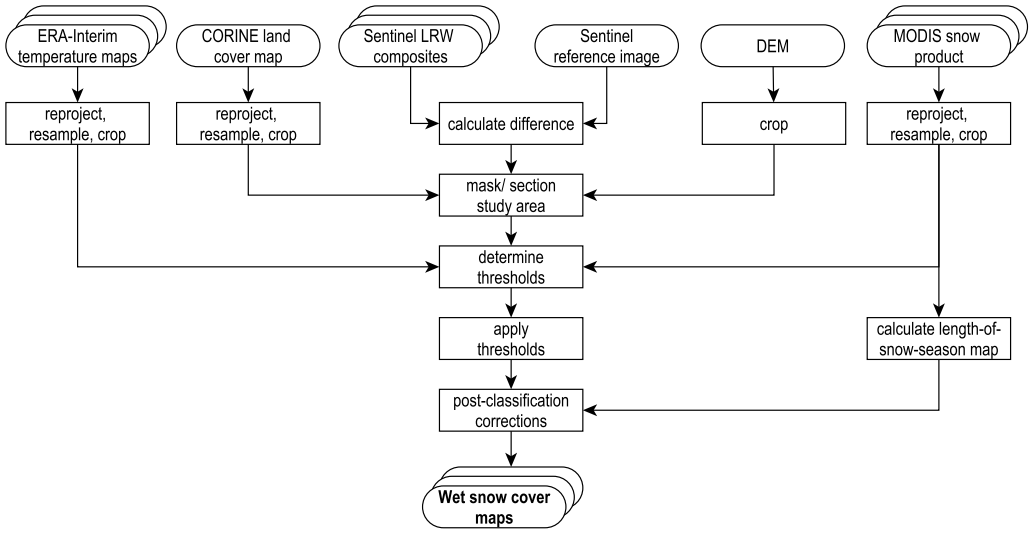

Figure 4. Overview over all input datasets and processing steps.

3.1 Radar pre-processing and data preparation

The Sentinel LRW composites were already calibrated and georeferenced level 3 products, so that pre-processing was confined to converting the backscatter into the logarithmic decibel (dB) domain. The map projection and resolution of the LRW data was used as the target grid for all other datasets.

The auxiliary data products used in this study were level 3 products with a sufficient degree of georeferencing accuracy. A separate co-registration step was therefore not necessary. Pre-processing of this data was limited to reprojection into the target grid, cropping to the scene extent and resampling to match the target resolution. With the exception of the temperature data, resampling was done using the nearest neighbour approach, in order to preserve the original data content. The temperature data needed to be resampled with a more complex approach in order to achieve the necessary level of detail. This resampling approach is described below.

3.1.1 Resampling of the ERA-Interim temperature data

The best available spatial resolution of the ERA-Interim surface temperature data was 0.125x0.125° (or 450x450 arc-seconds) in geographic coordinates. While this gave a good overview of the regional temperature distribution, it was too coarse to adequately represent the local changes in surface temperatures due to complex terrain. A downscaling method developed by Gao et al. (2012) using a DEM and the local lapse rate was therefore used to resample the temperature data to match the 3x3 arc-second spatial reso-

lution of the SAR images. The DEM described in chapter 2.4 was used for this purpose. Additionally, the following ERA-Interim input datasets were used:

- t2m: temperature two meters above ground
- t700: temperature at the 700 hPa pressure level
- t850: temperature at the 850 hPa pressure level
- t925: temperature at the 925 hPa pressure level
- z700: geopotential at the 700 hPa pressure level
- z850: geopotential at the 850 hPa pressure level
- z925: geopotential at the 925 hPa pressure level

Only data for 06:00 UTC and 18:00 UTC was used, as those times coincided roughly with the ascending and descending passes of Sentinel-1A over the study area. A complete time series spanning from the 1st of October 2014 to the 29th of February 2016 was available. As the data was already georeferenced, no further pre-processing needed to be done.

The resampling method was implemented as described by Gao et al. (2012). First, the geopotential data was converted to geopotential height by dividing each grid cell by the gravitational acceleration g. Next, the local lapse rate Γ was calculated for the different pressure levels (PL) by dividing the temperature difference (ΔT) of two pressure levels by the difference in geopotential height (Δz) of the same pressure levels:

$$\Gamma = \frac{T_{PL1} - T_{PL2}}{z_{PL1} - z_{PL2}}.$$

Next, the mean elevation h_{450s} of every 450x450 arc-second ERA-Interim grid cell was calculated by averaging the DEM-values contained within each pixel. Based on this, the elevation difference Δh between the mean elevation and the actual DEM elevation h_{3s} at each 3x3 arc-second grid cell was calculated:

$$\Delta h = h_{450s} - h_{3s}.$$

Finally, the temperature data could be resampled to the higher spatial resolution by calculating the height-corrected temperature T:

$$T = T_{ref} + \Gamma * \Delta h.$$

At lower altitudes, temperature conditions are mainly influenced by local circulation patterns, while at higher elevations they are more representative of free airflow. The boundary layer between those two conditions usually lies at approximately 1500 m.a.s.l., which corresponds roughly to the 850 hPa pressure level. To account for those conditions, different reference temperatures and lapse rates were used for different elevations (see Table 1).

Elevation	Reference temperature T_{ref}	Lapse rate Γ
< 1500 m.a.s.l.	t2m	$\Gamma_{850hPa-925hPa}$
> 1500 m.a.s.l.	t850	$\Gamma_{700hPa-850hPa}$

Table 1. Reference temperatures and lapse rates for different elevations.

The resulting temperature maps contain some artefacts caused by the larger ERA-Interim pixel size, but in general they appear to well represent the height-induced temperature differences (see example in Figure 5).

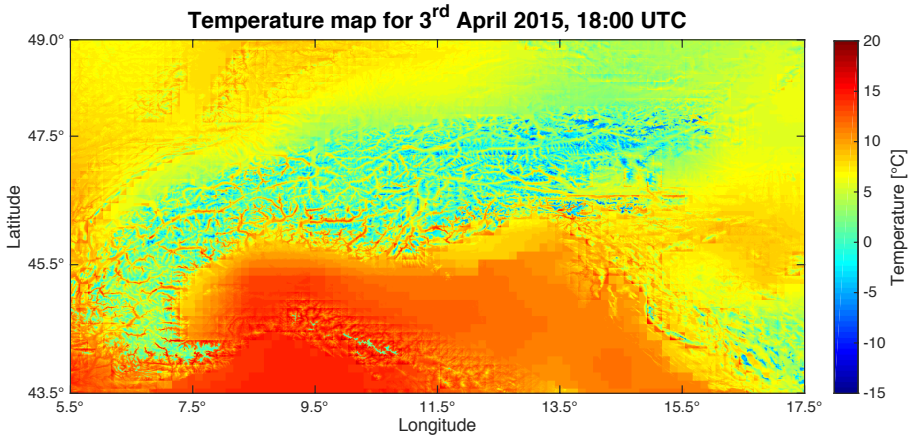

Figure 5. Example of resampled temperature map.

To validate the temperature maps, a comparison with measurements from weather stations was conducted. Surface temperature measurements were available from 111 automated weather stations scattered over Switzerland, spanning one year (1st October 2014 to 30th September 2015). Measurements from 06:00 UTC and 18:00 UTC were used as comparison values in order to match the reference times of the resampled ERA-Interim temperature maps. A total of 80'630 valid station measurements were available. A daily correlation analysis revealed good agreement between the resampled maps and the station measurements, with values for Pearson's r varying around a median of 0.71 with a mean deviation from the median of 0.09. Agreement was slightly lower during winter months and higher during summer months. When comparing the values over the entire year, a correlation of 0.91 was achieved. Over all, the resampled temperature maps were sufficiently accurate for the purposes of this study.

3.2 Backscatter reference image

The backscatter reference image represents the backscatter of the study area under snow-free and/or dry snow conditions. It is therefore typically either an image composited from summer acquisitions, where no snow was present, or from winter images acquired during freezing periods, when all the snow present in the scene was completely dry. Calculating the average of multiple acquisitions that meet the required conditions can reduce errors induced by temporal variations of backscattering and speckle (Nagler & Rott, 2000). The quality of the reference image is crucial, as any wet snow contamination will most likely lead to an erroneous snow classification at that location.

To assess which reference image was best suited for wet snow mapping, four different approaches were compared in the present study: 1) a simple summer reference, based on LRW composites acquired during summer months; 2) a simple winter reference, based on LRW composites acquired in winter during periods of lowest average temperature over

the study area; 3) a snow-adjusted summer reference, where any summer pixels with residual snow were replaced by winter pixels; and 4) an improved winter reference, where the selection of suitable acquisitions was based on temperature values on the pixel level instead of the average temperature over the entire scene. All reference images are printed in appendix A.2. The methods used to produce those reference scenes are described in detail in the following sub-chapters.

3.2.1 Simple summer reference image

Producing a reference image from summer acquisitions presented the simplest approach, as the vast majority of the study area was snow-free during summer months. This minimized the chance of wet snow contamination for most of the reference scene. However, due to the inclusion of high elevations in the study area, some areas were snow-covered year-round. These areas featured wet snow conditions during the warm summer months, which led to wet snow contamination of the reference scene. While this problem only affected small areas at high altitudes that accounted for roughly 0.3% of the total study area, these were exactly the regions of interest for wet snow mapping during late melting season. Furthermore, backscatter during summer was influenced by factors like vegetation, tree canopy and soil moisture, which were less prominent during the early melting season. This could lead to backscatter differences between investigation and reference image that were not caused by snow cover and might cause erroneous snow classification.

To minimize wet snow contamination, acquisitions from July and early August 2015 were used for the summer reference scene, as this was – according to the MODIS snow product – the time with the smallest extent of residual snow. The average of the 16-day composites from the following dates was calculated:

- 04.07. – 19.07.2015
- 12.07. – 27.07.2015
- 20.07. – 04.08.2015
- 28.07. – 12.08.2015

All of those images were acquired during a period when large persistent data gaps in the northern part of the study area impaired the completeness of the scene. As a consequence, the reference image produced from those four images only covered 98.2% of the entire study area (see Figure 6). The remaining data gap was filled with the average backscatter of the earliest two composites that featured data in the missing area and that were taken outside of the melting season. The image dates of those composites were

- 24.10. – 08.11.2015
- 01.11. – 16.11.2015

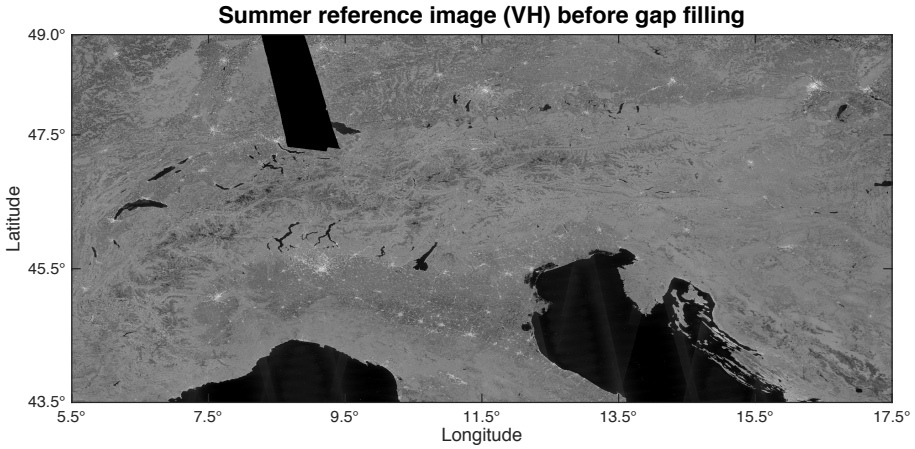

Figure 6. Summer reference (VH-polarisation) image with remaining data gap in the northwest quadrant.

3.2.2 Simple winter reference

Dry snow is largely transparent for C-band radar; therefore the backscatter does not change significantly between snow-free ground and ground covered by dry snow (Stiles & Ulaby, 1980). This allowed the use of cold winter acquisitions that only featured dry snow as reference images for wet snow mapping. The advantage over summer acquisitions was found to be that there were less disturbing influences from high vegetation growth, tree canopy and soil moisture. It was however more difficult to choose appropriate acquisitions, since only images taken during freezing conditions should be used as reference. This made it necessary to use auxiliary temperature data to find acquisition periods when temperatures were below zero degrees across a large region. Note, however, that this approach could be problematic, since it was based on the mean temperature over the entire study area. When the study area is as large as it was in the present study, a mean temperature of below zero degrees over the entire area does not necessarily mean that all parts of it are actually frozen. Therefore, some wet snow contamination was to be expected with this approach, particularly at lower elevations.

The resampled daily ERA-Interim temperature data was used to identify periods where the average temperature over the entire study area was below zero degrees. Three periods were identified where this condition was met: from the 27th of December 2014 to the 2nd of January 2015; from the 31st of January to the 9th of February 2015; and from the 16th of January to the 23rd of January 2016. To better match those relatively short time periods, 8-day LRW composites were used instead of 16-day composites. The winter reference image was produced by calculating the average of 8-day composites from the following dates:

- 01.01. – 08.01.2015
- 29.01. – 05.02.2015
- 13.01. – 20.01.2016
- 17.01. – 24.01.2016

Between those four images, the entire study area was covered with data; therefore no gap filling was necessary.

3.2.3 Snow-adjusted summer reference

The main problem with the summer reference was the residual snow in high altitudes, which would most likely lead to wet snow contamination in the reference image. The main problem with the winter reference was that even if all acquisitions were taken during a time when the mean temperature over the entire study area was below freezing, some parts, particularly in lower elevations, might still have been warmer and therefore feature wet snow contamination. Both those problems could be solved by producing the reference image from both summer- and winter acquisitions: summer images were used for lower elevations where no residual snow was found, while areas at high altitudes that were snow-covered year-round were replaced by winter acquisitions. Since only very high altitude pixels were replaced by the winter images, it was safe to assume that those areas were completely frozen in mid-winter. Therefore, the wet snow contamination of the used winter pixels should be very small.

The decision on the replacement of summer pixels by winter pixels could be made in one of two ways: either a fixed elevation threshold is chosen (e.g. 2000 m.a.s.l.) of which one can safely assume that below this elevation there will be no residual snow during summer months. Using a DEM, all pixels with elevations above this threshold are then replaced by winter image backscatter values. Alternatively, a decision based on external snow data can be made. This approach was used in the present study: The MODIS snow cover data was used to identify residual snow pixels in the summer images. These pixels were then replaced by corresponding pixels from the winter reference image.

3.2.4 Improved winter reference

The snow-adjusted summer reference might have solved the problem of wet snow contamination at high altitudes, but it still contained potentially distorting factors like high vegetation, tree canopy and soil moisture. This might lead to errors when mapping snow in early snowmelt season, because those factors are less prominent during this time period. It was therefore desirable to produce a reference image that was based solely on winter images, where wet snow contamination could be avoided by having more control over which SAR acquisitions were used. This could be achieved by using the full spatial information contained within the resampled ERA-Interim temperature data rather than just the average temperature over the entire study area.

Semi-daily temperature masks of freezing conditions were produced for the time series from October 2014 to February 2016, based on the resampled ERA-Interim temperature data from 06:00 UTC and 18:00 UTC. A conservative rule for *freezing conditions* was used: temperatures had to be below -1 °C for at least 24 hours, otherwise the pixel was masked out. This approach reduced errors due to inaccuracies in the resampled temperature data. The temperature masks were then applied to the flattened, but non-composited

Sentinel SAR acquisitions (ascending acquisitions were masked by the 06:00 UTC mask, descending acquisitions by the 18:00 UTC mask), producing a time series of SAR data where only pixels that featured data acquired during freezing conditions remained. A single LRW composite was then calculated over this entire time series of selected and masked images. The result was a winter reference image that should feature minimal wet snow contamination. The whole process is illustrated in the flowchart in Figure 7.

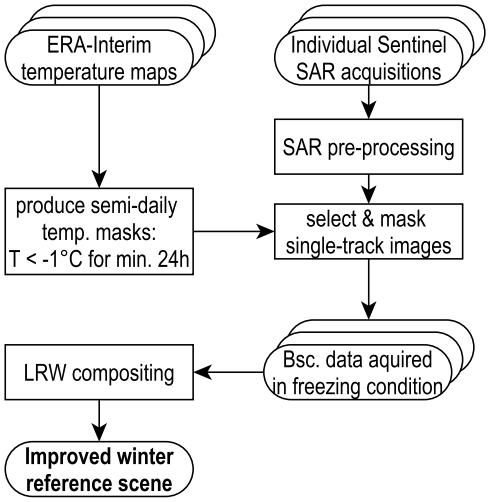

Figure 7. Flowchart illustrating the processing steps to produce the improved winter reference scene.

Unfortunately, the resulting reference image contained some large data gaps (see Figure 8a). Those gaps were filled in a two-step process:

1. A second set of temperature masks was produced, where a less conservative masking rule was applied (the temperature threshold was set at 0°C instead of -1°C and was based on the current temperature instead of the temperature over the last 24 hours). A second reference LRW was calculated based on those masks. Thanks to the less conservative masking, more data was available and therefore fewer data gaps occurred; however, it also increased the probability of wet snow contamination. The resulting LRW was used to fill as many gaps as possible in the first reference LRW.
2. Some gaps still remained after step one, as some areas in the south of the study area never experienced freezing conditions during the available time period. To avoid wet snow contamination, these gaps were filled using summer reference pixels.

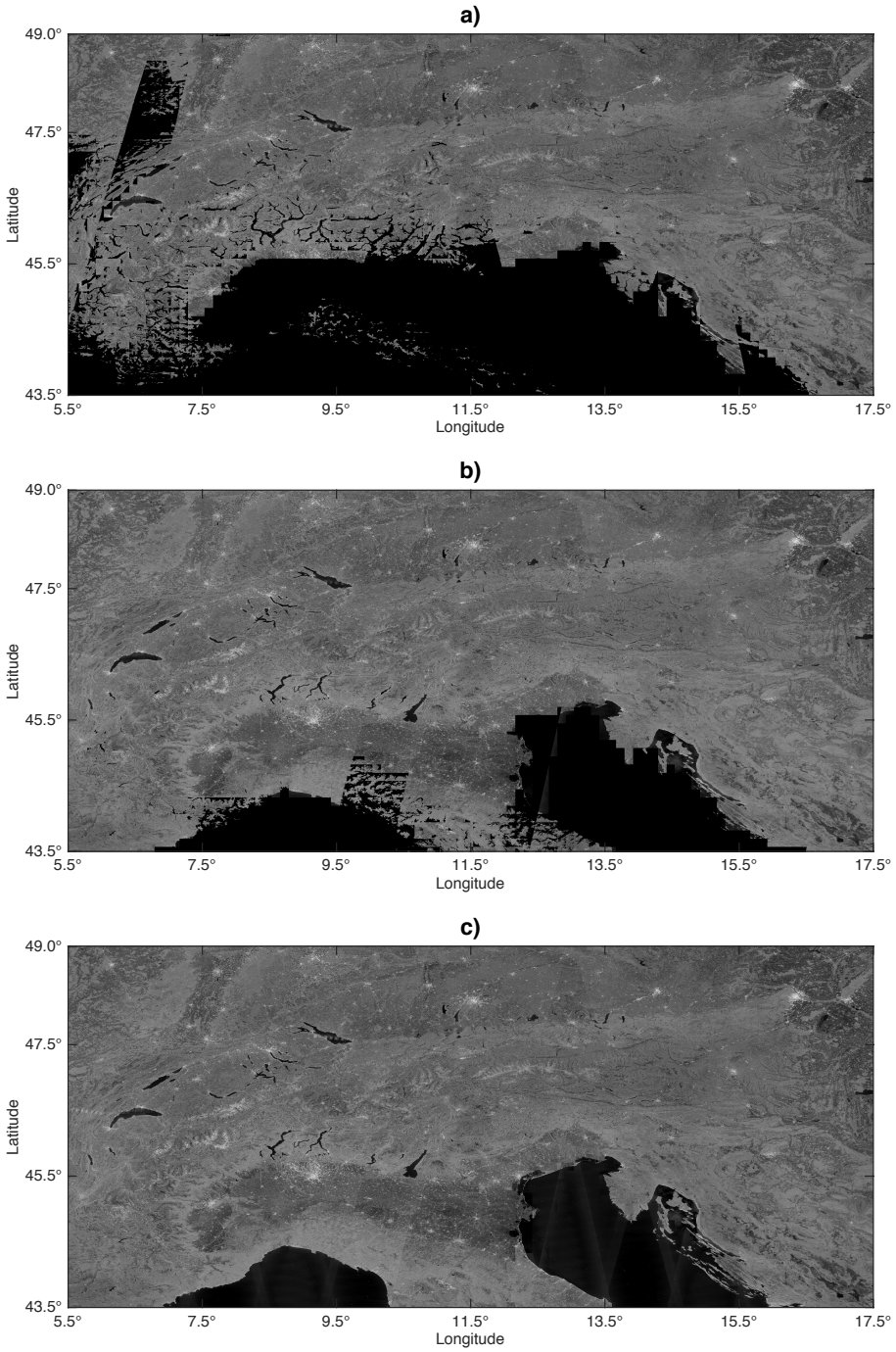

Figure 8. The three steps of the improved winter reference for VH-polarisation. a) LRW based on -1°C for 24h masking; b) gaps filled with LRW based on 0°C masking; c) final VH reference image, remaining gaps filled with summer images.

3.3 Wet snow threshold identification

The thresholds for wet snow discrimination were determined by comparing histogram peaks of SAR backscatter difference from cold and warm snow. The histograms were calculated for acquisitions spanning the extended melting period of the year 2015, which

was defined as starting with the first properly cold winter period on the 1st of January 2015 and running to minimum snow extent on the 4th of July 2015. Individual histograms were produced with all four reference images, for 8-day and 16-day time windows as well as for VH- and VV-polarisation. Figure 9 illustrates the processing steps that were applied to extract the wet snow thresholds.

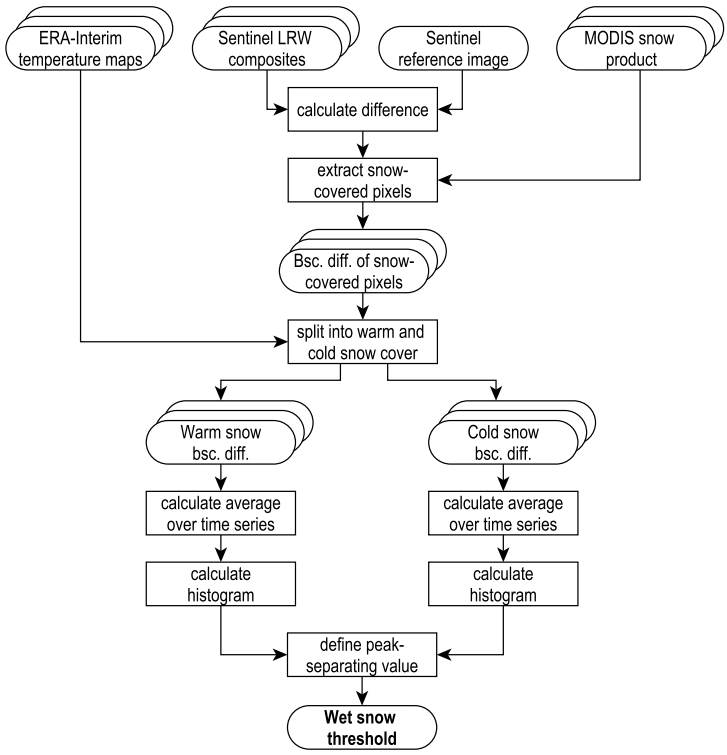

Figure 9. Processing steps applied to extract a suitable wet snow threshold.

The individual steps in more detail were as follows:

1. Subtracting the reference image from all LRW composites produced backscatter difference images.
2. To amplify the differences between cold and warm snow histogram peaks, snow free areas were masked out. This was achieved by applying snow masks extracted from the NASA MODIS snow cover product MOD10A2 (Riggs et al., 2006). To reduce noise and false classification in the MODIS snow map, only pixels identified as snow covered on at least 25% of the days of the MODIS composite time periods were labelled as *snow*. This meant that during the 8-day period, a pixel had to be detected as snow covered on at least two days, and during the 16-day period for at least four days in order to be labelled as *snow*. This approach minimised the number of wrongly classified MODIS snow pixels.
3. The snow-covered areas were then split into cold snow and warm snow areas by applying the resampled ERA-Interim temperature data. In theory, wet

snow occurs at temperatures above 0°C, while dry snow prevails at temperatures below 0°C. Since the composite periods spanned several days, the decision had to be made based on the average temperature over those days, which necessitated more conservative temperature thresholds. A lower temperature limit of 4°C for warm snow and an upper limit of -2°C for cold snow were found to be good compromises between clear distinction of warm and cold snow while still leaving enough non-masked pixels to produce meaningful histograms. Based on those thresholds, temperature masks for warm and cold snow were calculated and applied to the backscatter difference images, resulting in two separate images for cold and warm snow conditions for every time period. The cold snow pixels were expected to be dominated by dry snow and the warm snow pixels by wet snow.

4. The cold and warm snow backscatter difference images were averaged pixelwise over the entire melting period, so that a single averaged cold snow and a single averaged warm snow image remained.
5. Normalized histograms were calculated for the cold and warm snow difference images. No-data pixels were ignored in the histogram calculation. Overlaying the two histograms in the same plot allowed the extraction of the separating threshold, defined as the point where the two histogram peaks intersected.

The result of this process was a histogram plot with individual peaks for cold and warm snow that represented the entire study area. To investigate whether different land cover classes or elevations require different wet snow thresholds, the difference images for cold and warm snow were further subdivided by land cover and/or elevation before the histograms were calculated. The aggregated land cover classes *urban areas*, *agricultural areas*, *forests*, *scrubland*, *non-vegetated areas* and *glaciers* (see chapter 2.5) were differentiated. Subdivision by elevation was done by dividing the study area into 500-meter elevation bands based on a DEM. In total, four different levels of subdivision were used to calculate the histograms: 1) one single histogram plot over the entire study area (no subdivision); 2) subdivision by elevation; 3) subdivision by land cover; and 4) subdivision by both elevation and land cover.

3.4 Wet snow mapping

The wet snow mapping algorithm in itself was comparatively simple. Figure 10 shows the algorithm as a flow chart. The processing steps were as follows: A difference image γ_{diff} was produced for every available Sentinel composite period by subtracting the reference backscatter γ_{ref} from the investigated SAR composite backscatter γ_i (both backscatters were first transformed to the logarithmic dB domain):

$$\gamma_{diff} = \gamma_i - \gamma_{ref}$$

The wet snow cover area was calculated by applying the determined threshold to the difference images. If different thresholds were used for different land cover classes and/or elevations, the difference images were first subdivided into the corresponding fragments. The different thresholds were then applied to the individual fragments, before the resulting wet snow sub-images were joined back together.

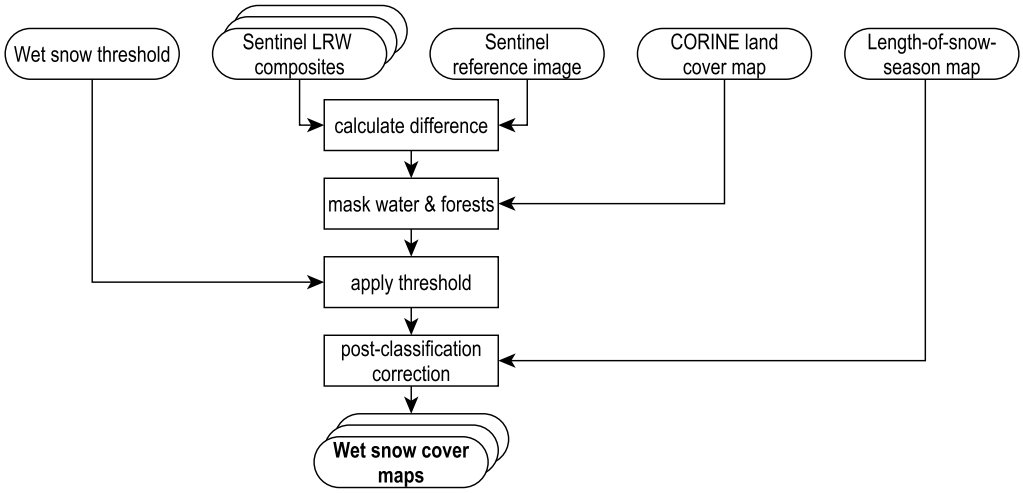

Figure 10. Flow chart of the wet snow mapping algorithm.

As the SAR data only allows the detection of wet snow, the main time period of interest was springtime. Wet snow map production was therefore limited to the months of February through August.

3.5 Post-classification correction

There were a multitude of error sources that could lead to misclassification of wet snow, e.g. noise in the reference or investigation image, more complex backscattering signatures in forests and urban areas, changes in soil moisture or surface roughness. Noise-induced misclassifications of wet snow typically appeared as very small, isolated patches consisting of only a few pixels. The majority of those small-scale errors could be removed by applying a patch filter to the classified wet snow map, removing any isolated snow patches that were smaller than 25 conjoined pixels. Other error sources led to larger misclassified areas that were not corrected by this approach. Given that snow is a highly seasonal phenomenon, these areas could partly be corrected by applying a Length Of Snow Season (LOSS) filter. If the mean duration of the snow season was known for a particular area, any pixels classified as *wet snow* within that area outside of the snow season could be corrected to *snow-free*.

A LOSS map was produced from the available 15-year time series of NASA MODIS snow maps. The data was split into 15 time series, each spanning one hydrological year (1st of October to 30th of September (USGS, 2016)). For each time series, the indexed date of the first and last occurrence of snow was extracted for each pixel, resulting in two 15-

element date index vectors per pixel. Outliers caused by misclassification or persistent cloud cover in the MODIS image were removed from each vector using the Thompson Tau method (Cimbala, 2011). Next, the mean and standard deviation of each vector was calculated. Finally, a separate map was produced for the first and the last occurrence of snow for a typical hydrological year by subtracting the standard deviation from the mean for the first occurrence of snow and adding the standard deviation to the mean for the last occurrence of snow. These two maps in combination defined the start and end date of a typical snow season for every pixel within the study area (see Figure 11).

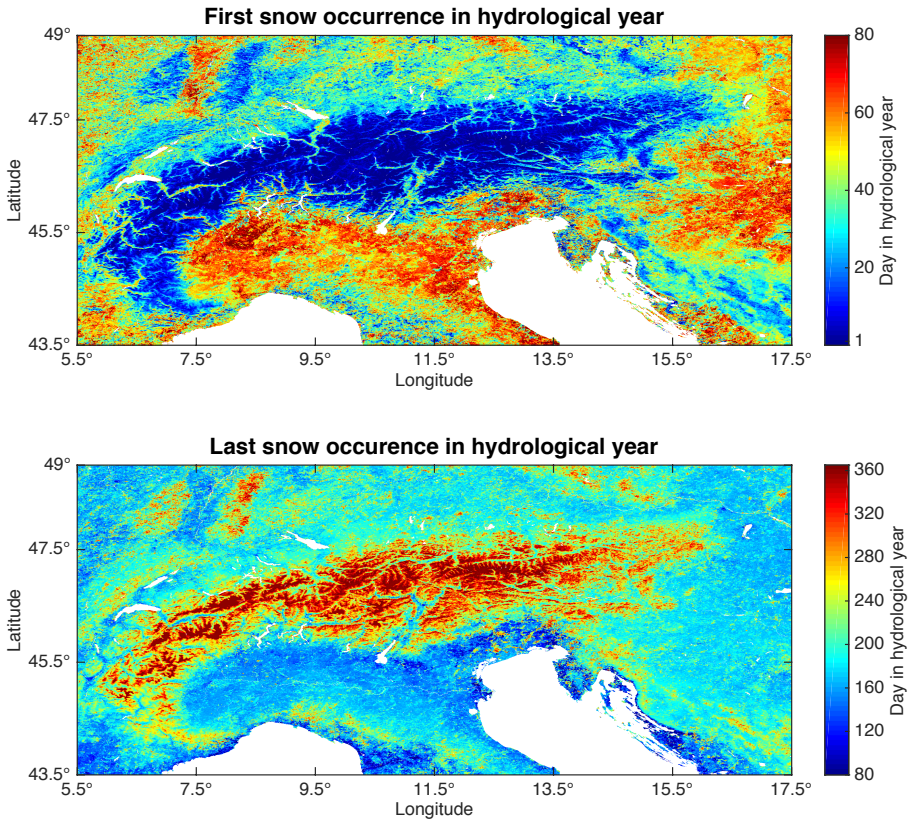

Figure 11. Maps of average first (top) and last (bottom) occurrence of snow.

3.6 Wet snow map validation

The Sentinel-derived wet snow maps were validated against MODIS-derived snow maps of the same time period. Two separate comparisons were made, one against the 500 m resolution NASA MODIS snow product and one against the 250 m EURAC MODIS snow product. For each image, a confusion matrix was produced. There are several measures that can be used to validate such classifications: overall accuracy, Kappa coefficient, error of commission, error of omission, user's accuracy and producer's accuracy. In this study, the area was classified into only two classes (wet snow and dry/no snow), and for the majority of the study period the dry/no snow class covered a substantially larger area than the wet snow class. This meant that even if a pixel was assigned to the dry/no snow class completely randomly, there was still a high chance that the assignment was

correct, leading to a high, but not very meaningful value for the overall accuracy. Cohen's kappa was therefore generally a more telling indicator for the actual quality of the classification, as it is corrected for chance agreement (Cohen, 1960). However, in the context of the present study, the kappa coefficient was not ideal because of the properties that were compared: the optically derived MODIS snow maps displayed the total snow cover area, without differentiating between wet and dry snow. As discussed in chapter 3, C-band radar sensors can only detect wet snow; therefore the SAR-derived snow maps only showed the wet parts of the total snow covered area, making a direct comparison more complicated. A high error of omission was expected in the early melting period, when large parts of the snow pack were still dry and therefore invisible to the radar. For this reason, the most descriptive measure for this study was the user's accuracy, which is the counterpart to the error of commission: it measured the percentage of correctly allocated wet snow pixels. The validation of the wet snow maps was therefore mostly based on the user's accuracy. The kappa coefficient was also considered, but only as a comparison tool: if of one algorithm setting produced generally higher kappa values than another, it was assumed that the corresponding settings produce more accurate wet snow maps. Due to the different nature of the compared quantities (i.e. wet snow cover vs. total snow cover), the absolute value of kappa could however not be directly translated into an absolute quality measure. As the total wet snow area decreases strongly during the melting season, the results were always viewed together with the total number of classified wet snow pixels.

The general performance of the Sentinel wet snow mapping algorithm was assessed by looking at the time series of those measures over the entire melting period. In addition, confusion images displaying agreement and disagreement between the Sentinel and the MODIS snow maps were produced, allowing a spatially more detailed investigation of the results. Data gaps and masked areas in the Sentinel composite image, and pixels that were cloud-covered in the MODIS image were excluded from the accuracy assessment.

4 Results

In this chapter, the relevant results of the wet snow mapping investigations are listed and described. The retrieved wet snow thresholds are described in sub-chapter 4.1. In sub-chapter 4.2, the results from the different adjustments to the standard wet snow mapping algorithm are described, compared against each other and finally merged to form the final wet snow mapping algorithm. The results from applying this final algorithm to current SAR composite data from 2015 and 2016 are described in sub-chapter 4.3.

4.1 Determination of wet snow thresholds from Histograms

The wet snow threshold was determined by comparing the histograms of backscatter difference from areas covered by cold and warm snow cover. Cold snow should be predominately dry; therefore the difference between the dry snow reference and the cold snow

backscatter should be close to zero dB, with only small variance. On the other hand, the reduced backscatter from warm and therefore mostly wet snow should lead to a negative backscatter difference and therefore to a histogram peak in the negative dB range. Ideally, the two histogram peaks would exhibit only very little overlap and allow the extraction of a clear separating threshold. A sufficient separability was given if both histogram peaks were unimodal, the apex of one histogram was outside of the other peak (i.e. if there was a valley between the two peaks) and if the warm snow peak featured generally lower backscatter difference values than the cold snow peak. If one of those conditions was not met, no threshold could be determined.

The histograms displayed over the next pages were all produced using the improved winter reference and VH-polarisation. While the shapes of the peaks were slightly different for the other three reference images and for VV-polarisation, the overall trends were the same for every case.

4.1.1 Single threshold for all land cover classes and elevations

In a first step, histograms were produced for warm and cold snow backscatter difference over all elevations and land cover classes (see Figure 12, bottom left plot). As expected, the cold snow backscatter difference produced a narrow histogram peak close to zero dB. However, the warm snow histogram showed a bimodal distribution covering a wide range of backscatter difference from -10 to +5 dB. This suggested that the warm snow backscatter was influenced by a multitude of effects and not just the reduced backscatter due to the higher dielectric losses in wet snow. A distinct extraction of a threshold was not possible from this plot.

4.1.2 Thresholds subdivided by elevation

In a second step, the snow pixels were split into 500 m elevation bands and individual histograms were produced for each band (see Figure 12, first and second row). This revealed a clear pattern: In lower elevations, the warm snow peaks lay clearly in the positive dB sector. This suggested that the reduced backscatter of wet snow was completely masked by some other effect that led to an increase in backscatter. No wet-snow threshold could therefore be extracted from those histograms. With increasing elevation, the warm snow histogram peak was shifting towards lower backscatter difference. Starting from 2000 m.a.s.l., the apex of the warm snow peak lay distinctly left of the cold snow peak and continued to shift towards lower backscatter difference with increasing elevation. Consequently, clear threshold detection was only feasible for elevations above 2000 m.a.s.l. The pixels were therefore additionally split into two zones, one for elevations below 2000 m.a.s.l. and one for elevations above 2000 m.a.s.l. (see Figure 12, bottom row). A threshold of -1.4 dB for VH-Polarisation and for the improved winter reference was extracted from the histogram for elevations above 2000 m.a.s.l. The thresholds for the other reference scenes and for VV-polarisation can be found in Table 7 in appendix A.3.

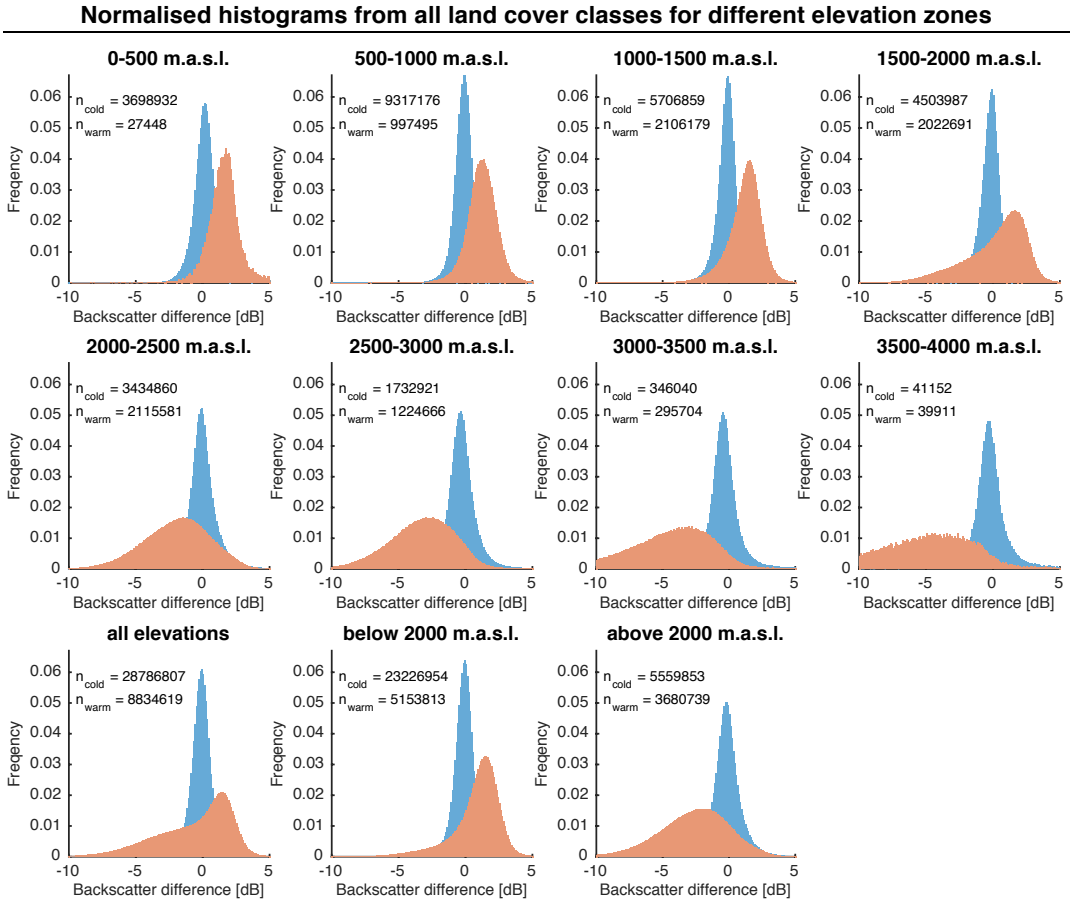

Figure 12. Normalised histograms of VH-backscatter difference from snow-covered pixels from all land cover classes and for different elevation zones. Red peak: *warm snow* pixels (T > +4°C). Blue peak: *cold snow* pixels (T < -1°C). Applied reference scene: improved winter reference.

4.1.3 Thresholds subdivided by land cover class

In a third step, the snow pixels were split into different land cover classes based on the CORINE land cover map. To reduce the influence of mixed pixels that typically occur at the border between two different land cover classes, a 3x3 pixel erode function was applied to the land cover map, thereby masking out the border zones. Individual histograms were then produced for each class (see Figure 13). This approach revealed that the majority of pixels contributing to the positive backscatter difference signal of warm snow observed at elevations below 2000 m.a.s.l. originated from the land cover classes *forest*, *urban areas* and *agricultural areas*. Incidentally, these were the predominant land cover classes for areas below 2000 m.a.s.l., while being barely present at elevations above 2000 m.a.s.l. (see Table 2). This could help to explain the shift of the warm snow peak from positive to negative backscatter difference with increasing elevation observed in Figure 12. The land cover classes found to allow a clear threshold extraction were *nonvegetated areas* and *glaciers*, which made up the majority of the land area above 2000 m.a.s.l. The extracted thresholds for the improved winter reference and VH-polarisation were -1.5 dB

for *non-vegetated areas* and -1.9 dB for *glaciers*. The thresholds for the other reference scenes and for VV-polarisation can be found in Table 6 in appendix A.3.

	Land cover portion below 2000 m.a.s.l.	Land cover portion above 2000 m.a.s.l.
Urban areas	6.3 %	0.0 %
Agricultural areas	43.8 %	0.1 %
Forest	40.2 %	4.5 %
Scrubland	8.2 %	33.1 %
Non-vegetated areas	1.2 %	56.1 %
Glaciers	0.0 %	6.1 %

Table 2. Share of the different land cover classes on the total study area below and above 2000 m.a.s.l., based on CORINE land cover classification.

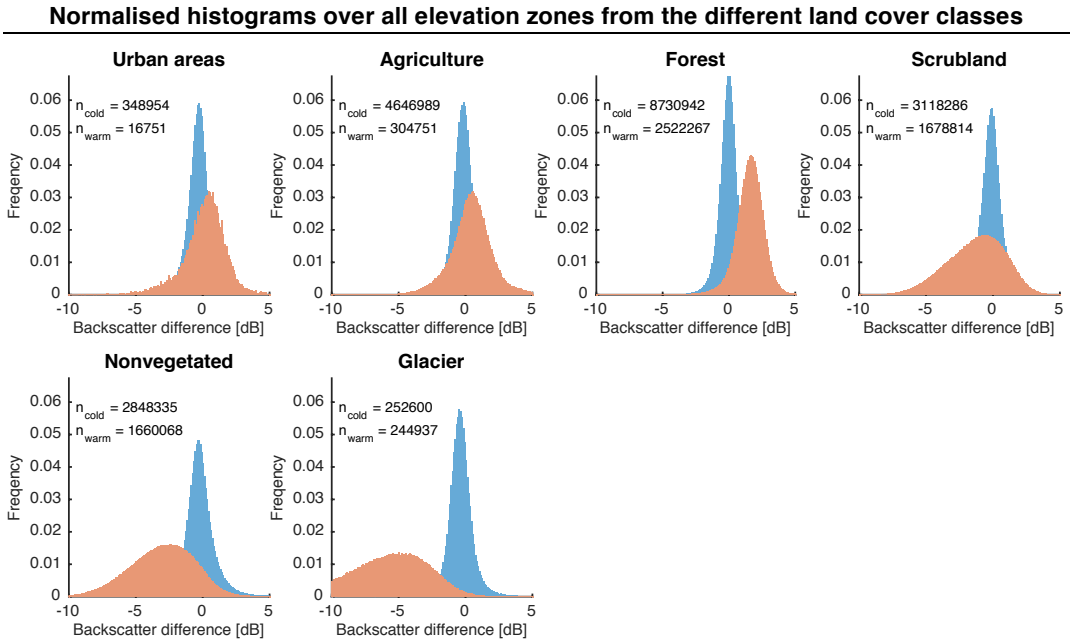

Figure 13. Normalised histograms of VH-backscatter difference from snow-covered pixels from the different land cover classes over all elevation zones. Red peak: *warm snow* pixels (T > +4°C). Blue peak: *cold snow* pixels (T < -1°C). Applied reference scene: improved winter reference.

4.1.4 Thresholds subdivided by elevation and land cover class

As a last step, snow pixels were subdivided by both elevation and land cover, so that individual histograms were produced for every 500 m elevation band within each land cover class. Figure 14 displays the histograms for *urban areas*, Figure 15 for *agricultural areas*, Figure 16 for *forested areas*, Figure 17 for *scrubland*, Figure 18 for *non-vegetated areas* and Figure 19 for *glaciers*. This further subdivision did not reveal any new information for the land cover classes *forest*, *urban areas* and *agriculture*, a threshold extraction was still not possible at any elevation. This problem was particularly dominant for *forested areas,* where the warm snow backscatter difference showed persistently higher values over all elevations than the cold snow (see Figure 16). The land cover classes *non-*

vegetated areas and *glaciers* showed clear separability for all elevations above 2000 m.a.s.l., with only small threshold differences between the different elevation bands. The most interesting land cover class for this approach was the class *scrubland*, as it was present on a wide elevation spectrum. It showed similar behaviour as the analysis over all land cover classes combined: at lower altitudes, the warm snow histogram peak featured higher backscatter difference values than the cold snow peak and lay well within the positive backscatter difference zone, thereby preventing a threshold extraction. With increasing elevation, the warm snow peak shifted towards lower backscatter difference values, until threshold extraction became possible above 2000 m.a.s.l. (see Figure 17). This suggested that there might be a general phenomenon that masked out any wet-snow induced backscatter reduction at lower elevations and instead led to an increase in backscatter difference. The most likely explanation was signal mixing due to the length of the composite period: as wet snow at lower elevations can occur and completely melt of within a few days or even hours, the LRW composite calculation could lead to a mixing of signals from wet snow and snow-free ground. The wet snow signal could therefore be lost in the process of calculating the weighted average of a pixel. This problem is discussed in more detail in chapter 5.4.2.

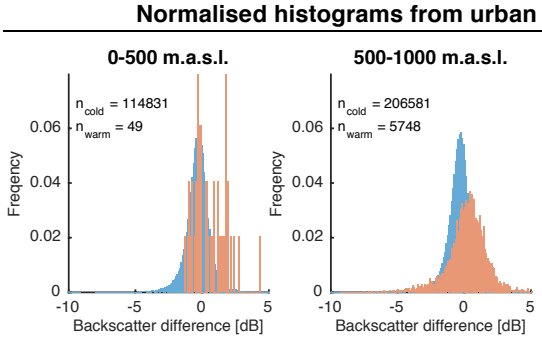

Figure 14. Normalised histograms of VH-backscatter difference from snow-covered pixels from land cover class *urban areas* for different elevation zones. Red peak: *warm snow* pixels (T > +4°C). Blue peak: *cold snow* pixels (T < -1°C). Applied reference scene: improved winter reference.

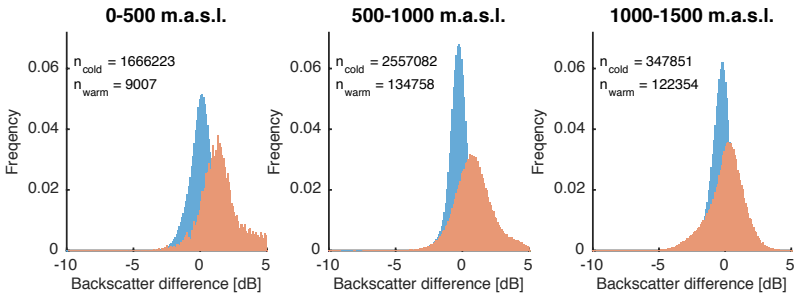

Figure 15. Normalised histograms of VH-backscatter difference from snow-covered pixels from land cover class *agricultural areas* for different elevation zones. Red peak: *warm snow* pixels (T > +4°C). Blue peak: *cold snow* pixels (T < -1°C). Applied reference scene: improved winter reference.

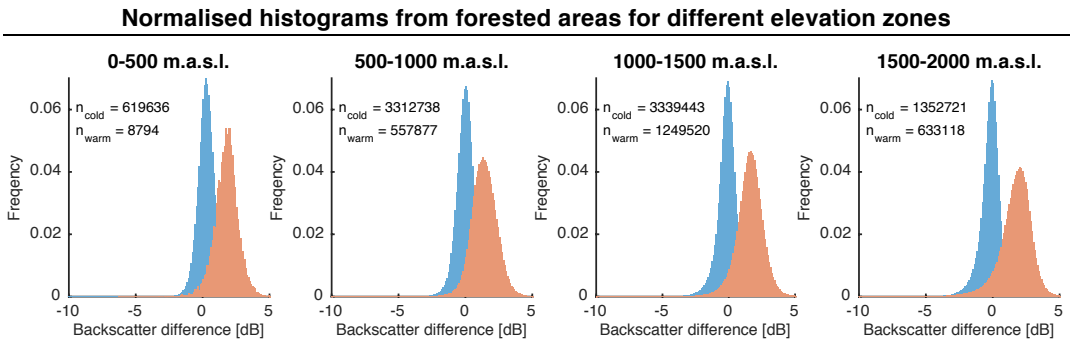

Figure 16. Normalised histograms of VH-backscatter difference from snow-covered pixels from land cover class *forest* for different elevation zones. Red peak: *warm snow* pixels (T > +4°C). Blue peak: *cold snow* pixels (T < -1°C). Applied reference scene: improved winter reference.

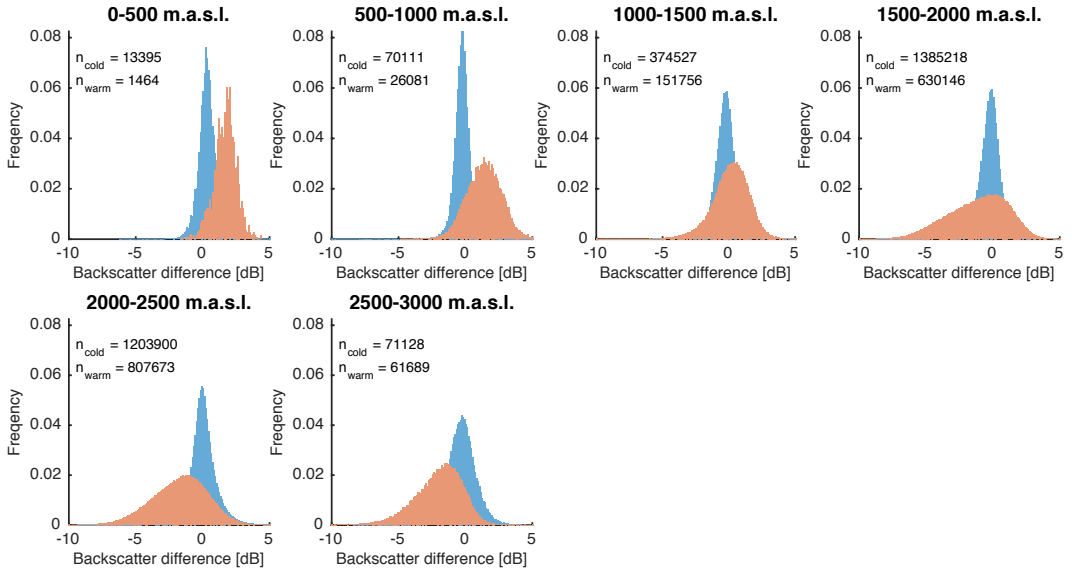

Figure 17. Normalised histograms of VH-backscatter difference from snow-covered pixels from land cover class *scrubland* for different elevation zones. Red peak: *warm snow* pixels (T > +4°C). Blue peak: *cold snow* pixels (T < -1°C). Applied reference scene: improved winter reference.

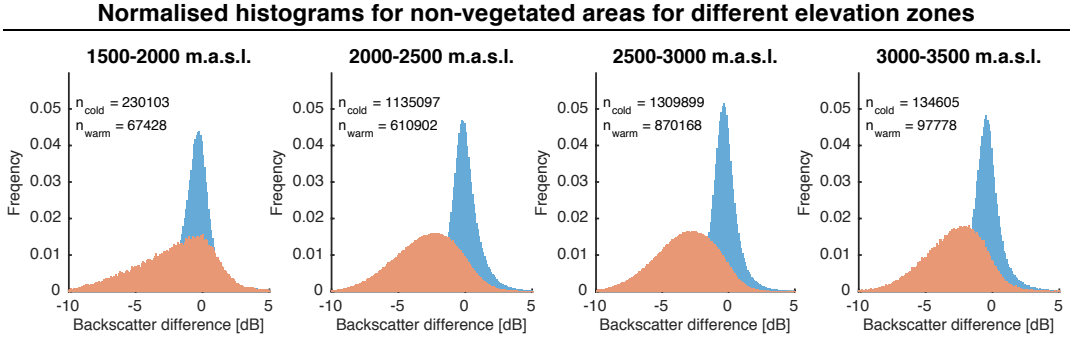

Figure 18. Normalised histograms of VH-backscatter difference from snow-covered pixels from land cover class *non-vegetated areas* for different elevation zones. Red peak: *warm snow* pixels (T > +4°C). Blue peak: *cold snow* pixels (T < -1°C). Applied reference scene: improved winter reference.

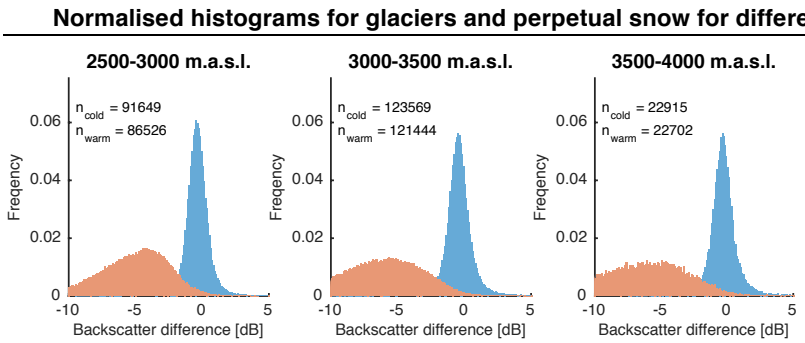

Figure 19. Normalised histograms of VH-backscatter difference from snow-covered pixels from land cover class *glaciers and perpetual snow* for different elevation zones. Red peak: *warm snow* pixels (T > +4°C). Blue peak: *cold snow* pixels (T < -1°C). Applied reference scene: improved winter reference.

The results described and shown here were derived from the difference image based on 16-day VH composites and the improved winter reference scene (see chapter 3.2.4). The wet snow thresholds for this configuration, as far as they were identifiable, are listed in Table 3. Similar analyses were carried out for the other three reference images as well as for VV-polarisations. The corresponding wet snow thresholds are listed in Table 6 in appendix A.3. While there were clear differences in the derived thresholds for the different polarisations and reference images, the main characteristics of the histograms did not derivate from those described here. That is, with one exception: when using the summer reference, the warm and cold snow peaks for land cover class *glacier* were both shifted towards higher backscatter difference, well into the positive dB zone (see Figure 20). This could be explained by the widespread wet snow contamination of the summer reference scene in those areas (see chapter 3.2.1), which led to decreased reference backscatter and therefore to increased backscatter difference for both warm and cold snow. While a separation of the peaks was still possible, the derived thresholds were atypically high, with values ranging between 0 and +5 dB.

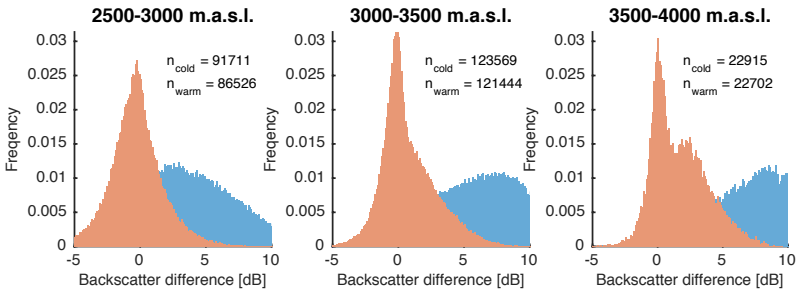

Figure 20. Normalised histograms of VH-backscatter difference from snow-covered pixels from land cover class *glaciers and perpetual snow* for different elevation zones. Red peak: *warm snow* pixels (T > +4°C). Blue peak: *cold snow* pixels (T < -1°C). Applied reference scene: simple summer reference.

	Urban areas	Agricultural areas	Forest	Scrubland	Non-vegetated areas	Glacier	All land cover classes
0-500 m.a.s.l.	-	-	-	-	-	-	-
500-1000 m.a.s.l.	-	-	-	-	-	-	-
1000-1500 m.a.s.l.	-	-	-	-	-	-	-
1500-2000 m.a.s.l.	-	-	-	-	-	-	-
2000-2500 m.a.s.l.	-	-	-	-1.0 dB	-1.3 dB	-	-1.2 dB
2500-3000 m.a.s.l.	-	-	-	-1.3 dB	-1.5 dB	-1.8 dB	-1.5 dB
3000-3500 m.a.s.l.	-	-	-	-	-1.5 dB	-2.0 dB	-1.7 dB
3500-4000 m.a.s.l.	-	-	-	-	-	-2.0 dB	-1.7 dB
All elevations	-	-	-	-	-1.5 dB	-1.9 dB	-
Below 2000 m.a.s.l.	-	-	-	-	-	-	-
Above 2000 m.a.s.l.	-	-	-	-1.0 dB	-1.5 dB	-1.9 dB	-1.4 dB

Table 3. Wet snow thresholds for 16-day VH composites, based on the improved winter reference scene.

4.1.5 Threshold application

Table 3 lists the different wet snow thresholds, as far as they could be determined. For certain land cover classes and elevations, definition of a clear threshold was not possible. This was either because the corresponding land cover class or elevation zone experienced some backscatter effect that masked out the decreasing backscatter of wet snow, or because the number of pixels for that class was too small to produce a meaningful histogram. In the wet snow mapping algorithm, areas where no individual threshold could be derived were therefore handled according to the following three rules:

1. If no clear threshold could be determined over all elevations for a certain land cover class, the threshold extracted from areas above 2000 m.a.s.l. within that land cover class was applied to all elevations.
2. When individual thresholds per elevation band were applied, the threshold for the lowest separable elevation band was applied to all elevations below it and the threshold for the highest separable elevation band was applied to all elevations above it.
3. If a certain land cover class did not allow the extraction of a threshold for any elevation, the threshold determined over all land cover classes for areas above 2000 m.a.s.l. was applied to all elevations of that land cover class.

4.2 Refinement of the wet snow mapping algorithm

Several adjustments and extensions to the standard wet snow mapping algorithm based on thresholding were introduced and tested against each other in the present study. The results from those comparisons are described in this sub-chapter. The following refinements were implemented:

1. Masking of forested areas due to interference of canopy backscatter effects on the wet snow backscatter.
2. Application of a Length-Of-Snow-Season (LOSS) filter to correct misclassifications due to backscatter-reducing effects that occur in snow-free areas during warmer periods.
3. Application of individual wet snow thresholds for different land cover classes and/or elevation zones to account for land cover induced backscatter differences.
4. Comparison of different approaches of reference image production to find the most suitable method.
5. Comparison of different combinations of the two polarisations in order to exploit the full information content of every SAR acquisition.
6. Comparison of different temporal baselines of the LRW composites to find the best compromise between spatial completeness and temporal resolution.
7. Comparison of different MODIS validation data in order to assess the influence of spatial resolution of the validation images on the achieved accuracies.

Since those refinements partly build on the results of previous adjustments, some deductions are already described in this chapter. A more in-depth discussion of the results can be found in chapter 5.

4.2.1 Masking of forested areas

The investigation of histograms subdivided by land cover (see chapters 4.1.3 and 4.1.4) revealed that the backscatter difference of warm snow pixels that were forest-covered was consistently higher than that of forest-covered cold-snow pixels, thereby preventing wet snow detection by means of thresholding. This effect was most likely due to the scattering properties of forest: in densely forested areas, the backscatter signal was dominated by volume scattering in the crown, where usually only little snow is found. Due to the oblique angle of incident radar rays, only a very small part of the signal could reach and be scattered by the snow-covered forest floor. Wet snow mapping in densely forested areas therefore appeared to be infeasible. This finding is in agreement with several studies (e.g. Baghdadi et al., 1997; Rees & Steel, 2001), which noted that snow mapping in densely forested areas with the standard approach is impossible. Some efforts have been made in the past to overcome this limitation by incorporating forest canopy models (e.g. Cohen et al., 2015). Such investigations were beyond the scope of this study; therefore forested areas were masked out in all further analyses.

4.2.2 Assessment of the length-of-snow-season correction

Aside from snow wetness, other changes of the land surface such as soil moisture, vegetation changes or standing water can also lead to a decrease of radar backscatter. Such influences could lead to misclassification of wet snow. To illustrate this issue, an exemplary wet snow map was calculated based on a 16-day VH-polarised image, composited from images acquired between the 9th and the 24th of May 2015, and using the snow-corrected

summer reference image. The resulting wet snow map was then compared to the MODIS snow map of the same date to produce a confusion image, where pixels were marked as *correctly classified as wet snow, correctly classified as dry/no snow, wet snow error of omission* and *wet snow error of commission.* Masked-out pixels and areas where cloud cover obscured the MODIS-image were marked separately. Figure 21 displays the resulting confusion images. The top image shows the confusion map before the application of the Length-Of-Snow-Season (LOSS) correction. Aside from the correctly detected wet snow cover along the Alps, large regions in the Po Valley as well as in low altitude areas in the north and the northeast of the study area were initially erroneously classified as wet snow (red pixels), leading to an increased error of commission. A comparison with the ERA-Interim temperature maps of the same period revealed that the temperatures in those areas during the acquisition period were well above snowmelt level; therefore it was safe to assume that those areas were in fact snow-free and that those wet snow pixels were misclassified. The LOSS-filter (see chapter 3.5) effectively removed most of those misclassified pixels, producing a much more plausible map (see Figure 21, bottom). Some misclassification remained around the Adriatic Sea, which was most likely due to misclassification in the original NASA MODIS snow cover product that the LOSS-filter was based on. Overall, the LOSS-filter seemed to function as an effective correction device.

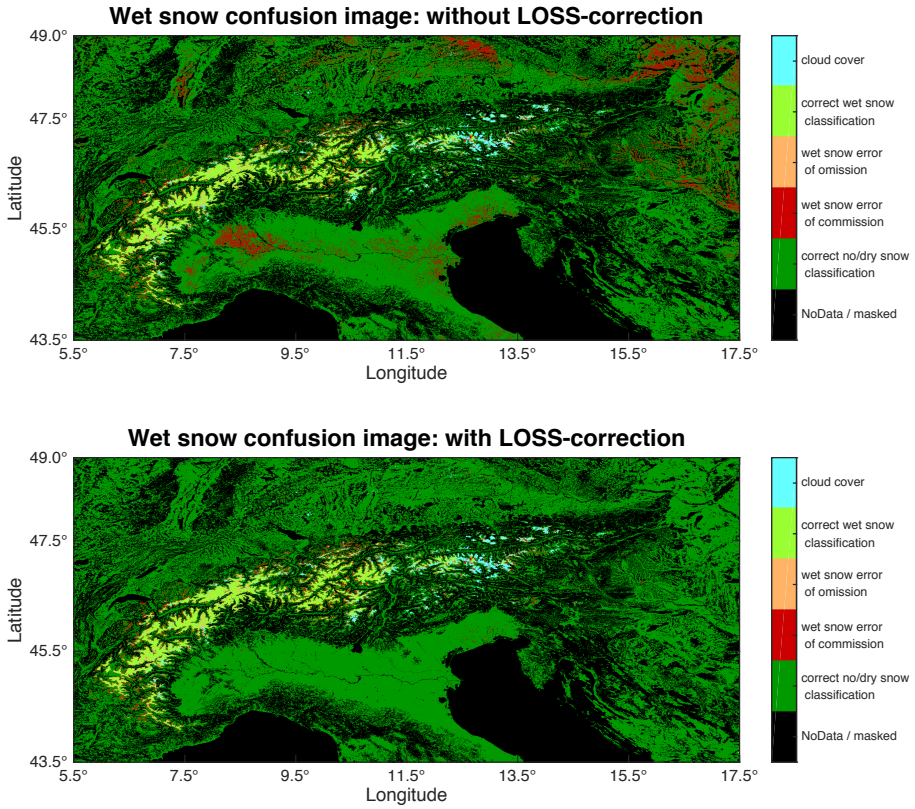

Figure 21. Exemplary comparison of the confusion images of a wet snow map before (top) and after (bottom) applying the length-of-snow-season correction.

For a more meaningful evaluation of the LOSS-correction performance, a set of wet snow maps was produced for each reference image and polarisation, covering the entire melting period of 2015. Each map was compared against the corresponding NASA MODIS snow map before and after the LOSS-correction. User's accuracy, error of omission, kappa coefficients and total number of wet snow pixels were extracted from the results. Figure 22 displays the results for wet snow maps derived from VH-polarisation and from the snow-adjusted summer reference. The user's accuracy was significantly increased over the entire time series by applying the LOSS-correction, reaching an improvement of up to 48% compared to the non-corrected maps. Since this correction only removed wet snow pixels, an improvement in the error of omission was not possible, leading to the same values before and after the LOSS-correction. The total number of wet snow pixels was reduced by up to 4.8 million.

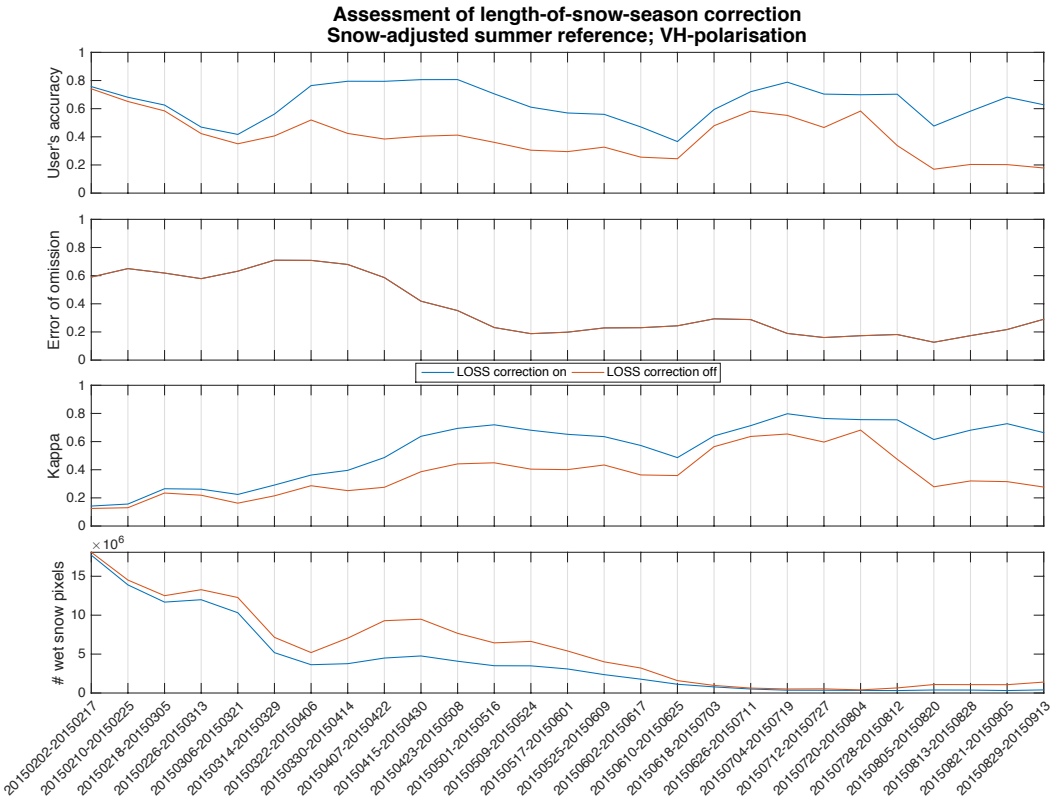

Figure 22. Comparison of user's accuracy, error of omission and number of classified wet snow pixels of snow maps produced from VH-polarised 16-day composites and from the snow-adjusted summer reference before and after application of the LOSS-filter.

The magnitude of the improvement in user's accuracy achieved by the LOSS-correction varied, depending on the reference scene and polarisation used for the generation of the wet snow maps. However, every case showed a clear improvement after application of the LOSS-filter (see Table 4). The correction was therefore applied to every map produced in the further analyses.

	Summer ref.		Winter ref.		Snow-adj. summer ref.		Improved winter ref.	
	VH	**VV**	**VH**	**VV**	**VH**	**VV**	**VH**	**VV**
Min. increase in UA	3.3%	3.3%	6.2%	9.4%	6.7%	6.1%	3.0%	8.1%
Max. increase in UA	40.3%	33.3%	32.6%	40.6%	**48.0%**	33.6%	20.8%	46.2%

Table 4. Minimal and maximal increase in user's accuracy (UA) of snow maps produced for the melting season of 2015 after applying the LOSS-correction for the different reference scenes and polarisations.

4.2.3 Comparison of different threshold subdivisions

Four different subdivisions of the wet snow threshold were compared against each other: 1) one single threshold applied to all land areas within the study area; 2) individual thresholds per land cover class, as far as they could be determined; 3) individual thresholds per 500 m elevation band, as far as they could be determined; and 4) individual thresholds per 500 m elevation band within each land cover class (see chapters 3.3 and 4.1). The expectation was that subdivided thresholds would produce more accurate wet snow maps, as they could better account for backscatter differences between different land cover classes and/or elevations. However, a comparison of the accuracy measures for the wet snow maps produced with the different threshold subdivisions revealed almost no variations. Figure 23 shows the measures for the maps based on VH-polarised images and the improved winter reference. The overall trend was very similar for maps derived from VV-polarised images and from the snow-corrected summer reference and the simple winter reference.

In general, the subdivision of the wet snow threshold barely influenced the accuracy of the resulting wet snow map. Subdivision by land cover led to a very slight improvement in user's accuracy and error of omission in the very early melting season, but the changes were not significant enough to justify the higher computational and manual effort associated with the production of those subdivided snow maps. In the later part of the melting season, the subdivisions even seemed to produce slightly lower accuracies compared to the non-divided threshold, but these changes were again very small. The comparison of kappa values showed very little differences as well and therefore confirmed those findings.

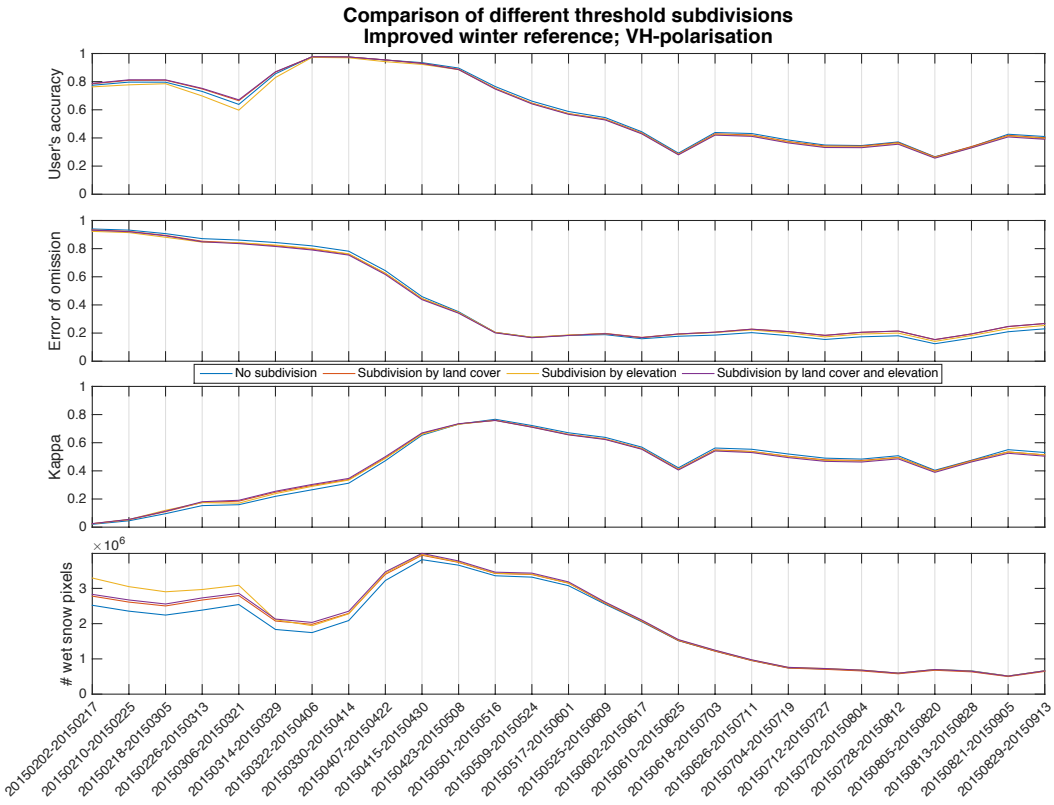

Figure 23. Comparison of user's accuracy, error of omission and number of classified wet snow pixels of snow maps produced from VH-polarised 16-day composites and from the improved winter reference for different subdivisions of the wet snow threshold.

There was one exception to this trend. Snow maps produced with the simple summer reference image showed higher sensitivity to the threshold subdivision in the second half of the melting season (see Figure 24). Starting in May, the accuracies of the wet snow maps produced with a single threshold began to fall, dropping below 20% in July and August. With the number of classified wet snow pixels reaching almost zero, the error of omission increased up to 99.8%, making the resulting wet snow maps completely unusable. This problem was likely caused by wet snow contamination of the summer reference image in high altitude areas (see chapter 3.2.1). During summer months, the only areas still featuring wet snow were largely identical with the areas where the summer reference contained wet snow contamination. This led to an increase in omission of wet snow as the time series progressed towards summer. These effects could already be observed in the histograms (see Figure 20), where both warm and cold snow peaks were suddenly shifted towards higher backscatter difference with increasing elevation. As can be seen in Figure 24, using individual and much higher thresholds of up to +5 dB for those areas could partly correct this effect. Best results were achieved when thresholds were set individually per land cover class. An increase in user's accuracy of up to 56.6% could be achieved. Further subdivision by elevation did not bring significant further improvement.

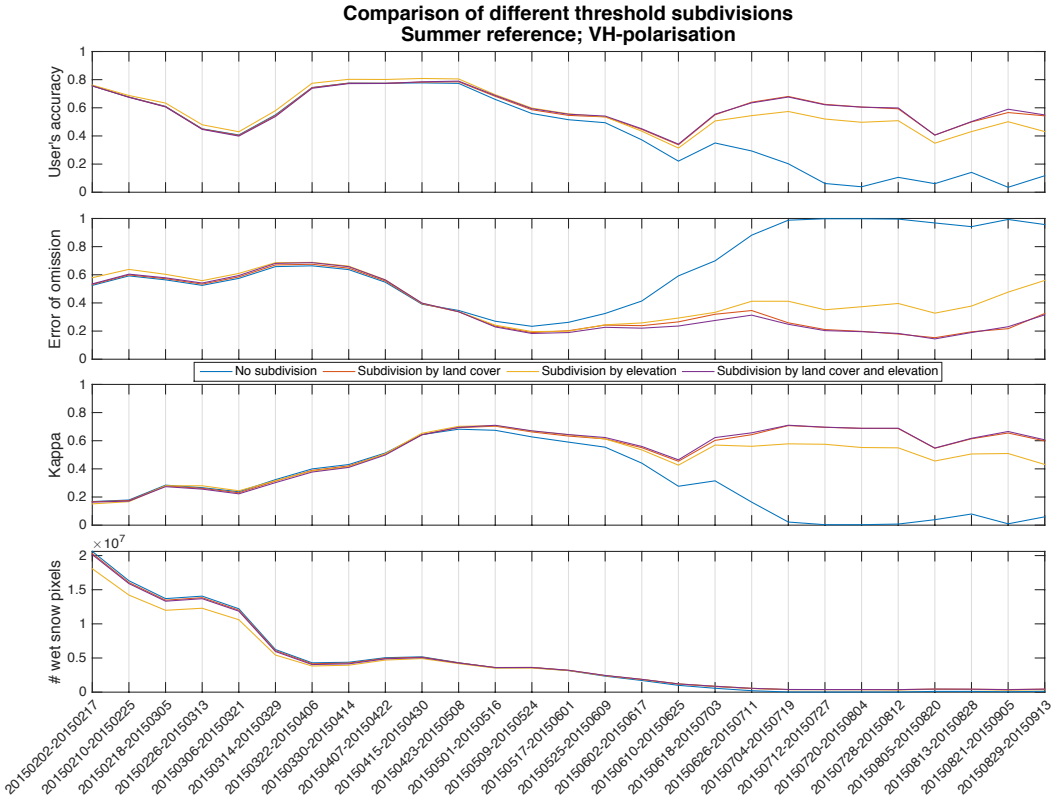

Figure 24. Comparison of user's accuracy, error of omission and number of classified wet snow pixels of snow maps produced from VH-polarised 16-day composites and from the summer reference for different subdivisions of the wet snow threshold.

Based on those findings, a single threshold was applied for wet snow maps derived from the simple winter, improved winter and snow-adjusted summer reference in all further analyses. For maps derived from the simple summer reference, individualised thresholds for each land cover class were used.

4.2.4 Comparison of different reference images

A direct comparison of wet snow map accuracies achieved by applying the four different reference images was carried out. Based on the findings of chapter 4.2.3, a single threshold for the entire scene was used for the two winter reference images and the snow-adjusted summer reference image. Individual thresholds per land cover class were used for the simple summer reference. Figure 25 and Figure 26 show the wet snow accuracy measures over the entire melting period for VH and VV polarisations. All time series show similar overall trends: After lower levels in early snowmelt season, the user's accuracy increased for April images, reaching up to 98% for the improved winter image in VH-polarisation and 95% in VV-polarisation. User's accuracy for both VH- and VV-polarisation then start to fall again, reaching a minimum for the composite spanning from the 10th to the 25th of June. After that, user's accuracies start to increase again. The error of omission largely behaved as expected: Widespread dry snow cover in early snowmelt season led to a high error of omission. In April and May, increased snow melting trans-

formed the majority of snow cover into wet snow, making it detectable by radar and therefore reducing the error of omission. In the later months, the residual snow cover was mostly wet and therefore detectable with a relatively low error of omission. The kappa coefficient behaved inverse to the error of omission: after very low values in the beginning of February, it began to gradually increase until reaching a maximum of 0.77 for VH and 0.70 for VV by the end of April. After that, the behaviour of the kappa coefficient largely mirrored the user's accuracy.

In VH-polarisation, the improved winter reference produced the most accurate wet snow maps in terms of user's accuracy in the first half of the investigation period. Starting at the end of May, the snow-adjusted summer reference surpassed the improved winter reference in terms of user's accuracy and produced consistently more accurate wet snow maps during summer months (see Figure 25). The simple summer and winter references showed similar trends, but at a consistently lower level of user's accuracy than their improved versions. This confirmed that the adjusted methods applied to generate the improved winter and snow-adjusted summer reference (see chapter 3.2) did in fact present an improvement over the simpler approaches.

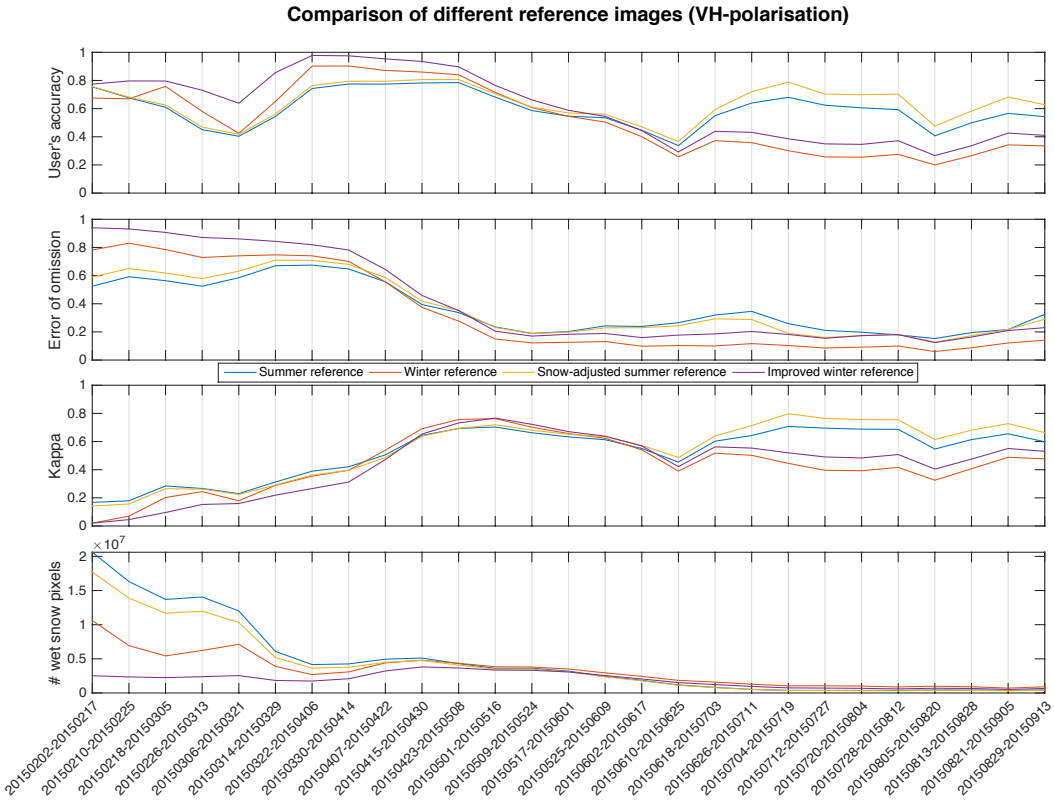

Figure 25. Comparison of user's accuracy, error of omission and number of classified wet snow pixels of snow maps produced from VH-polarised 16-day composites for different reference images.

The overall trends and achieved user's accuracies were similar for VH- and VV-polarisations. However, in VV-polarisation, wet snow mapping with the snow-adjusted summer reference outperformed mapping with the improved winter reference in terms of

user's accuracy over the entire melting season. The accuracy differences between the results for the four reference images were largest in June, July and August. While the user's accuracies were similar for VH- and VV- polarisations, the error of omission was significantly higher in VV-polarisation from May onwards (see Figure 26).

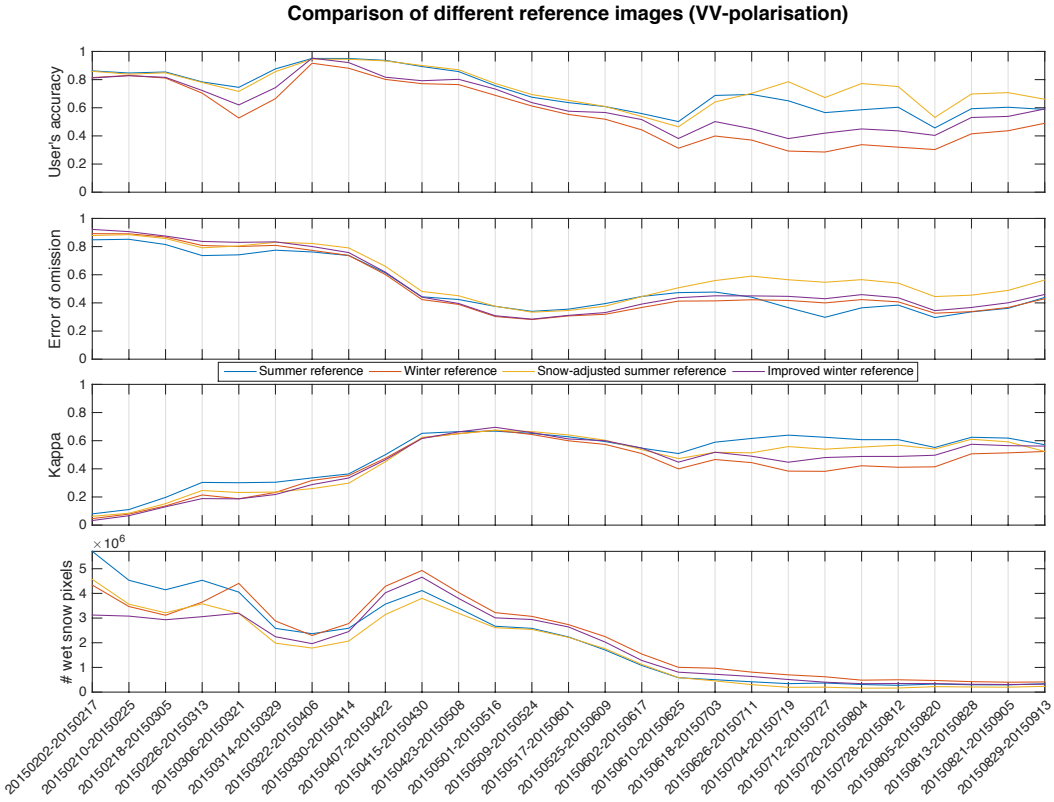

Figure 26. Comparison of user's accuracy, error of omission and number of classified wet snow pixels of snow maps produced from VV-polarised 16-day composites for different reference images.

All four reference versions displayed a gradual decrease in user's accuracies between the end of April and the beginning of June. This period corresponded with a relatively high percentage of cloud-coverage present in the MODIS image. Consistent cloud cover obscured up to 22% of detected wet snow pixels (see Figure 27, red line). While cloud coverage does not influence the radar-retrieved wet snow map, it does impair the MODIS snow image, leading to lower agreement when the two datasets were compared. Additionally, a clear drop in Sentinel data coverage could be observed in the beginning of June, reaching only 82% on the composite from the 10th to the 25th of June (see Figure 27, blue line). This drop in completeness, together with the high percentage of cloud obscured wet snow pixels, could help explain the distinct notch in user's accuracy and kappa for the corresponding composite period (see Figure 25 and Figure 26). The decrease in accuracy was therefore interpreted as an artefact of the validation process and not necessarily as evidence of actual malfunction of the wet snow mapping algorithm.

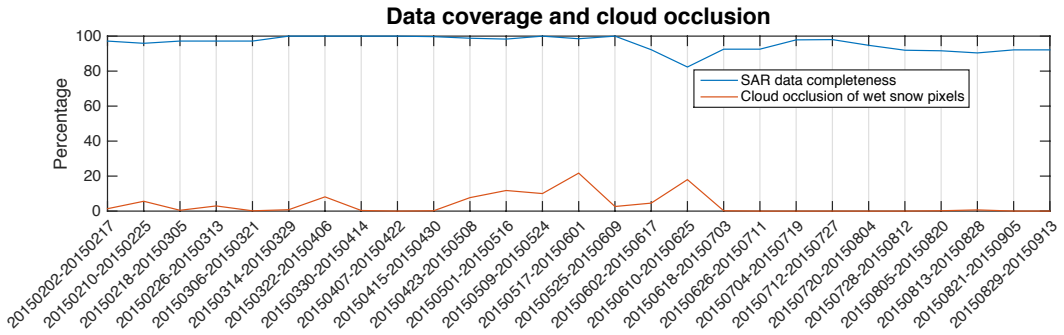

Figure 27. Data completeness of the 16-day SAR composites and cloud occlusion of wet snow pixels over the melting period of 2015.

The results presented in this sub-chapter demonstrated that the snow-adjusted summer reference produced consistently more accurate wet snow maps than the simple summer reference and that the improved winter reference produced consistently more accurate maps than the simple winter reference. As a consequence, the simple summer and winter reference images were not used for any further analyses. Between the improved winter reference and the snow-adjusted summer reference, no clear favourite could be determined. The improved winter reference seemed to outperform the snow-adjusted summer reference in the first half of the melting period, while the snow-adjusted summer reference produced more accurate wet snow maps during the second half of the investigation period, with the changeover being located in mid-May. Based on those findings, all further analyses were performed with both improved reference scenes.

4.2.5 Combination of VH- and VV-polarisations

So far, wet snow maps have been extracted separately from VH- and VV-polarised images. To exploit the full information content of the polarised data, a combination of the two polarisations was desirable. A weighted average of the backscatter differences D_{VH} and D_{VV} was calculated:

$$D_{comb} = W * D_{VH} + (1 - W) * D_{VV}.$$

Six different values for the weight W were compared: W = 0 (which makes D_{comb} equivalent to D_{VV}), W = 0.2, W = 0.4, W = 0.6, W = 0.8, and W = 1 (which makes D_{comb} equivalent to D_{VH}). For each weight, separate histograms for cold and warm conditions were produced and individual thresholds per weight were extracted. These thresholds were then applied to the weighted backscatter difference images to produce wet snow maps. The resulting accuracies over the melting period are plotted in Figure 28 (for the improved winter reference) and Figure 29 (for the snow-adjusted summer reference).

When applying the improved winter reference, pure VH-polarisation produced highest user's accuracies and kappa in the first part of the melting period, but around mid-May it was surpassed by the pure VV-polarisations as well as by the different combinations (see Figure 28). The weights W = 0.4 and W = 0.6 produced the highest mean values over the

entire snowmelt season in terms of user's accuracy (65.5%) resp. kappa (47.5%) (see Table 5).

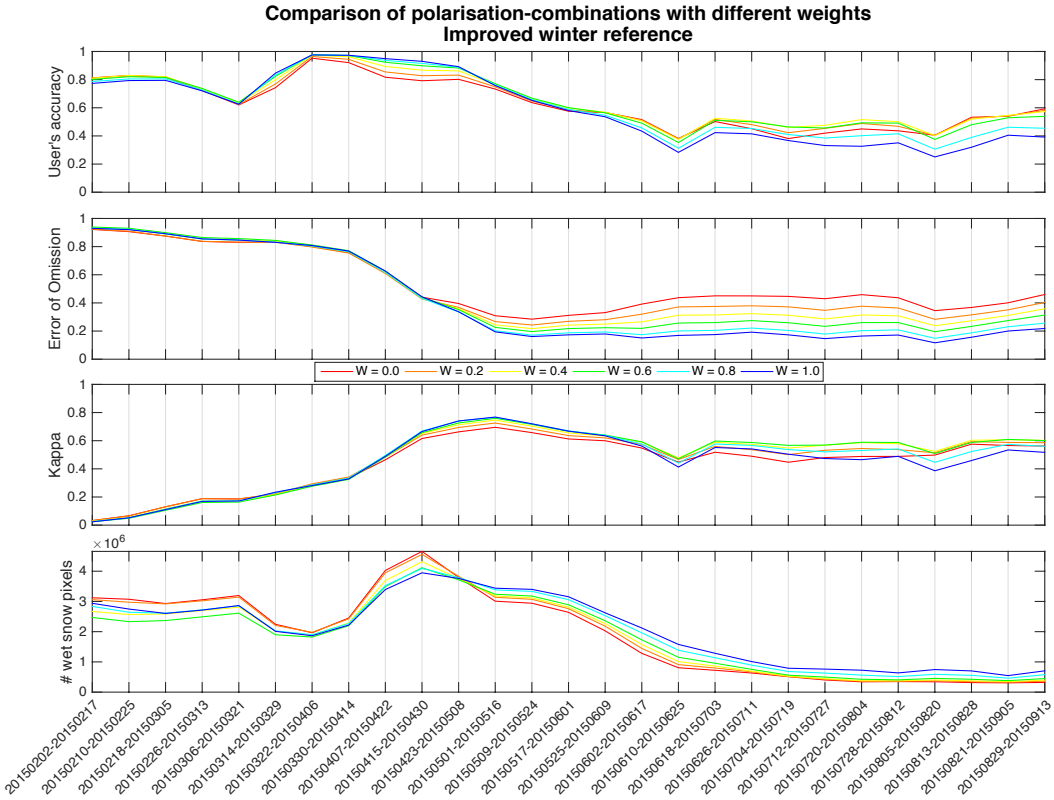

Figure 28. Comparison of combinations of VH- and VV-polarisations for the improved winter reference, using different weights for the VH-polarisation (W = 0 is equivalent to VV-polarisation; W = 1 is equivalent to VH-polarisation).

When using the snow-adjusted summer reference, the VV-polarisation achieved higher user's accuracies than the VH-polarisation for most of the melting period. However, it also produced consistently higher errors of omission, which led to lower kappa coefficients (see Figure 29). The weight W = 0 achieved the highest mean user's accuracy of 73.8% over the snowmelt season, but in terms of kappa the weight of W = 0.8 appeared to be best, producing a mean kappa value of 55.0% (see Table 5). When considering both user's accuracy and kappa, a value somewhere between these two weights would achieve the best compromise.

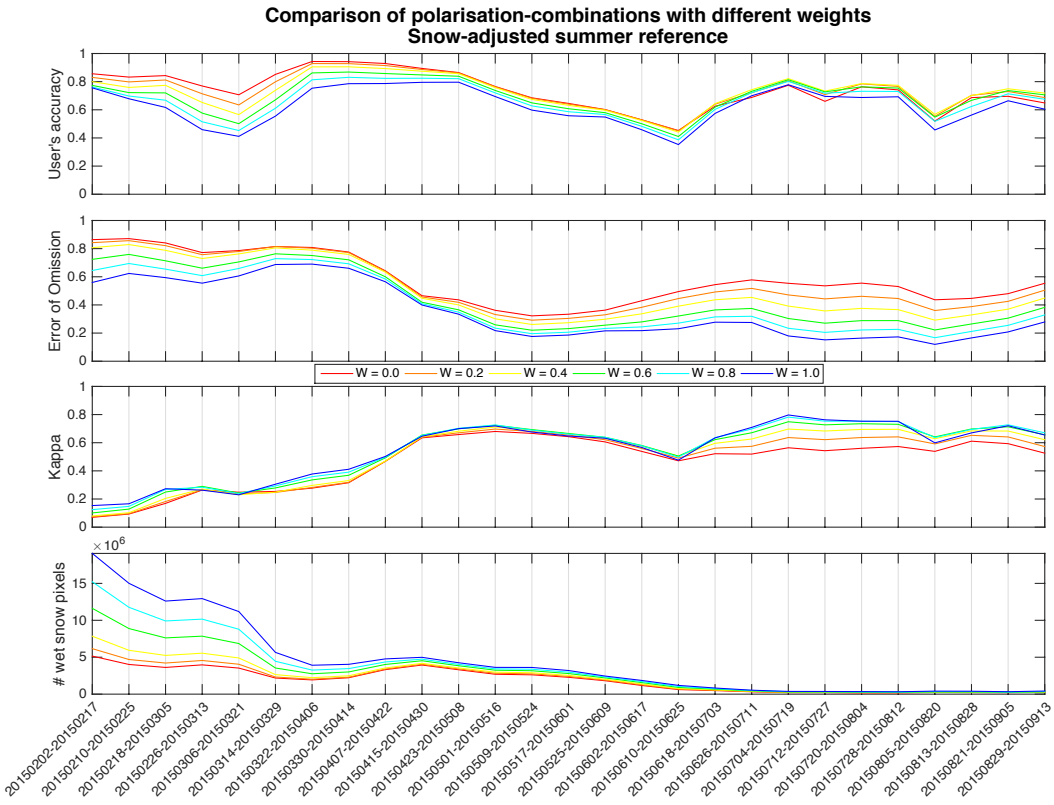

Figure 29. Comparison of combinations of VH- and VV-polarisations for the snow-adjusted summer reference, using different weights for the VH-polarisation (W = 0 is equivalent to VV-polarisation; W = 1 is equivalent to VH-polarisation).

		W=0.0	W=0.2	W=0.4	W=0.6	W=0.8	W=1.0
Improved winter reference	mean UA	62.8%	64.2%	**65.5%**	65.1%	62.0%	59.6%
	mean kappa	43.9%	46.2%	**47.5%**	**47.5%**	46.2%	44.3%
Snow-adjusted summer reference	mean UA	**73.8%**	73.6%	72.5%	69.6%	66.8%	63.0%
	mean kappa	46.7%	49.3%	51.6%	54.0%	**55.0%**	54.8%

Table 5. Mean values for user's accuracy (UA) and kappa coefficient over the entire snowmelt season for the different reference scenes and different values for the weight W.

When the values for both accuracy measures achieved with both reference images were considered together, a weight of W = 0.4 proved to be the best compromise over the entire time series. All further analyses were therefore carried out with a weighted average of VH and VV backscatter differences, where the VH-polarisation was weighted with 0.4 and VV-polarisation with 0.6. The corresponding wet snow thresholds were -1.1 dB when applying the improved winter reference and -2.3 dB when applying the snow-adjusted summer reference.

4.2.6 Comparison of 16-day and 8-day composites

The length of the temporal baseline for the composite images is the result of a trade-off between temporal resolution and image completeness. As the focus in this study was on high percentage of data coverage, a relatively long composite period of 16 days was chosen (see chapter 2.2). During the melting season, the extent of snow cover can change heavily within only a few days, which can lead to a mixing of snow- and ground-backscatter over 16 days. It was expected that this mixing impaired the overall accuracies of wet snow maps achievable with 16-day composites. In theory, a shorter composite period should reduce the mixing of different backscatter signals and therefore improve the accuracies of retrieved wet snow maps.

To test this theory, wet snow maps were produced based on 8-day composite images and their accuracies were compared to the accuracies achieved with the 16-day composites. Figure 30 displays the results for the improved winter reference. The snow-adjusted summer reference produced slightly different absolute values, but the overall trends were the same. The 8-day composite wet snow maps showed more fluctuations in accuracies, but viewed over the entire melting period the achieved values in user's accuracy were similar for 8-day and 16-day composites. The 8-day composite maps displayed generally higher values in error of omission for both reference images, leading to generally lower kappa values.

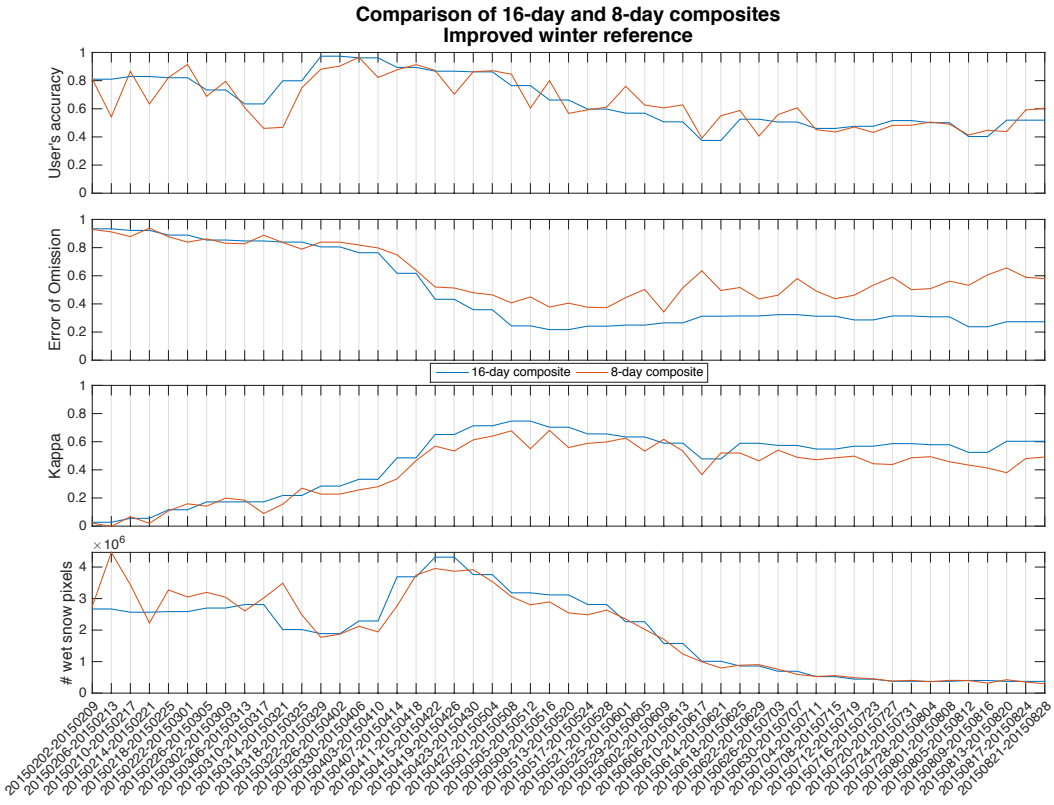

Figure 30. Comparison of wet snow accuracies achieved by 16-day and 8-day composites and the improved winter reference.

The expected increase in accuracy for 8-day composites could not be observed. The reason for this was most likely the lack of enough data to produce 8-day composite images with sufficient quality. The 8-day radar composite images suffered from large data gaps, with data coverage during the melting period varying between 64% and 99% (see chapter 2.2). Where data was available, the spatial overlap between the different SAR acquisitions was smaller than for 16-day composites, which impaired the noise-reduction capabilities of the LRW-algorithm and therefore led to more noisy images. The combination of data gaps and higher noise level most likely offset any improvement in accuracy achieved due to decreased signal mixing. A definitive assessment of the relationship between length of temporal baseline and quality of wet snow mapping was therefore not possible due to the lack of sufficient data. Consequently, only 16-day composite data was used for all further analyses in this study.

4.2.7 Validation with the EURAC MODIS snow product

So far, the wet snow maps produced in this study were validated against the MODIS 500m resolution snow product available from NASA (Riggs et al., 2006). The main advantages of this product were its high overall accuracy of up to 99% (Hall & Riggs, 2007) and the large spatial coverage of a single image tile. Its main disadvantage was the 500m spatial resolution, which was roughly five times coarser than the LRW composite resolution. Any comparison between the two data sets will therefore suffer from an inherent inaccuracy due to the resolution differences. To assess the magnitude of this problem, the wet snow maps were additionally validated against the 250m resolution EURAC MODIS snow product (Notaricola et al., 2013b). This product was based on the same input data as the NASA product, but exploited the higher spatial resolution of MODIS bands 1 & 2 to produce snow maps with 250m resolution (see chapter 2.3.2). The expectation was that a comparison with a higher resolution validation image would lead to higher agreement between Sentinel- and MODIS-derived snow maps.

The comparison was conducted for wet snow maps derived from the improved winter reference and the snow-adjusted summer reference. Figure 31 shows the results for the improved winter reference; the results for the snow-adjusted summer reference displayed the same overall trends and are therefore not printed here. The results demonstrated a higher user's accuracy for the EURAC product for the majority of the melting season. However, the error of omission was also generally higher for the EURAC product, particularly during the summer months. As a consequence, the overall map agreement, measured by the kappa coefficient, was very similar for both MODIS products during the first half of the melting season, but was significantly lower for the EURAC product during summer months. The usage of the EURAC product could therefore not be seen as an improvement to the wet snow map validation process.

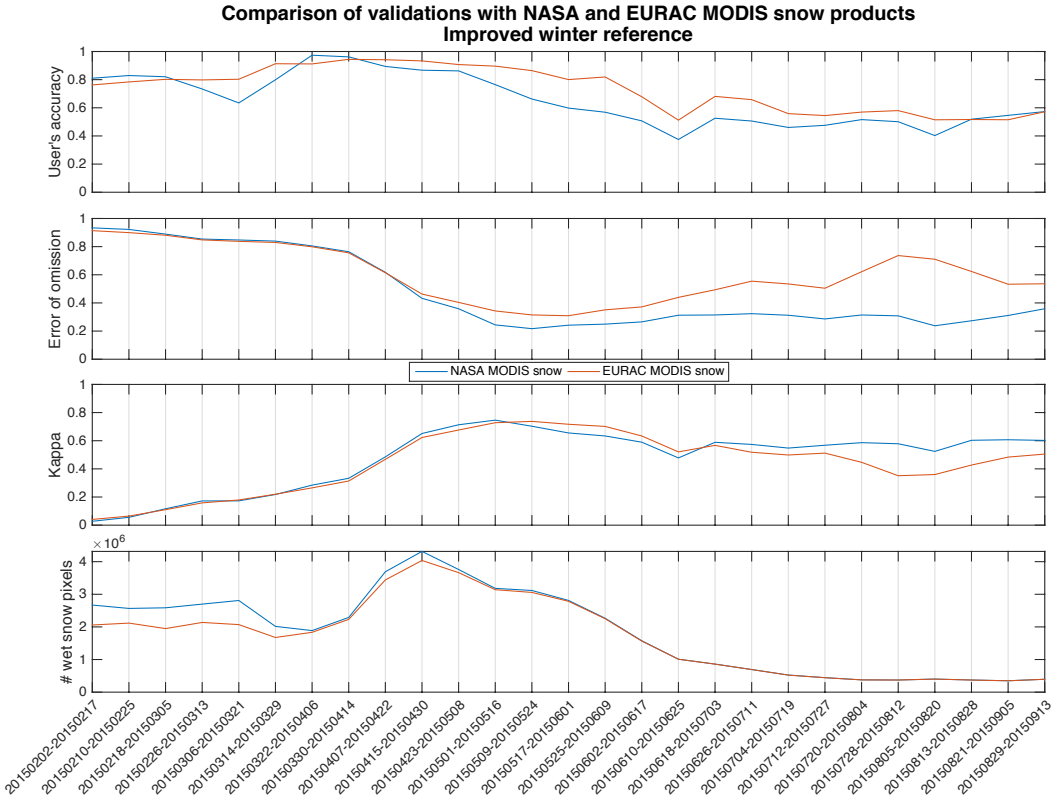

Figure 31. Comparison of accuracies of wet snow maps produced with the improved winter reference and validated against the NASA and the EURAC MODIS snow product.

The reason for the lack of improvement in accuracy despite the higher spatial resolution could be partly explained by the quality of the EURAC snow data. Notarnicola et al. (2013b) reported a mean overall accuracy of the EURAC snow product of around 88% when compared to Landsat 7 images, which is well below the reported accuracies of the NASA snow product of around 93% to 99% (Hall & Riggs, 2007). An investigation of the time series of daily EURAC snow cover maps further revealed large fluctuations in quality. While some daily maps appeared to be of very good quality, others were very noisy, featured a high number of unclassified pixels, clear artefacts and some obvious misclassifications of cloud cover as snow, particularly during summer months (see examples in Figure 32). Combination of these daily maps into 16-day composites to match the temporal resolution of the radar data added up those errors and led to a generally lower quality snow map compared to the NASA product. The higher level of noise and artefacts therefore mostly offset the benefits of the higher spatial resolution in terms of accuracy. As a result, the EURAC MODIS snow product did not present a gain in the context of this study and were not used any further.

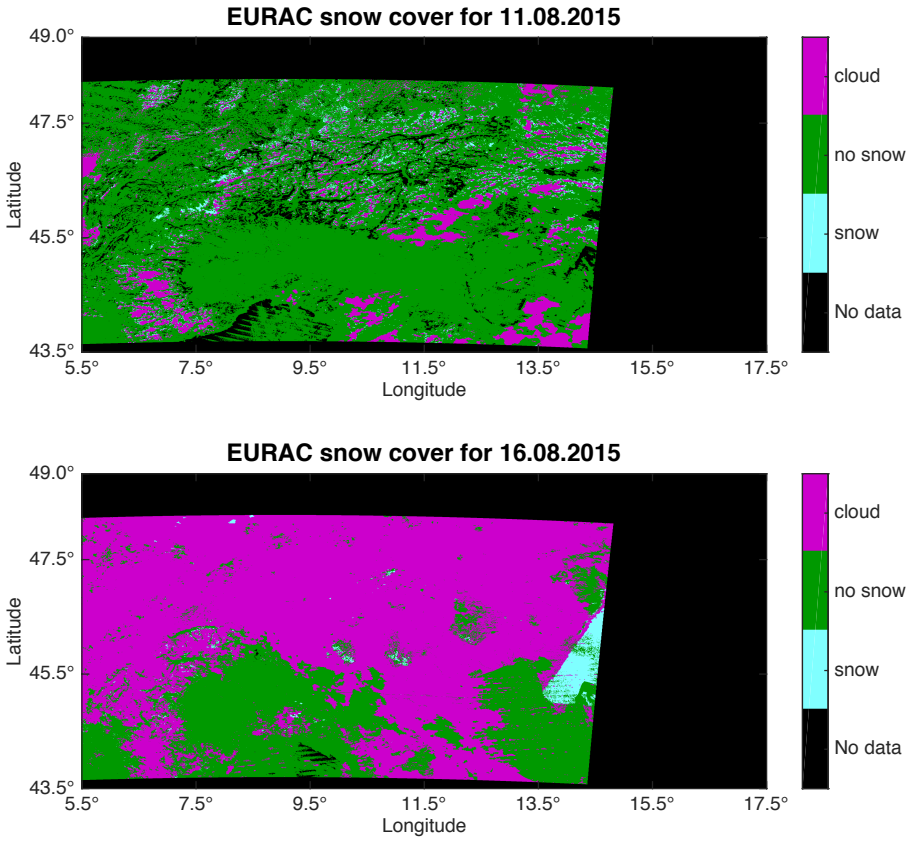

Figure 32. Examples of problems observed with the EURAC MODIS snow product: noisy snow classification and data gaps (top) and artefacts misclassified as snow (bottom).

4.2.8 Summary of the final algorithm settings

A number of variations on the input datasets and settings of the wet snow mapping algorithm originally introduced by Rott & Nagler (1995) were tested and compared in the present study. Based on the results, the final algorithm was set up as follows:

- Forested areas and water bodies were masked out using the CORINE land cover map.
- A post-classification correction of misclassified snow pixels by means of a length-of-snow-season map proved to be effective and was adopted in the algorithm.
- Subdividing the wet snow thresholds by land cover or elevation only produced significant changes in one case: when wet snow mapping was based on the simple summer reference image, a subdivision by land cover could correct some of the errors introduced by the high-altitude wet snow contamination of the reference image. However, the classification accuracies achieved from applying subdivided thresholds to the simple summer reference were still lower than the ones achieved by applying a single threshold to the snow-adjusted summer reference.

Therefore the subdivision of thresholds was deemed ineffective and was not adopted in the final algorithm.

- The snow-adjusted summer reference produced more accurate wet snow maps than the simple summer reference. Similarly, the improved winter reference produced more accurate maps than the simple winter reference. No clear favourite between the improved winter reference and the snow-adjusted summer reference could be determined. The improved winter reference tended to work better in early snowmelt season up to mid-May, while the snow-adjusted summer reference was superior in late spring and summer months. As a consequence, the final algorithm calculated two wet snow maps for every input image; one based on the improved winter reference, and one based on the snow-adjusted summer reference.
- A combination of VH- and VV-polarisations produced the best results when considering the entire melting period. A weighted average of the backscatter differences of VH and VV with a weight of 0.4 for VH and 0.6 for VV proved to be the best compromise. The corresponding wet snow thresholds were -1.1 dB when applying the improved winter reference and -2.3 dB when applying the snow-adjusted summer reference.
- A shortening of the composite period length from 16 to 8 days did not achieve any improvement in overall accuracy due to lack of sufficient radar data. The final algorithm therefore only considered 16-day composites.
- Validation of the wet snow maps against the higher-resolution EURAC snow product did not yield any improvements due to the lower overall quality of the EURAC snow product compared to the NASA product. The EURAC product was therefore not considered any further.

4.3 Application of the final wet snow map algorithm

4.3.1 Application to snow melt season of 2015

With the algorithm set as described above, a wet snow map time series was produced, starting in February of 2015 and running through August 2015. Figure 33 shows the accuracy measures of the resulting wet snow maps. By applying the improved winter reference to images acquired from February to April and the snow-adjusted summer reference from May to August, a mean user's accuracy of 76% over the entire period was achieved. The kappa coefficient was very low during early snowmelt season due to widespread dry snow cover. Once the majority of snow cover became wet by the end of April, kappa values of around 0.7 were achieved, indicating good overall agreement between Sentinel wet snow maps and MODIS snow maps. The complete confusion matrices can be found in Table 9 and Table 10 in the appendix A.4.

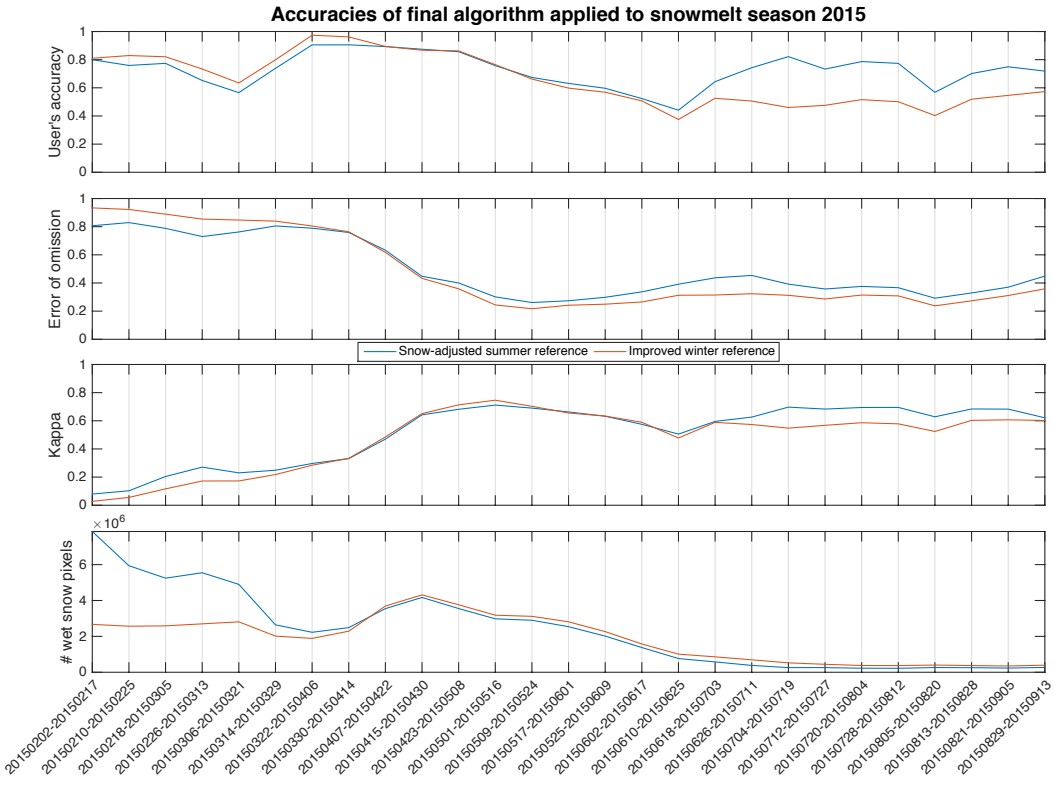

Figure 33. Accuracy measures for the wet snow maps of the snowmelt season of 2015, produced with the final algorithm settings.

Wet snow covered approximately 16'000 km^2 or 2.8% of the study area in the beginning of February, reached its widest spread in mid-April with an area of roughly 26'000 km^2 or 4.5% of the study area, and then retreated to approximately 1'600 km^2 or 0.3% of the study area by the end of August. Over the next pages, an excerpt of the wet snow cover time series is pictured, showing one wet snow map per month (Figure 34). The image acquired in February shows some clear artefacts caused by backscatter differences between single acquisition tracks. These were partly caused by data gaps in the corresponding LRW image, and partly by the generally short-lived nature of wet snow at lower elevations. It was possible that wet snow was present during the acquisition of one satellite track within the 16-day period, but was already gone by the time the track next to it was recorded. Depending on the amount of overlap between the single tracks, those differences could lead to abrupt changes in wet snow cover from one track to another. This turned out to be a major limitation of wet snow mapping in the early melting season with 16-day composites (see also chapter 5.4.2). From March onwards, this problem became less dominant, and the wet snow maps describe the retreat of the snow cover into higher altitudes during spring generally well.

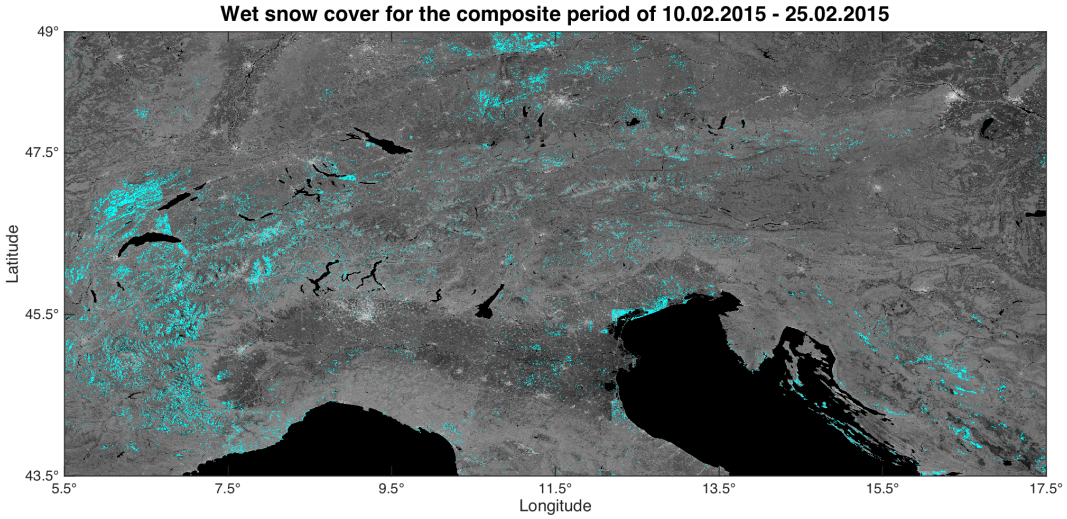
Wet snow cover for the composite period of 10.02.2015 - 25.02.2015
49°
47.5°
45.5°
43.5°
Latitude
5.5°
7.5°
9.5°
11.5°
13.5°
15.5°
17.5°
Longitude

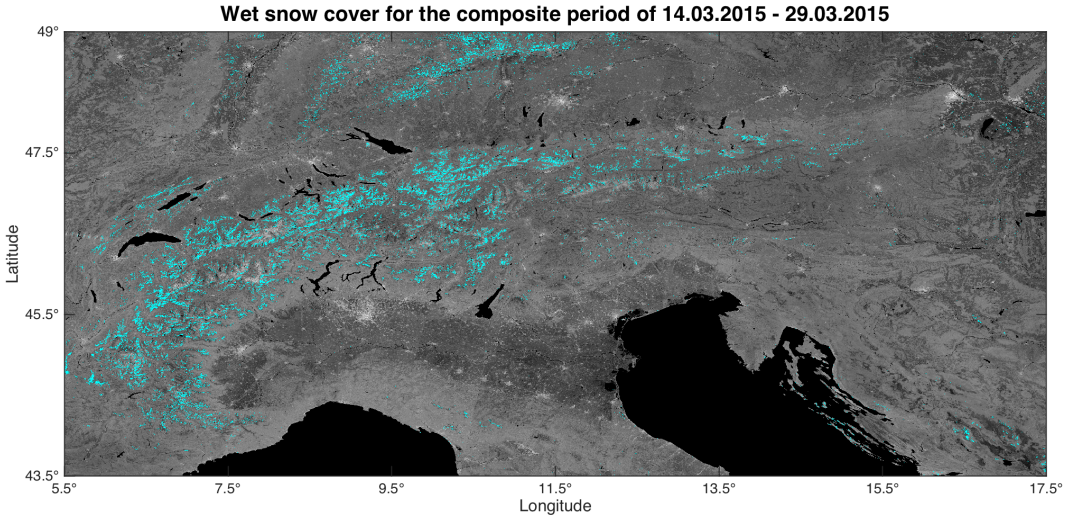
Wet snow cover for the composite period of 14.03.2015 - 29.03.2015
49°
47.5°
45.5°
43.5°
Latitude
5.5°
7.5°
9.5°
11.5°
13.5°
15.5°
17.5°
Longitude

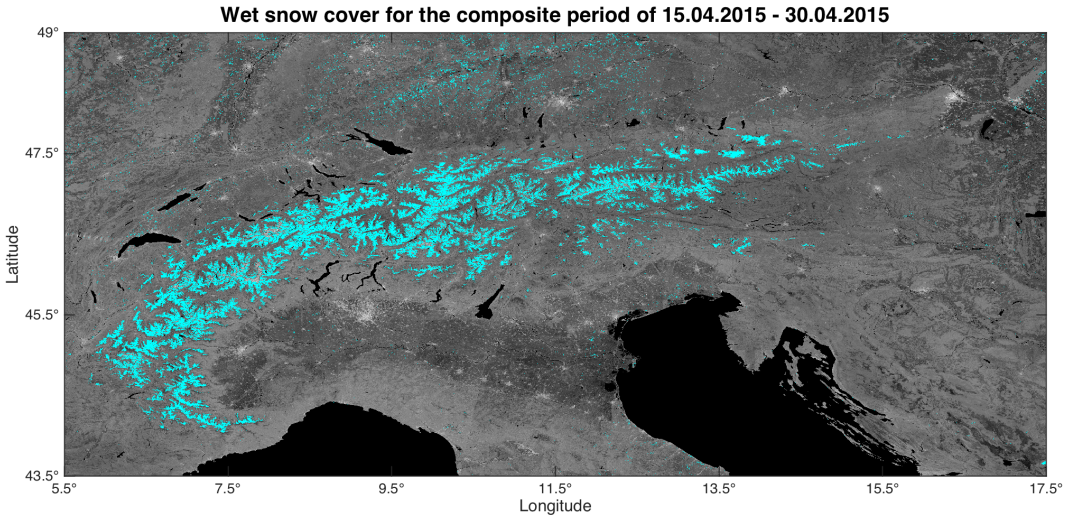
Wet snow cover for the composite period of 15.04.2015 - 30.04.2015
49°
47.5°
45.5°
43.5°
Latitude
5.5°
7.5°
9.5°
11.5°
13.5°
15.5°
17.5°
Longitude

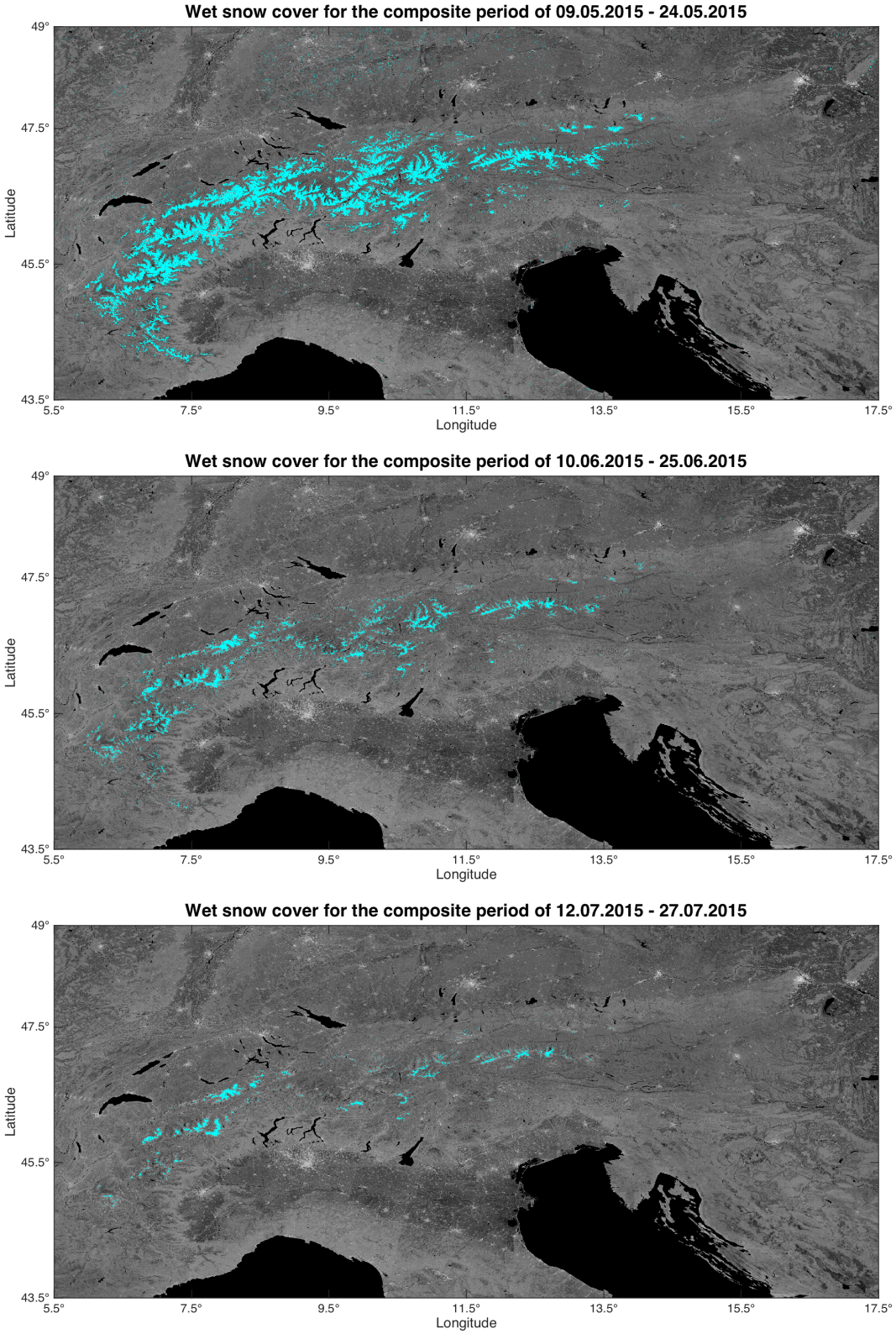

Figure 34. Time series of wet snow maps over the snowmelt season of 2015 (one image per month), derived with the final algorithm from 16-day LRW composites. Blue: wet snow. Background: Improved winter reference image for VH-polarisation.

4.3.2 Application to snow melt season of 2016

The final algorithm was additionally applied to the most recent Sentinel-1 data from the snowmelt period of 2016. While the LRW data was available in near-real time, the MODIS data was usually publicised with a delay of one to two months, which limited the accuracy assessment of the 2016 wet snow cover time series to the time period of February to the beginning of June. The results showed similar overall trends to the 2015 results. The mean user's accuracy was 79%, with the improved winter reference slightly outperforming the snow-adjusted summer reference. Due to the lack of validation data of the late melting season, it could not be assessed whether the snow-adjusted summer reference would have outperformed the improved winter reference during summer months. Kappa values were again very low during early snowmelt due to widespread dry snow cover, but reached good values of around 0.7 by April, indicating generally good agreement between Sentinel and MODIS snow cover maps. The complete confusion matrices can be found in Table 11 and Table 12 in the appendix A.4.

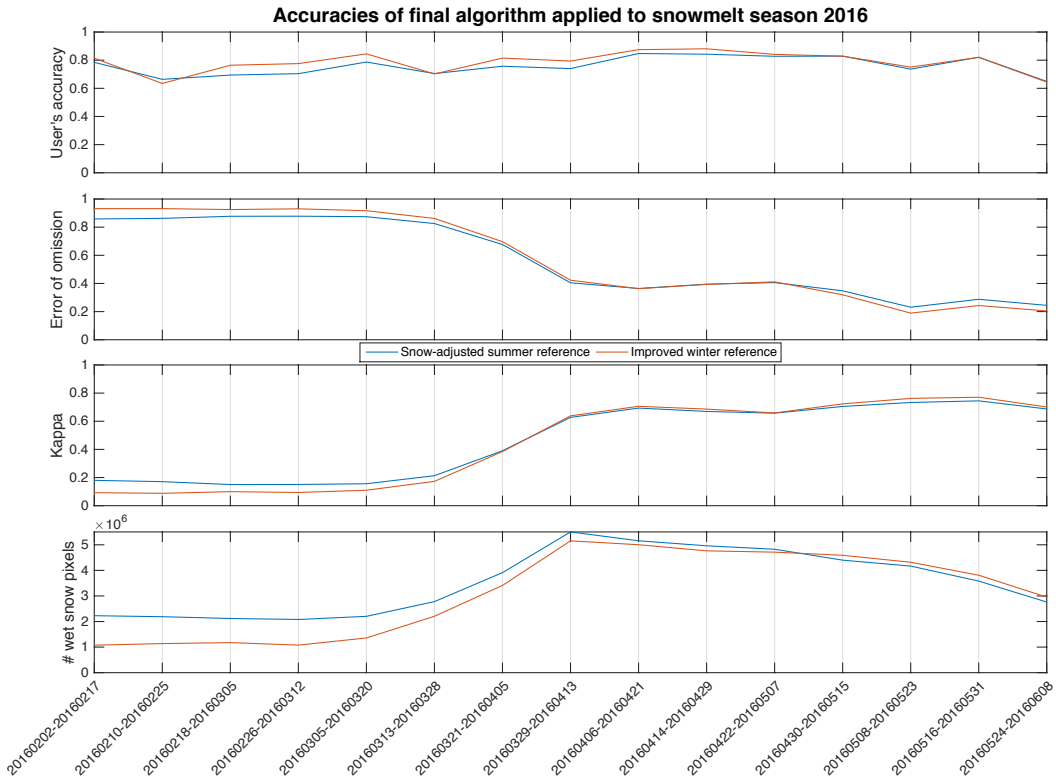

Figure 35. Accuracy measures for the wet snow maps of the snowmelt season of 2016, produced with the final algorithm settings.

The total wet snow cover area in February 2016 was significantly lower than in 2015, only covering approximately 6'400 km^2 or 1.1% of the study area. Maximum wet snow cover was reached by the end of March, with coverage of 31'000 km^2 or 5.4% of the study area. The images on the next two pages (Figure 36) show one wet snow map per month for the melting season of 2016. The February-image displays less between-track

artefacts than the one from 2015. This might partly be due to the generally smaller amount of snow that was present in February of 2016 compared to 2015, and partly due to the higher number of individual radar acquisitions that were available to produce the LRW composite, which increased the amount of radar track overlap.

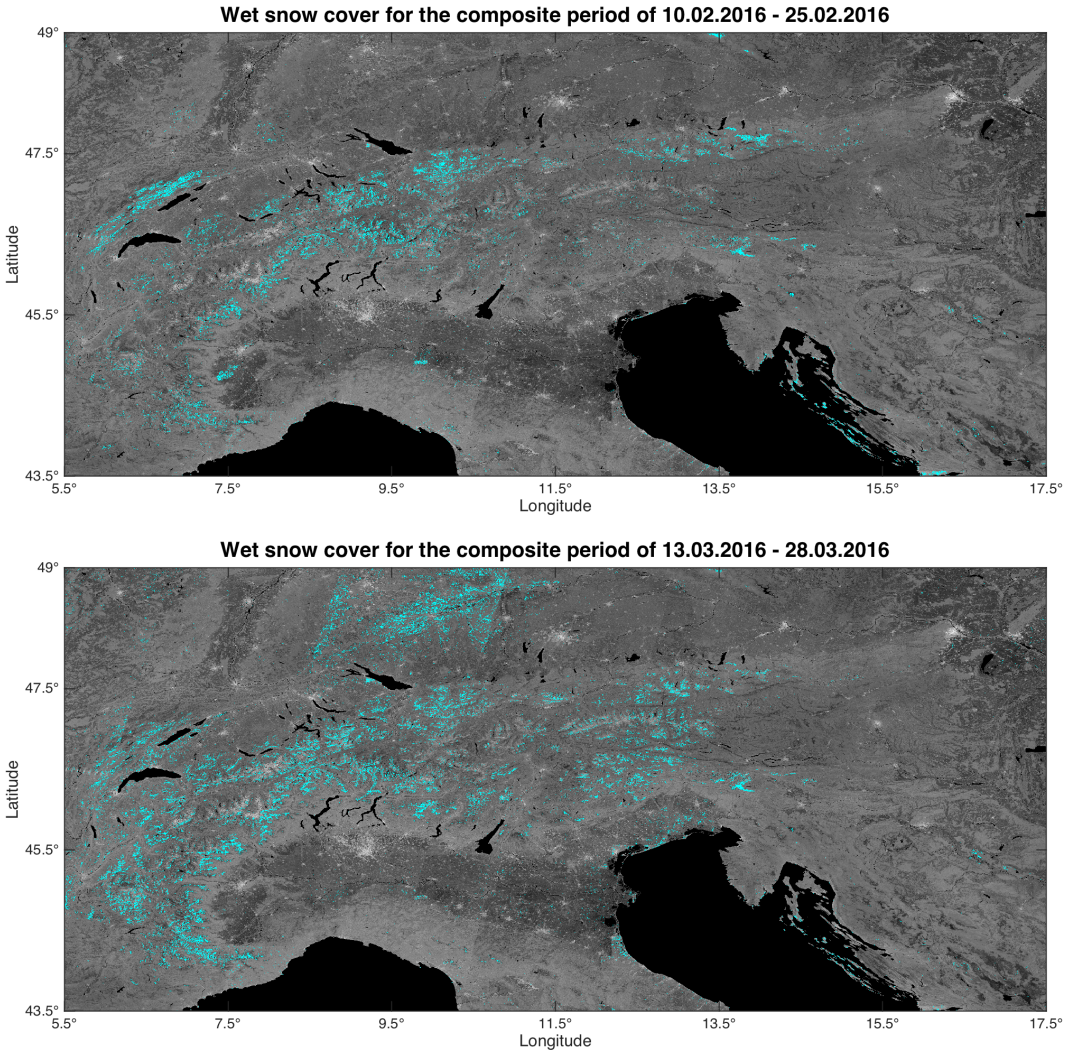

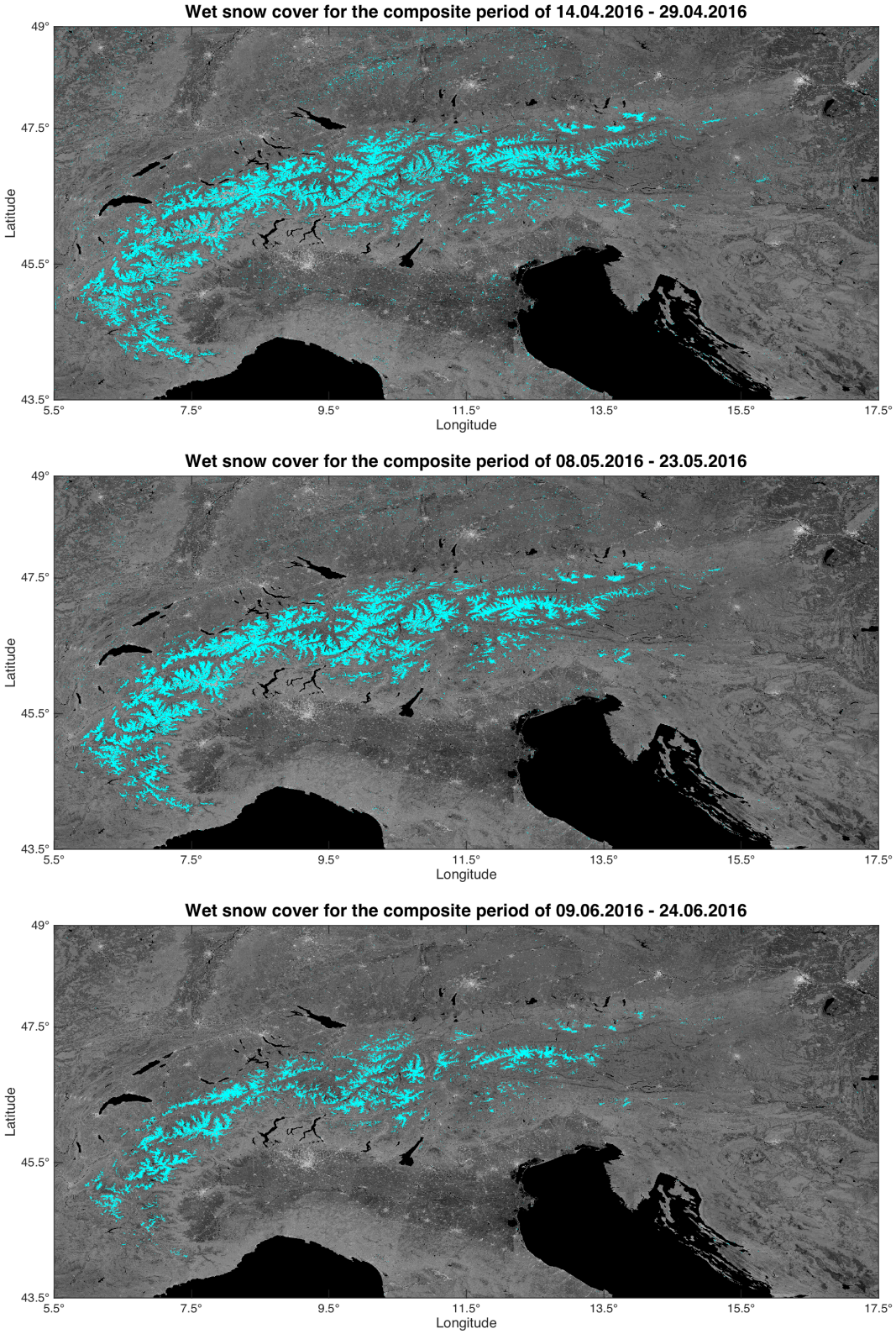

Figure 36. Time series of wet snow maps over the snowmelt season of 2016 (one image per month), derived with the final algorithm from 16-day LRW composites. Blue: wet snow. Background: Improved winter reference image for VH-polarisation.

5 Discussion

In this study, a method to map wet snow cover area originally introduced by Rott & Nagler (1995) for ERS-1 data was adapted to Sentinel-1A SAR data that was composited by means of local resolution weighting (LRW; see Small, 2012). A variation of input datasets and different algorithm settings were compared and validated. Results of those comparisons were described in chapter 4. In this chapter the different findings are linked and the performance and applicability as well as some limitations of the used methods are discussed.

5.1 General performance of Sentinel-1A LRW wet snow mapping

After implementing and comparing all algorithm adjustments, the final wet snow mapping algorithm was set up. It first masked out all forested areas and water surfaces using the CORINE land cover map. Then it calculated the difference between the backscatter in dB of any given investigation LRW composite and of a dry/no snow reference image. For investigation images acquired before mid-May, the improved winter reference (see chapter 3.2.4) was applied, for images acquired later in the melting season, the snow-adjusted summer reference (see chapter 3.2.3) was preferred. The backscatter differences of VH- and VV-polarisations were then combined by calculating a weighted average between the two, with a weight of 0.4 for VH and 0.6 for VV. Next, wet snow areas were identified by applying a threshold of -1.1 dB to difference images produced with the improved winter reference and a threshold of -2.3 dB to difference images produced with the snow-adjusted summer reference. A post-classification correction based on a length-of-snow-season map produced from a 15-year MODIS time series (see chapter 3.5) was then applied to remove misclassified wet snow pixels. Finally, the wet snow maps were validated against 500 m resolution MODIS snow maps.

With this algorithm, the Sentinel LRW products demonstrated good capability for wide area wet snow mapping. By using the improved winter reference for scenes acquired up to mid-May and the snow-adjusted summer reference for the later acquisitions, a mean user's accuracy of 76% for the period of February through August 2015 and 79% for the period of February through May 2016 was achieved. Individual maps achieved user's accuracy of up to 97%. Major drops in user's accuracy down to 43% in June 2015 could be partly explained by large data gaps in the Sentinel composite and high percentage of residual cloud cover in the MODIS validation image (see chapter 4.2.4); therefore, those values were not seen as evidence for bad algorithm performance. The achieved accuracies agreed well with the results from a similar investigation carried out by Rohner (2014). He used a similar algorithm based on C-band LRW composites from ENVISAT ASAR and Radarsat-2 acquisitions to map wet snow cover over Switzerland, achieving user's accuracies of between 76% and 90%.

The Cohen's kappa coefficient (Cohen, 1960) was calculated as a measure of overall agreement between Sentinel wet snow maps and MODIS snow maps. Kappa values were

very low for acquisitions from February and March. This could be partly explained by the differences between Sentinel and MODIS in terms of what the respective products displayed: The MODIS snow product mapped the entire snow pack, while Sentinel could only detect wet snow. As most snow present in the early melting season was still dry, it was invisible to the radar sensor, leading to large differences between Sentinel and MODIS snow maps. Around the end of March and beginning of April, the snow pack became wet on a large scale, making the Sentinel and MODIS snow maps more comparable. The achieved kappa values in this later period were scattered around 0.7, indicating good overall agreement between Sentinel and MODIS snow maps.

5.2 Assessment of different backscatter reference images

A backscatter reference image can be produced from any radar image that features as little wet snow cover as possible. Nagler & Rott (2000) suggested to average multiple SAR images acquired either during cold winter months, when the entire snow pack was frozen, or during summer months, when all snow has melted off. In the present study it was demonstrated that this approach could be problematic if the study area is very large and features several different climate regimes. No winter acquisition featuring freezing temperatures over the entire area was available as reference. No completely snow-free summer acquisition was available, either, as the study area featured several high-altitude regions that were snow-covered all year round. Both winter and summer reference images therefore inevitably featured some degree of wet snow contamination, which led to errors in the snow mapping process.

Two improvements on the simple averaging of winter or summer acquisitions for reference generation were proposed in this study: 1) The snow-adjusted summer reference, which used summer acquisitions as reference for all snow-free areas, and winter acquisitions for any high altitude areas with persistent snow cover (see chapter 3.2.3); and 2) the improved winter reference, which was composited from pixels chosen by applying masks of freezing temperatures to each individual radar acquisition (see chapter 3.2.4). Investigation of wet snow maps produced over the entire snowmelt season of 2015 revealed that these two improved approaches outperformed the simple averaging approach over the entire time series. The application of one of those approaches is therefore recommended for studies that simultaneously investigate large areas and/or a wide range of elevations. Between the two improved approaches, no clear favourite emerged. The improved winter reference generally worked better during late winter and spring. From the end of May onwards, the snow-adjusted summer reference yielded higher user's accuracies. This was most likely due to backscatter differences between winter and summer scenes other than snow-induced differences. During summer, vegetation is generally higher and more developed than during winter, which typically increases the volume scattering of the radar signal. Large differences in vegetation between investigation and reference scene could lead to backscatter differences that were big enough to be classified as wet snow, even though the cause of the differences lay in the amount of biomass. To minimise such sea-

sonal distortions, it is recommended to choose the appropriate reference image based on the acquisition date of the investigation scene. This is in accordance to the findings of Rohner (2014), who noted that the reference scene should be temporally close to the investigation scene.

5.3 Threshold extraction

Wet snow areas were separated from dry snow and snow-free areas by subtracting a reference image from the investigation image and applying a threshold to the resulting difference image. Rott & Nagler (1995) suggested a wet snow threshold of -3 dB for ERS-1 C-band radar images, based on comparison of field observations and SAR data. This value has subsequently been applied in a multitude of studies using ERS data (e.g. Baghdadi et al., 1997; Nagler & Rott, 2000) and ENVISAT ASAR data (e.g. Storvold et al., 2006; Longepe et al., 2009; Schaub, 2011; Rohner, 2014). Recently, the same algorithm was adapted to Sentinel-1A data, where an adjusted threshold of -2 dB was chosen based on histograms of the backscatter differences (Nagler et al., 2016). The same histogram approach was used in this study: Backscatter from snow-covered areas was divided into warm and cold snow by applying temperature masks. Backscatter histograms of those two classes were then used to identify a separating threshold (see chapter 3.3). It was found that the threshold was dependent on the applied reference image. When the final algorithm settings (see chapter 4.2.8) were applied, a wet snow threshold of -1.1 dB was identified for the improved winter reference, while -2.3 dB was used for the snow-adjusted summer reference. This large difference implies that the threshold should always be determined individually based on the applied reference image.

A separate analysis was carried out to investigate whether subdividing the thresholds by land cover or elevation could improve the overall wet snow map accuracy (see chapter 4.2.3). The investigation revealed that individual wet snow thresholds per land cover class showed considerable differences (see Table 6 in appendix A.3). The thresholds were lowest for *glaciers* and *non-vegetated areas* and increased for *scrubland*. *Agricultural areas* and *urban areas* featured backscattering differences between cold and warm snow that were too small to clearly identify a wet snow threshold. These trends were consistent with the findings of Koskinen et al. (1997), who noted that the backscattering differences in C-band SAR between wet snow and dry/no snow decreases with increasing biomass. No such trend was expected for subdivision by elevation, as radar backscatter is generally not influenced by altitude. However, the wet snow thresholds showed significant differences for the different elevation zones (see Table 6 in appendix A.3). This could be partly explained by the strong correlation between land cover and elevation: densely vegetated land cover classes like *forests* and *agricultural areas* were predominately found in elevations below 2000 m.a.s.l., while sparsely or non-vegetated classes like *scrubland*, *non-vegetated areas* and *glaciers* were more prominent above 2000 m.a.s.l. The backscatter differences and resulting differences in thresholds had therefore the same cause as with the subdivision by land cover. As a consequence, subdivision by elevation did not provide

any new information compared to subdivision by land cover. Despite the differences in thresholds subdivided by land cover, the final wet snow maps produced with subdivided thresholds showed almost no difference compared to maps produced with a single threshold over all land cover classes (see chapter 4.2.3). Threshold subdivision was therefore deemed ineffective and was not adopted in the final algorithm.

5.4 Limitations

5.4.1 Validation with the MODIS snow product

The accuracy measures provided in this thesis give a good general indication on the overall performance of the wet snow mapping algorithm. However, they should not be interpreted as absolute accuracies of the resulting wet snow maps for several reasons: Firstly, the MODIS snow product used as validation was in itself a classification that came with inherent uncertainties and could therefore not be seen as absolute ground truth. While the overall quality of the MODIS snow maps was generally good, with accuracies beyond 93% (Hall & Riggs, 2007), any present classification errors were inevitably propagated into the Sentinel wet snow map validation. Secondly, as mentioned earlier, the MODIS snow product mapped the entire snow pack, while the radar sensor could only detect wet snow. This difference led to lower accuracy values for the Sentinel wet snow maps in early snowmelt season that were ultimately not a reflection of their actual quality. For this reason, the main accuracy measure used in this study was the user's accuracy, as the non-detectable dry snow cover did not influence it. Thirdly, the NASA MODIS snow product used as standard validation dataset featured a significantly coarser spatial resolution of 500 m compared to the roughly 90 m resolution of the Sentinel composite data. The validation could therefore not account for the full level of detail that the wet snow maps could in theory provide, most likely leading to an underestimation of the actual wet snow map accuracy. To investigate this effect, a comparison of wet snow map validations based on a 500 m NASA snow product and a 250 m EURAC snow product was carried out. This analysis did not, however, provide any definitive insights due to the generally lower quality of the EURAC snow product (see chapter 4.2.7). Better results could possibly be achieved by using snow maps retrieved from higher-resolution optical sensors such as Landsat or Sentinel-2 as validation data. The smaller footprint of those sensors compared to MODIS would have required significantly more pre-processing effort and data storage capacity, pushing their application beyond the scope of this thesis. Furthermore, higher resolution validation data could not have prevented the fourth problem encountered in the validation process of the wet snow maps: the long composite period of 16 days. This problem is discussed in more detail in the following sub-chapter.

5.4.2 Usefulness of 16-day radar composites for snow monitoring

Snow cover area can change drastically within a very short time period. A single snowfall event can greatly increase the total snow-covered area within a few hours, while a warm weather period can lead to an equally fast decrease of snow-covered area. This holds true

especially for areas at lower elevations that typically do not feature continuous snow cover during winter months. Operational, satellite-based monitoring of snowmelt therefore requires revisit times of between one and five days (Malenovský et al., 2012; Key et al., 2007). This requirement was not fulfilled with the 16-day LRW composites used in this thesis. As described in chapter 2.2.2, even this comparatively long time span could not guarantee gap-free composites over the entire time series. A shortening of the composite period length without major data gaps would therefore only be possible if the study area were greatly reduced in size. Since the focus of this study was on wide-area wet snow mapping, the longer composite period length was accepted as necessary prerequisite for sufficient data coverage over the entire Alps.

The main problem associated with a long temporal baseline of LRW composites was the mixing of different backscatter signals. The final backscatter value of any composite pixel represented the weighted average of all backscatter values measured at that pixel over a 16-day period. If wet snow was present during the first days of the composite period, but melted within the 16 days, the resulting composite backscatter value represented a mixture of wet snow and no snow. As the snow mapping was strictly binary, the results of such cases were wrong no matter whether those particular pixels were ultimately mapped as wet snow or as snow-free. This problem was particularly severe for areas at elevations below 2000 m.a.s.l., where the snow pack was generally thin and could completely melt over large areas within only a few days. The snow mapping capabilities of 16-day composite images was therefore severely limited for areas below 2000 m.a.s.l.

A further problem was that some parts of the study area were sometimes only imaged on one or two days within the 16-day period. They therefore did not represent the mean snow conditions over the 16 days, but the present conditions on those particular days. This could lead to composites that represented the snow conditions of different points in time within a single image. This problem, together with the mixing of different backscatter signals, caused an uncertainty about what exactly a wet snow map derived from a 16-day LRW composite represented: it was neither the maximum nor the minimum wet snow extent over the corresponding 16 days, but some not exactly quantifiable mean value between these two extremes. This stood in contrast to the MODIS snow maps that represented the maximum snow extent over the composite period, which further complicated the validation process.

Shorter composite time periods should reduce these two problems. Accuracy assessment of snow maps produced from shorter composite periods should therefore yield better values. This hypothesis was tested by mapping wet snow extend from 8-day radar composites. However, at the time of writing not enough Sentinel data was available to produce sufficiently complete coverage of the study area over an 8-day period. Any potential improvements in accuracy of the resulting wet snow maps due to reduced signal mixing were therefore offset by the lack of data (see chapter 4.2.6). By the end of 2016, Sentinel-1B radar imagery should become readily accessible, effectively doubling the amount of available data. This should enable complete coverage of the study area in eight days or

even less. A future repetition of the comparison between 8-day and 16-day snow maps with this new data should therefore produce more telling results.

5.4.3 Problems with radiometric stability of Sentinel-1A data

High radiometric stability of SAR data is crucial for accurate surface monitoring. Variations in radar backscatter should be exclusively caused by variations in physical surface conditions and not by imprecisions in the radar calibration. A recent study by El Hajj et al. (2016) assessed the radiometric stability of Sentinel-1A data acquired between the 1st of October 2014 and the 1st of February 2016. They found that data acquired prior to the 19th of March 2015 and after the 25th of November 2015 showed very little variation in the backscattering coefficient σ^0, indicating good calibration. However, data acquired between the 19th of March and 25th of November 2015 displayed a mean increase in σ^0 of nearly 1 dB for both VH and VV polarisations compared to the images acquired before and after this period (El Hajj et al., 2016). As this period covers the majority of the snowmelt season of 2015, a distorting effect on the wet snow thresholds retrieved in the present thesis had to be expected, depending on the used reference image. This effect could be observed in the histograms calculated for the threshold retrieval.

The summer reference was produced from images that were acquired during the period of increased σ^0. Since most pixels selected as *warm snow pixels* in the histogram process (see chapter 3.3) were also derived from this period, the backscatter overestimation was corrected by calculating the backscatter difference. However, most *cold snow pixels* were derived from the months of January and February, which lay outside of the period of increased σ^0. The backscatter difference calculated with the summer reference was therefore too low, leading to a shift of the cold snow peak towards lower backscatter difference values (see Figure 37, left). The winter reference was calculated from images acquired in January of 2015 and 2016, thus representing the period of correct σ^0. Applying the winter reference therefore led to the inverse effect on the histograms: the cold snow peak is located correctly, while the warm snow peak is shifted towards higher backscatter difference values (see Figure 37, right). As a consequence, the wet snow threshold for the winter reference (-1 dB) is roughly 1 dB higher than the one for the summer reference (-1.9 dB), matching the 1 dB shift in σ^0 caused by the calibration error described by El Hajj et al. (2016). It is reasonable to assume that without this calibration error, the different reference images would have produced more similar wet snow thresholds. The improved winter reference and the snow-adjusted summer reference were both produced from images acquired inside and outside of the period with increased σ^0, which slightly dampened, but could not eliminate the distorting effect of the calibration error on the thresholds.

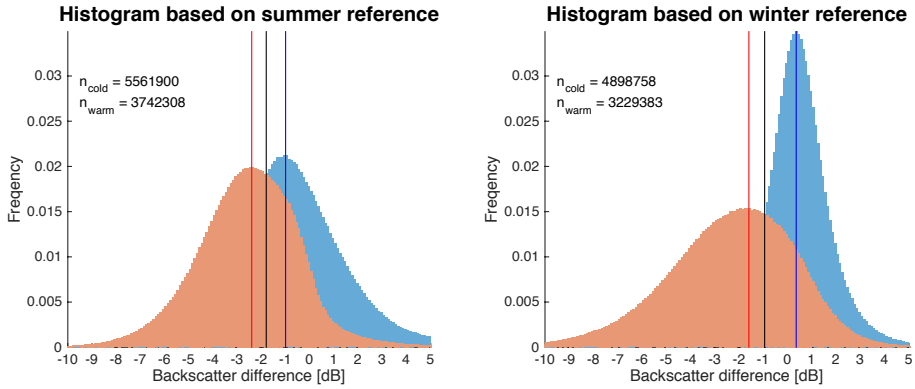

Figure 37. Normalised histograms of VH-backscatter difference from snow-covered pixels from all land cover classes for elevations above 2000 m.a.s.l. Red peak: *warm snow* pixels (T > +4°C). Blue peak: *cold snow* pixels (T < -1°C). Black line: extracted threshold.

Since the period of increased σ^0 almost matched the main investigation period, the extraction of individual thresholds per reference image could at least partly compensate the distortions caused by the calibration error. If for example the winter reference (produced from images with correct σ^0) was applied to an image acquired in May 2015 (within period of increased σ^0), the resulting difference image exhibits an overestimation of backscatter difference. This overestimation is however partly compensated by applying the higher threshold extracted for the winter reference. In general, the wet snow maps should therefore not be impaired too severely. Still, some degree of resulting error had to be expected. These errors could have been prevented if the increased σ^0 was corrected in the original Sentinel images acquired between the 19th of March and 25th of November 2015, before any further analysis was carried out. Unfortunately, the paper by El Hajj et al. (2016) was published too late to incorporate their findings into the data analysis of the present thesis.

6 Conclusion and outlook

This thesis investigated the adaptability of existing methods for wet snow mapping based on multitemporal radar backscatter thresholding to Sentinel-1 LRW composite images. The goal was to simultaneously map the entire European Alps, thereby leaving the local to national scale that was used in most previous studies and move towards a multi-national scale, including a wide variety of land cover classes, climate regimes and elevations. Level 3 LRW composites from Sentinel-1A C-band SAR were available with 16- and 8-day temporal baselines for the period from the 1st of October 2014 to the end of June 2016. The main investigation period was the extended snowmelt period of 2015, spanning from February to August. Conclusions from those investigations were combined in a final wet snow mapping algorithm that was then applied to images from the snowmelt period of 2016. Validation of the wet snow maps was done by comparison with snow maps derived from optical MODIS data.

In general, the wet snow mapping algorithm showed good performance during the main and late snowmelt season and demonstrated its applicability to wide-area investigation

scenes. Some difficulties were encountered when mapping wet snow at lower elevations, which were mainly caused by the long temporal baseline of 16 days and the subsequent mixing of wet snow and snow-free ground backscatter signals. This limited the algorithm performance for areas at lower elevations and during the early snowmelt season.

A variety of adjustments to the wet snow mapping algorithm were proposed and tested in order to obtain the best possible results. The incorporation of a DEM and daily temperature data enabled the extraction of more representative wet snow thresholds. A land cover map was used to mask out water surfaces and forested areas. This improved the overall quality of the classification, as wet snow mapping within forested areas proved to be infeasible. Major improvements in the final map accuracies could be achieved by applying a length-of-snow-season map to the classified image. This map was calculated from the available 15-year time series of MODIS data and was able to correct the majority of pixels falsely classified as wet snow.

The importance of a high-quality reference backscatter image could be demonstrated by comparing four different approaches of reference calculation. Two advanced methods were presented that managed to significantly reduce the wet snow contamination of the reference image and therefore improve the quality of the wet snow classification compared to the simple usage of winter or summer acquisitions as reference. Instead of using one fixed wet snow threshold for all analyses, individual thresholds were determined for each reference image and polarisation. It could be demonstrated that the different reference images produced substantially different thresholds. Some of those differences might have been caused or amplified by radiometric instability of the Sentinel images. A correction of those instabilities would likely reduce the differences between the different thresholds. Nevertheless, an individual determination of the wet snow threshold for the applied reference image is recommended. An additional analysis was conducted to assess whether a further subdivision of thresholds by land cover class and elevation zone could increase the overall quality of the wet snow maps. However, this subdivision did not provide any significant improvement for the final algorithm.

Differently weighted combinations of VH and VV polarisations were tested against each other. Which combination produced the best results depended on the image date and the chosen reference image. By considering the entire snowmelt season and both of the improved reference scenes, a combination of polarisations with a weight of 0.4 for VH- and 0.6 for VV-polarisation was found to be the best compromise.

Some problems and limitations were observed and discussed due to the relatively long 16-day temporal baseline of the composite images. A shortening of the period to eight days or fewer was hypothesised to improve the overall quality of the wet snow maps. However, no clear conclusion could be reached in that respect due to a lack of sufficient Sentinel-1 acquisitions. Similarly, no clear verdict could be given on the question of whether the use of the 250 m MODIS snow product could enhance the accuracy assessment. It was assumed that the higher level of detail compared to the standard 500 m reso-

lution would improve the wet snow map accuracies, but the generally lower quality of the 250 m MODIS product compared to the standard 500 m product did not allow any conclusive insights.

The final wet snow mapping algorithm worked well for wide-area Sentinel-1 16-day LRW composites. It allowed unsupervised wet snow classification of entire time series of composite images and could be adapted into an operational snow mapping system. The resulting snow maps allowed the tracking of snowmelt processes over large areas and clearly visualised the retreat of the snow cover into higher altitudes during the snowmelt season. However, they offer limited practicability for detailed hydrological applications due to the temporal blurring caused by the long composite period length. The present thesis should therefore chiefly be seen as a precursor to future studies that will incorporate more SAR data and can therefore shorten the temporal baseline of wide-area composite images. Such studies should become feasible in the near future, as the second Sentinel radar satellite, Sentinel-1B, was already launched and is at the time of writing in its in-orbit commissioning phase. Operational Sentinel-1B data should become available by the end of 2016 and will allow at least a bisection of the composite period length. With RADARSAT constellation, the Canadian Space Agency plans an additional C-band SAR mission. This mission is scheduled to launch in 2018 and will consist of three identical radar satellites, achieving a combined revisit time of four days (Canadian Space Agency, 2015). If data from both Sentinel-1 and all three RADARSAT constellation satellites can be combined to produce LRW images, composite periods of only a few days should be feasible. Additional incorporation of X-band data from TerraSAR-X or COSMO-SkyMed into the algorithm is also conceivable. With this increase in data availability, SAR-derived wet snow maps will offer good capabilities for hydrological analyses and climate change research over wide areas.

7 Acknowledgements

Several people contributed directly or indirectly to this thesis. First of all, I would like to thank my supervisor Dr. David Small for the many fruitful meetings and discussions over the past months as well as for providing the LRW composites tailored to my needs. Further thanks goes to Christoph Rohner for his help with the production of the dry reference, to Dr. Rogier De Jong for providing me with an R-script that greatly facilitated the download and resampling of the MODIS data, and to Dr. Felix Morsdorf for his help with Matlab. I would like to express my gratitude to Dr. Claudia Notarnicola and the EURAC research institute in Bozen, Italy, for giving me the opportunity to spend one month as guest researcher at their Institute for Applied Remote Sensing. Many thanks also to EURAC researchers Dr. Carlo Marin and Dr. Mattia Callegari for their valuable inputs and comments on my results, and to Alexander Jacob for providing me with the EURAC MODIS snow product. Last but not least I want to thank my parents and family for their continued support during my studies.

8 References

- Baghdadi, N., Gauthier, Y., & Bernier, M. (1997). Capability of multitemporal ERS-1 SAR data for wet-snow mapping. *Remote sensing of environment*, *60*(2), 174-186. DOI: 10.1016/S0034-4257(96)00180-0
- Berrisford, P., Kallberg, P., Kobayashi, S., Dee, D., Uppala, S., Simmons, A. J., Poli, P., Brugge, R., Fielding, K., Fuentes, M., Simmons, A. & Sato, H. (2011). The ERA-Interim archive version 2.0. *European Centre for Medium-Range Weather Forecasts ERA Tech. Rep, 1*, 23.
- Büttner, G., Soukup, T., & Kosztra, B. (2014). CLC2012 addendum to CLC2006 technical guidelines. *Final Draft, Copenhagen (EEA)*.
- Canadian Space Agency (2015). RADARSAT constellation. Retrieved from http://www.asc-csa.gc.ca/eng/satellites/radarsat/ on 21.07.2016.
- Cimbala, J. M. (2011). Outliers. *Penn State Univ*.
- Cohen, J. (1960). A coefficient of agreement for nominal scale. *Educ Psychol Meas*, *20*, 37-46. DOI: 10.1177/001316446002000104
- Cohen, J., Lemmetyinen, J., Pulliainen, J., Heinilä, K., Montomoli, F., Seppänen, J., & Hallikainen, M. T. (2015). The Effect of Boreal Forest Canopy in Satellite Snow Mapping—A Multisensor Analysis. *IEEE Transactions on Geoscience and Remote Sensing*, *53*(12), 6593-6607. DOI: 10.1109/TGRS.2015.2444422
- Dee, D. P., Uppala, S. M., Simmons, A. J., Berrisford, P., Poli, P., Kobayashi, S., Andrae, U., Balmaseda, M.A., Balsamo, G., Bauer, P., Bechtold, P., Beljaars, A.C.M., van de Berg, L., Bidlot, J., Bormann, N., Delsol, C., Dragani, R., Fuentes, M., Geer, A.J., Haimberger, L., Healy, S.B., Hersbach, H., Holm, E.V., Isaksen, L., Kallberg, P., Köhler, M., Matricardi, M., McNally, A.P., Monge-Sanz, B.M., Morcrette, J.-J., Park, B.-K., Peubey, C., de Rosnay, P., Tavolato, C., Thepaut, J.-N. & Vitart, F. (2011). The ERA-Interim reanalysis: Configuration and performance of the data assimilation system. *Quarterly Journal of the royal meteorological society, 137*(656), 553-597. DOI: 10.1002/qj.828
- Dietz, A. J., Kuenzer, C., Gessner, U., & Dech, S. (2012). Remote sensing of snow–a review of available methods. *International Journal of Remote Sensing*, *33*(13), 4094-4134. DOI: 10.1080/01431161.2011.640964
- El Hajj, M., Baghdadi, N., Zribi, M., & Angelliaume, S. (2016). Analysis of Sentinel-1 Radiometric Stability and Quality for Land Surface Applications. *Remote Sensing*, *8*(5), 406. DOI: 10.3390/rs8050406
- ESA European Space Agency (n.d.). Sentinel-1. Retrieved from https://earth.esa.int/web/guest/missions/esa-operational-eo-missions/sentinel-1 on 20.06.2016.
- ESRI (2015). Imagery. Retrieved from http://www.arcgis.com/home/item.html?id=483b230c56a44c33beb13f9b9ab9f88d on 27.06.2016.

- Farr, T. G., Rosen, P. A., Caro, E., Crippen, R., Duren, R., Hensley, S., Kobrick, M., Paller, M., Rodriguez, E., Roth, L., Seal, D., Shaffer, S., Shimada, J., Umland, J., Werner, M., Oskin, M., Burbank, D. & Alsdorf, D. (2007). The shuttle radar topography mission. *Reviews of geophysics*, *45*(2). DOI: 10.1029/2005RG000183
- Gao, L., Bernhardt, M., & Schulz, K. (2012). Elevation correction of ERA-Interim temperature data in complex terrain. *Hydrology and Earth System Sciences*, *16*(12), 4661-4673. DOI: 10.5194/hess-16-4661-2012
- Hall, D. K. (1996). Remote sensing applications to hydrology; imaging radar. *Hydrological Sciences Journal*, *41*(4), 609-624. DOI: 10.1080/02626669609491528
- Hall, D. K., & Riggs, G. A. (2007). Accuracy assessment of the MODIS snow products. *Hydrological Processes*, *21*(12), 1534-1547. DOI: 10.1002/hyp.6715
- Hall, D. K., Riggs, G. A., Salomonson, V. V., Barton, J. S., Casey, K., Chien, J. Y. L., DiGirolamo, N. E., Klein, A. G., Powell, H. W. & Tait, A. B. (2001). Algorithm theoretical basis document (ATBD) for the MODIS snow and sea ice-mapping algorithms. *NASA GSFC*.
- Key, J., Drinkwater, M., & Ukita, J. (2007). IGOS Cryosphere Theme Report. *WMO/TD*, *1405*, 100.
- Koskinen, J. T., Pulliainen, J. T., & Hallikainen, M. T. (1997). The use of ERS-1 SAR data in snow melt monitoring. *IEEE Transactions on geoscience and remote sensing*, *35*(3), 601-610. DOI: 10.1109/36.581975
- Longepe, N., Allain, S., Ferro-Famil, L., Pottier, E., & Durand, Y. (2009). Snowpack characterization in mountainous regions using C-Band SAR data and a meteorological model. *IEEE Transactions on Geoscience and Remote Sensing*, *47*(2), 406-418. DOI: 10.1109/TGRS.2008.2006048
- Longepe, N., Allain, S., Ferro-Famil, L., Pottier, E., & Durand, Y. (2009). Snowpack characterization in mountainous regions using C-Band SAR data and a meteorological model. *IEEE Transactions on Geoscience and Remote Sensing*, *47*(2), 406-418. DOI: 10.1109/TGRS.2008.2006048
- Malenovský, Z., Rott, H., Cihlar, J., Schaepman, M. E., García-Santos, G., Fernandes, R., & Berger, M. (2012). Sentinels for science: Potential of Sentinel-1,-2, and-3 missions for scientific observations of ocean, cryosphere, and land. *Remote Sensing of Environment*, *120*, 91-101. DOI: 10.1016/j.rse.2011.09.026
- Mätzler, C. (1987). Applications of the interaction of microwaves with the natural snow cover. *Remote sensing reviews*, *2*(2), 259-387. DOI: 10.1080/02757258709532086
- Mätzler, C., & Schanda, E. (1984). Snow mapping with active microwave sensors. *International Journal of Remote Sensing, 5*, 409-422. DOI: 10.1080/01431168408948816
- Meier, E., Frei, U., & Nüesch, D. (1993). Precise terrain corrected geocoded images. *SAR Geocoding: Data and Systems*, 173-185. Hervert Wichmann Verlag GmbH, Karlsruhe.

- MeteoSchweiz (2014). Datenportal für Experten. Retrieved from http://www.meteoschweiz.admin.ch/home/service-und-publikationen/beratung-und-service/datenportal-fuer-experten.html on 30.06.2016.
- Nagler, T., & Rott, H. (2000). Retrieval of wet snow by means of multitemporal SAR data. *IEEE Transactions on Geoscience and Remote Sensing*, *38*(2), 754-765. DOI: 10.1109/36.842004
- Nagler, T., & Rott, H. (2005, April). Snow classification algorithm for Envisat ASAR. *Envisat & ERS Symposium, 572*.
- Nagler, T., Rott, H., Ripper, E., Bippus, G., & Hetzenecker, M. (2016). Advancements for Snowmelt Monitoring by Means of Sentinel-1 SAR. *Remote Sensing*, *8*(4), 348. DOI: 10.3390/rs8040348
- NASA National Aeronautics and Space Administration (2016a). About Aqua. Retrieved from http://aqua.nasa.gov/content/about-aqua on 22.06.2016.
- NASA National Aeronautics and Space Administration (2016b). About Terra. Retrieved from http://terra.nasa.gov/about on 22.06.2016.
- NASA National Aeronautics and Space Administration (n.d.). MODIS specifications. Retrieved from http://modis.gsfc.nasa.gov/about/specifications.php on 22.06.2016.
- Notarnicola, C., Duguay, M., Moelg, N., Schellenberger, T., Tetzlaff, A., Monsorno, R., Costa, A., Steurer, C. & Zebisch, M. (2013a). Snow cover maps from MODIS images at 250 m resolution, Part 1: Algorithm description. *Remote Sensing*, *5*(1), 110-126. DOI: 10.3390/rs5010110
- Notarnicola, C., Duguay, M., Moelg, N., Schellenberger, T., Tetzlaff, A., Monsorno, R., Costa, A., Steurer, C. & Zebisch, M. (2013b). Snow cover maps from MODIS images at 250 m resolution, Part 2: Validation. *Remote Sensing*, *5*(4), 1568-1587. DOI: 10.3390/rs5041568
- Notarnicola, C., Ratti, R., Maddalena, V., Schellenberger, T., Ventura, B., & Zebisch, M. (2013). Seasonal Snow Cover Mapping in Alpine Areas Through Time Series of COSMO-SkyMed Images. *IEEE Geoscience and Remote Sensing Letters*, *10*(4), 716-720. DOI: 10.1109/LGRS.2012.2219848
- Park, S. E., Yamaguchi, Y., Singh, G., Yamaguchi, S., & Whitaker, A. C. (2014). Polarimetric SAR response of snow-covered area observed by multi-temporal ALOS PALSAR fully polarimetric mode. *IEEE Transactions on Geoscience and Remote Sensing*, *52*(1), 329-340. DOI: 10.1109/TGRS.2013.2240000
- Piesbergen, J. (2001). ERS-1 SAR-Verarbeitungs-und Datenfusionsmethoden zur Schneekartierung im Hochgebirge. Zürich, RSL Remote Sensing Laboratories, Department of Geography, University of Zurich.
- Pivot, F. C. (2012). C-band SAR imagery for snow-cover monitoring at Treeline, Churchill, Manitoba, Canada. *Remote Sensing*, *4*(7), 2133-2155. DOI: 10.3390/rs4072133
- Rees, W. G. (2005). Remote sensing of snow and ice. CRC press.
- Rees, W. G., & Steel, A. M. (2001). Radar backscatter coefficients and snow detectability for upland terrain in Scotland. *International Journal of Remote Sensing*, *22*(15), 3015-3026. DOI: 10.1080/01431160120567

- Riggs, G. A., Hall, D. K., & Salomonson, V. V. (2006). MODIS snow products user guide to collection 5. *Digital Media*, *80*.
- Rohner, C. (2014). Relating Snow Wetness Information Gained from the Intercantonal Measurement and Information System Stations in Switzerland to Envisat ASAR Backscatter. *Master's thesis*, University of Zurich, Zurich (Switzerland).
- Rott, H., & Nagler, T. (1995, July). Monitoring temporal dynamics of snowmelt with ERS-1 SAR. *Geoscience and Remote Sensing Symposium, 1995. IGARSS'95. 'Quantitative Remote Sensing for Science and Applications', International, 3*, 1747-1749. IEEE. DOI: 10.1109/IGARSS.1995.524014
- Schaub, R. (2011). Validation of wet snow maps from Envisat/ASAR-Data. *Master's thesis*, University of Zurich, Zurich (Switzerland).
- Schellenberger, T., Ventura, B., Zebisch, M., & Notarnicola, C. (2012). Wet snow cover mapping algorithm based on multitemporal COSMO-SkyMed X-band SAR images. *IEEE Journal of Selected Topics in Applied Earth Observations and Remote Sensing*, *5*(3), 1045-1053. DOI: 10.1109/JSTARS.2012.2190720
- Shi, J., & Dozier, J. (1993). Measurements of snow-and glacier-covered areas with single-polarisation SAR. *Annals of Glaciology*, *17*(1), 72-76. DOI: 10.3198/1993AoG17-1-72-76
- Small, D. (2011). Flattening gamma: Radiometric terrain correction for SAR imagery. *IEEE Transactions on Geoscience and Remote Sensing*, *49*(8), 3081-3093. DOI: 10.1109/TGRS.2011.2120616
- Small, D. (2012, July). SAR backscatter multitemporal compositing via local resolution weighting. *2012 IEEE International Geoscience and Remote Sensing Symposium,* 4521-4524. IEEE. DOI: 10.1109/IGARSS.2012.6350465
- Small, D., Jehle, M., Meier, E., & Nüesch, D. (2004, May). Radiometric terrain correction incorporating local antenna gain. *Proc. of EUSAR*, 25-27.
- Small, D., Miranda, N., Zuberbuhler, L., Schubert, A., & Meier, E. (2010, December). Terrain-corrected Gamma: Improved thematic land-cover retrieval for SAR with robust radiometric terrain correction. *ESA Special Publication, 686*. DOI: 10.5167/uzh-41236
- Snehmani, Singh, M. K., Gupta, R. D., Bhardwaj, A., & Joshi, P. K. (2015). Remote sensing of mountain snow using active microwave sensors: a review. *Geocarto International*, *30*(1), 1-27. DOI: 10.1080/10106049.2014.883434
- Stiles, W. H., & Ulaby, F. T. (1980). The active and passive microwave response to snow parameters: 1. Wetness. *Journal of Geophysical Research: Oceans*, *85*(C2), 1037-1044. DOI: 10.1029/JC085iC02p01037
- Storvold, R., & Malnes, E. (2004, September). Snow covered area retrieval using ENVISAT ASAR wideswath in mountainous areas. *Geoscience and Remote Sensing Symposium, 2004. IGARSS'04. Proceedings. 2004 IEEE International*, *3*, 1845-1848. IEEE. DOI: 10.1109/IGARSS.2004.1370697
- Storvold, R., Malnes, E., & Lauknes, I. (2006). Using ENVISAT ASAR wideswath data to retrieve snow covered area in mountainous regions. *EARSeL eProceedings*, *4*(2), 150-156.

- Strozzi, T., Wegmuller, U., & Matzler, C. (1999). Mapping wet snowcovers with SAR interferometry. *International Journal of Remote Sensing*, *20*(12), 2395-2403. DOI: 10.1080/014311699212083
- Torres, R., et al. (2012). GMES Sentinel-1 mission. *Remote Sensing of Environment, 120*, 9-24. DOI: 10.1016/j.rse.2011.05.028
- USGS United States Geological Survey (2016). Explanations for the National Water Conditions. Retrieved from http://water.usgs.gov/nwc/explain_data.html on 30.06.2016.
- WMO and GCOS (2011). Systematic Observation Requirements for Satellite-Based Data Products for Climate – 2011 Update. *GCOS - 154*. Geneva: WMO GCOS.

A Appendix

A.1 List of Abbreviations

ASAR	Advanced Synthetic Aperture Radar
CORINE	Coordination of Information on the Environment
COSMO	Constellation of small Satellites for Mediterranean basin Observation
DEM	Digital Elevation Model
ECMWF	European Centre for Medium-Range Weather Forecasts
ENL	Equivalent Number of Looks
ENVISAT	Environmental Satellite
ERA	ECMWF Re-Analysis
ERS-1/2	European Remote Sensing Satellites 1 and 2
ESA	European Space Agency
EURAC	European Academy in Bozen, Italy
GCOS	Global Climate Observing System
GDAL	Geospatial Data Abstraction Library
GTC	Geocoded Terrain-Corrected radar image
LOSS	Length-Of-Snow-Season
LRW	Local Resolution Weighting
MODIS	Moderate Resolution Imaging Spectroradiometer
NASA	National Aeronautics and Space Administration
NDSI	Normalised Difference Snow Index
NDVI	Normalised Difference Vegetation Index
RTC	Radiometrically Terrain-Corrected radar image
SAR	Synthetic Aperture Radar
SRTM	Shuttle Radar Topography Mission
UTC	Universal Time Coordinated
VH	Cross-polarisation (Vertical – Horizontal)
VV	Like-polarisation (Vertical – Vertical)

A.2 Reference images

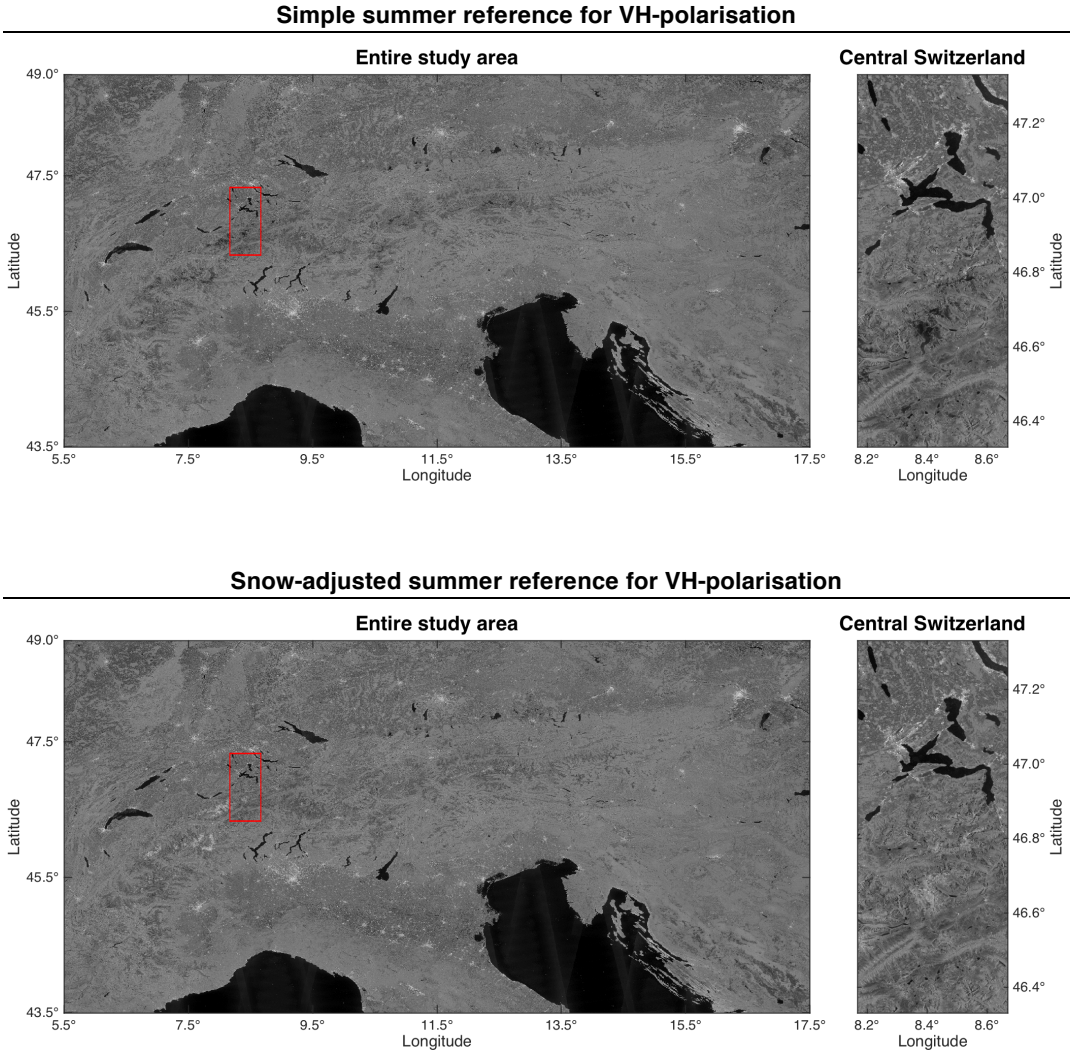

Figure 38. Comparison of the simple and the snow-adjusted summer reference images for VH-polarisation. Left: image over the entire study area. Right: Subset of Lucerne and Central Switzerland.

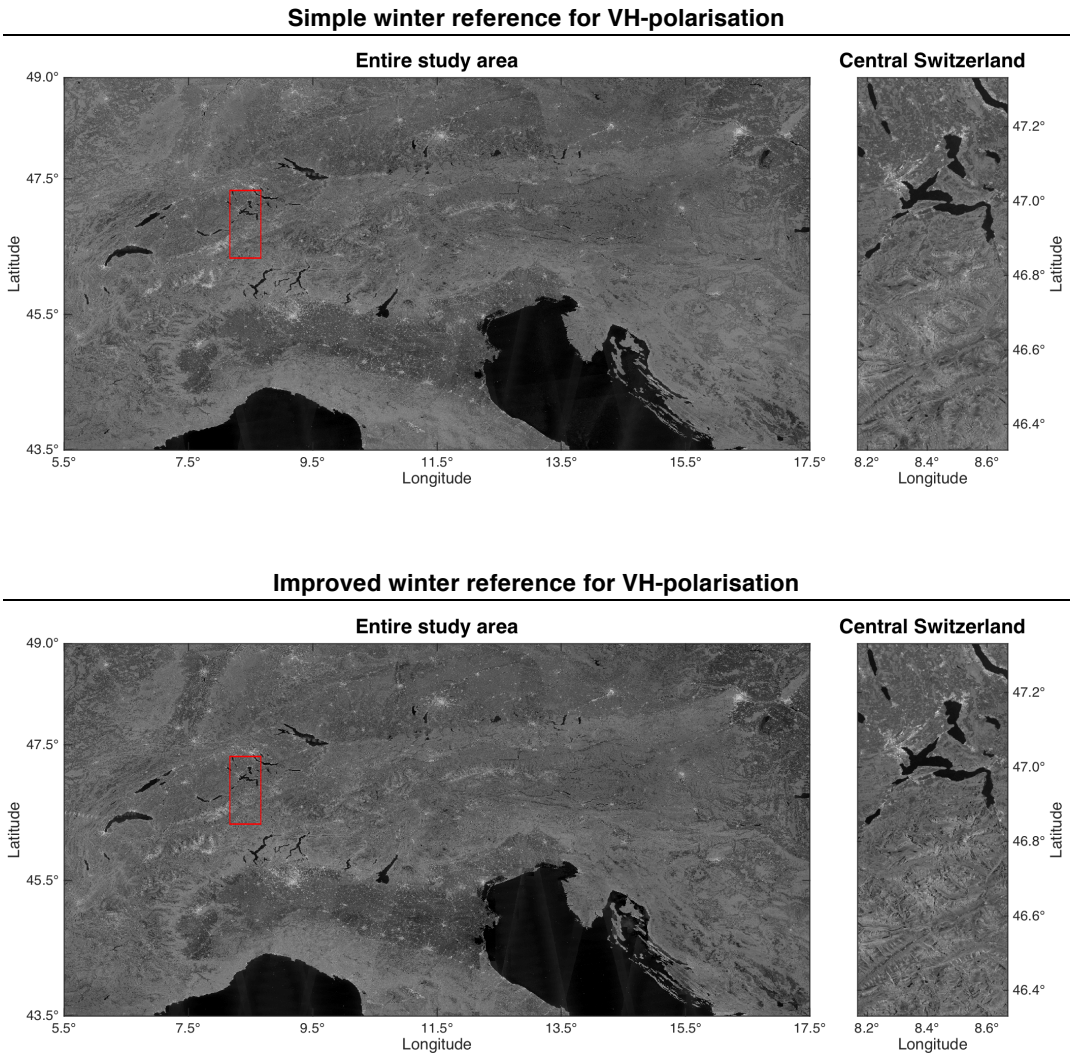

Figure 39. Comparison of the simple and the improved winter reference images for VH-polarisation. Left: image over the entire study area. Right: Subset of Lucerne and Central Switzerland.

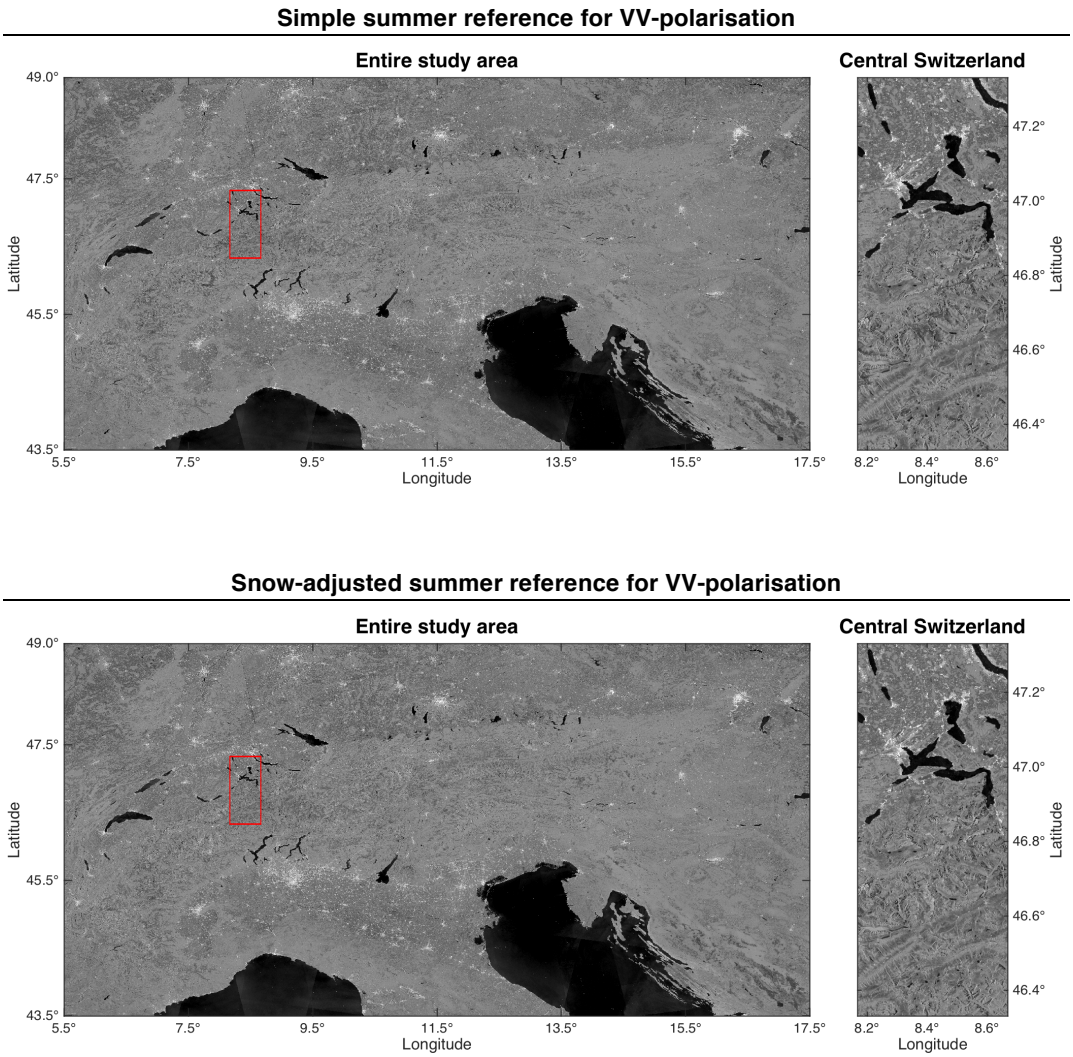

Figure 40. Comparison of the simple and the snow-adjusted summer reference images for VV-polarisation. Left: image over the entire study area. Right: Subset of Lucerne and Central Switzerland.

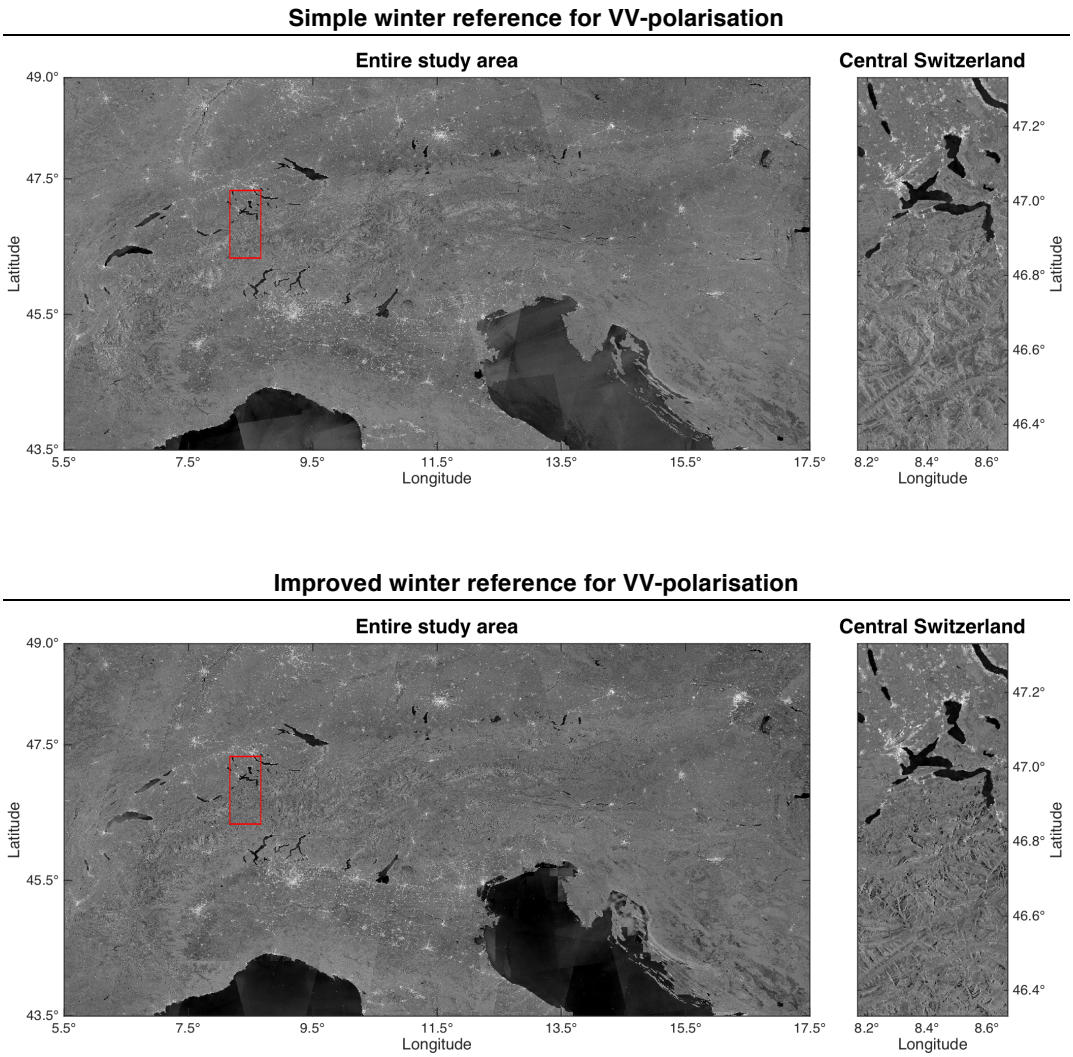

Figure 41. Comparison of the simple and the improved winter reference images for VV-polarisation. Left: image over the entire study area. Right: Subset of Lucerne and Central Switzerland.

A.3 Wet snow thresholds

Land cover class	Elevation	Summer reference		Winter reference		Snow adjusted summer reference		Improved winter reference	
		VV	VH	VV	VH	VV	VH	VV	VH
Urban areas	0-500 m	-	-	-	-	-	-	-	-
	500-1000 m	-	-	-	-	-	-	-	-
	below 2000 m	-	-	-	-	-	-	-	-
	above 2000 m	-	-	-	-	-	-	-	-
	all elevations	-	-	-	-	-	-	-	-
Agricultural areas	0-500 m	-	-	-	-	-	-	-	-
	500-1000 m	-	-	-	-	-	-	-	-
	1000-1500 m	-	-	-	-	-	-	-	-
	below 2000 m	-	-	-	-	-	-	-	-
	above 2000 m	-	-	-	-	-	-	-	-
	all elevations	-	-	-	-	-	-	-	-
Forests	0-500 m	-	-	-	-	-	-	-	-
	500-1000 m	-	-	-	-	-	-	-	-
	1000-1500 m	-	-	-	-	-	-	-	-
	1500-2000 m	-	-	-	-	-	-	-	-
	below 2000 m	-	-	-	-	-	-	-	-
	above 2000 m	-	-	-	-	-	-	-	-
	all elevations	-	-	-	-	-	-	-	-
Scrubland	0-500 m	-	-	-	-	-	-	-	-
	500-1000 m	-	-	-	-	-	-	-	-
	1000-1500 m	-	-	-	-	-	-	-	-
	1500-2000 m	-	-	-	-	-	-	-	-
	2000-2500 m	-1.8	-2.0	-1.1	-0.7	-1.7	-1.9	-0.7	-1.0
	2500-3000 m	-1.9	-1.6	-0.9	-0.5	-1.9	-1.6	-0.9	-1.3
	below 2000 m	-	-	-	-	-	-	-	-
	above 2000 m	-1.8	-1.9	-1.1	-0.7	-1.7	-1.9	-0.7	-1.0
	all elevations	-	-	-	-	-	-	-	-
Non-vegetated areas	1500-2000 m	-	-	-	-	-	-	-	-
	2000-2500 m	-3.0	-1.9	-1.5	-1.1	-2.9	-1.9	-1.0	-1.3
	2500-3000 m	-3.3	-1.9	-1.4	-1.0	-3.2	-1.9	-1.2	-1.5
	3000-3500 m	-	-1.1	-1.1	-1.0	-	-1.7	-	-1.5
	below 2000 m	-	-	-	-	-	-	-	-
	above 2000 m	-3.1	-1.9	-1.5	-1.1	-3.0	-1.9	-1.1	-1.5
	all elevations	-3.1	-1.9	-1.5	-1.1	-3.0	-1.9	-1.1	-1.5
Glacier	2500-3000 m	-0.1	1.3	-1.1	-1.2	-1.6	-2.2	-1.3	-1.8
	3000-3500 m	0.7	3.0	-1.2	-1.4	-1.9	-2.6	-1.5	-2.0
	3500-4000 m	3.2	-	-1.4	-1.7	-2.3	-3.0	-1.6	-2.0
	below 2000 m	-	-	-	-	-	-	-	-
	above 2000 m	0.7	2.5	-1.2	-1.3	-1.8	-2.4	-1.4	-1.9
	all elevations	0.7	2.5	-1.2	-1.3	-1.8	-2.4	-1.4	-1.9

Table 6. Wet snow thresholds (in dB) for the different reference scenes and polarisations, extracted from individual histograms per land cover class.

Land cover class	Elevation	Summer reference		Winter reference		Snow adjusted summer reference		Improved winter reference	
		VV	VH	VV	VH	VV	VH	VV	VH
All land cover classes	0-500 m	-	-	-	-	-	-	-	-
	500-1000 m	-	-	-	-	-	-	-	-
	1000-1500 m	-	-	-	-	-	-	-	-
	1500-2000 m	-	-	-	-	-	-	-	-
	2000-2500 m	-	-2.0	-1.3	-0.9	-	-1.9	-0.9	-1.2
	2500-3000 m	-3.0	-1.7	-1.3	-1.0	-2.9	-1.9	-1.2	-1.5
	3000-3500 m	-	-	-1.2	-1.2	-1.9	-2.1	-1.3	-1.7
	3500-4000 m	2.4	3.4	-1.4	-1.6	-2.1	-2.7	-1.3	-1.7
	below 2000 m	-	-	-	-	-	-	-	-
	above 2000 m	-2.6	-1.8	-1.3	-1.0	-2.6	-2.0	-1.0	-1.4
	all elevations	-	-	-	-	-	-	-	-

Table 7. Wet snow thresholds (in dB) for the different reference scenes and polarisations, extracted from histograms over all land cover classes.

A.4 Confusion matrices for the final snow maps of 2015 and 2016

		MODIS snow product	
		Snow	**No snow**
Sentinel wet snow maps	**Wet snow**	P_{11}	P_{12}
	Dry/no snow	P_{21}	P_{22}

Table 8. Template of the accuracy assessment confusion table.

Year: 2015 / Reference: improved winter reference / Unit: No. of Pixels

Composite period	**P_{11}**	**P_{12}**	**P_{21}**	**P_{22}**
20150202-20150217	2136027	500653	29965889	17039116
20150210-20150225	1995596	410745	23685690	21957656
20150218-20150305	2111569	461764	16918122	31184360
20150226-20150313	1919333	696493	11208120	36561001
20150306-20150321	1779705	1025193	9871276	38166522
20150314-20150329	1597439	401957	8347127	42144097
20150322-20150406	1679039	45306	6931319	42058098
20150330-20150414	2193578	87001	7091702	43240274
20150407-20150422	3298899	391557	5327035	43654507
20150415-20150430	3733243	572103	2848048	45263694
20150423-20150508	2982790	476390	1667580	45831449
20150501-20150516	2128537	655300	686941	47185904
20150509-20150524	1843017	940081	511120	48728187
20150517-20150601	1309568	880618	417841	47313674
20150525-20150609	1254346	951674	416658	49922069
20150602-20150617	762422	741124	275275	46471394
20150610-20150625	308344	514271	140251	40422402
20150618-20150703	451490	407187	207066	46888618
20150626-20150711	350820	342482	167906	47143489
20150704-20150719	241284	282842	109660	50802316
20150712-20150727	211024	232767	84583	51000493
20150720-20150804	194319	182212	89075	49172994
20150728-20150812	186408	185612	83065	47098186
20150805-20150820	161102	238958	50217	46992671
20150813-20150828	191790	177695	72103	46246467
20150821-20150905	190621	158343	85986	47285145
20150829-20150913	226363	168647	126531	47202107

Table 9. Confusion matrix values for all wet snow maps produced with the final algorithm (applied reference scene: improved winter reference) over the snowmelt period of 2015 (P-values represent the number of pixels of the corresponding confusion matrix cell).

Year: 2015 / Reference: snow-adjusted summer reference / Unit: No. of Pixels

Composite period	P_{11}	P_{12}	P_{21}	P_{22}
20150202-20150217	6204236	1553161	25897605	15986605
20150210-20150225	4391564	1395154	21289650	20973244
20150218-20150305	4035015	1179630	14994601	30466491
20150226-20150313	3547421	1893006	9579956	35364488
20150306-20150321	2767117	2124883	8883790	37066831
20150314-20150329	1935873	685180	8008619	41860869
20150322-20150406	1814675	190553	6795611	41912846
20150330-20150414	2239996	233745	7045206	43093530
20150407-20150422	3166366	379707	5459506	43666337
20150415-20150430	3636932	523192	2944309	45312578
20150423-20150508	2790321	467448	1860041	45840341
20150501-20150516	1967476	629717	848001	47211414
20150509-20150524	1739405	842074	614731	48826120
20150517-20150601	1254614	732531	472795	47461749
20150525-20150609	1172406	791952	498596	50081711
20150602-20150617	688117	626119	349580	46586317
20150610-20150625	273100	345838	175495	40590835
20150618-20150703	370953	205206	287603	47090592
20150626-20150711	283442	98101	235284	47387863
20150704-20150719	213422	46352	137522	51038806
20150712-20150727	189992	69181	105615	51164079
20150720-20150804	176949	48077	106445	49307129
20150728-20150812	170719	49897	98754	47233901
20150805-20150820	149644	113908	61675	47117715
20150813-20150828	177041	75401	86852	46348755
20150821-20150905	174272	58247	102335	47385229
20150829-20150913	194415	76106	158479	47294636

Table 10. Confusion matrix values for all wet snow maps produced with the final algorithm (applied reference scene: snow-adjusted summer reference) over the snowmelt period of 2015 (P-values represent the number of pixels of the corresponding confusion matrix cell).

Year: 2016 / Reference: improved winter reference / Unit: No. of Pixels

Composite period	P_{11}	P_{12}	P_{21}	P_{22}
20160202-20160217	722123	165348	9844343	33464991
20160210-20160225	721923	415492	9844540	41693289
20160218-20160305	897819	277051	11101287	40397594
20160226-20160312	836064	241760	11164555	40433314
20160305-20160320	1141236	209460	12591278	38679976
20160313-20160328	1546667	655281	9662371	40778855
20160321-20160405	2630761	598000	6049734	41421951
20160329-20160413	2767173	717937	2030107	43506655
20160406-20160421	4143163	592581	2361875	44962041
20160414-20160429	3967131	537072	2571224	44994888
20160422-20160507	3641229	687375	2545602	44981607
20160430-20160515	3352725	693558	1573058	45763972
20160508-20160523	2894464	960789	675730	47015057
20160516-20160531	2964652	649713	951300	47294939
20160524-20160608	1281335	707688	329914	47988314

Table 11. Confusion matrix values for all wet snow maps produced with the final algorithm (applied reference scene: improved winter reference) over the snowmelt period of 2016 (P-values represent the number of pixels of the corresponding confusion matrix cell).

Year: 2016 / Reference: snow-adjusted summer reference / Unit: No. of Pixels

Composite period	P_{11}	P_{12}	P_{21}	P_{22}
20160202-20160217	1496919	411186	9069513	33219129
20160210-20160225	1452949	735828	9113480	41372754
20160218-20160305	1471553	648064	10527378	40026523
20160226-20160312	1464531	615318	10535913	40059698
20160305-20160320	1724445	466979	12007842	38422451
20160313-20160328	1954278	817770	9254547	40616346
20160321-20160405	2805757	900572	5874630	41119282
20160329-20160413	2855061	1001361	1942120	43223107
20160406-20160421	4135679	745466	2369268	44809014
20160414-20160429	3956434	740152	2581795	44791701
20160422-20160507	3673996	764260	2512678	44904646
20160430-20160515	3212243	662958	1713432	45794448
20160508-20160523	2745010	982582	825166	46993065
20160516-20160531	2789692	609186	1126242	47335261
20160524-20160608	1217551	658703	393695	48037087

Table 12. Confusion matrix values for all wet snow maps produced with the final algorithm (applied reference scene: snow-adjusted summer reference) over the snowmelt period of 2016 (P-values represent the number of pixels of the corresponding confusion matrix cell).

A.5 Declaration of originality

Personal declaration:

I hereby declare that the submitted thesis is the result of my own, independent work. All external sources are explicitly acknowledged in the thesis.

_____	_____
Place and date	Signature